

THE INSTITUTE OF SPACE AND ASTRONAUTICAL SCIENCE  
YOSHINODAI, SAGAMIHARA, KANAGAWA 229

ISAS RESEARCH NOTE

ISAS RN 619

## X-Ray Study of Type 2 Seyfert Galaxies

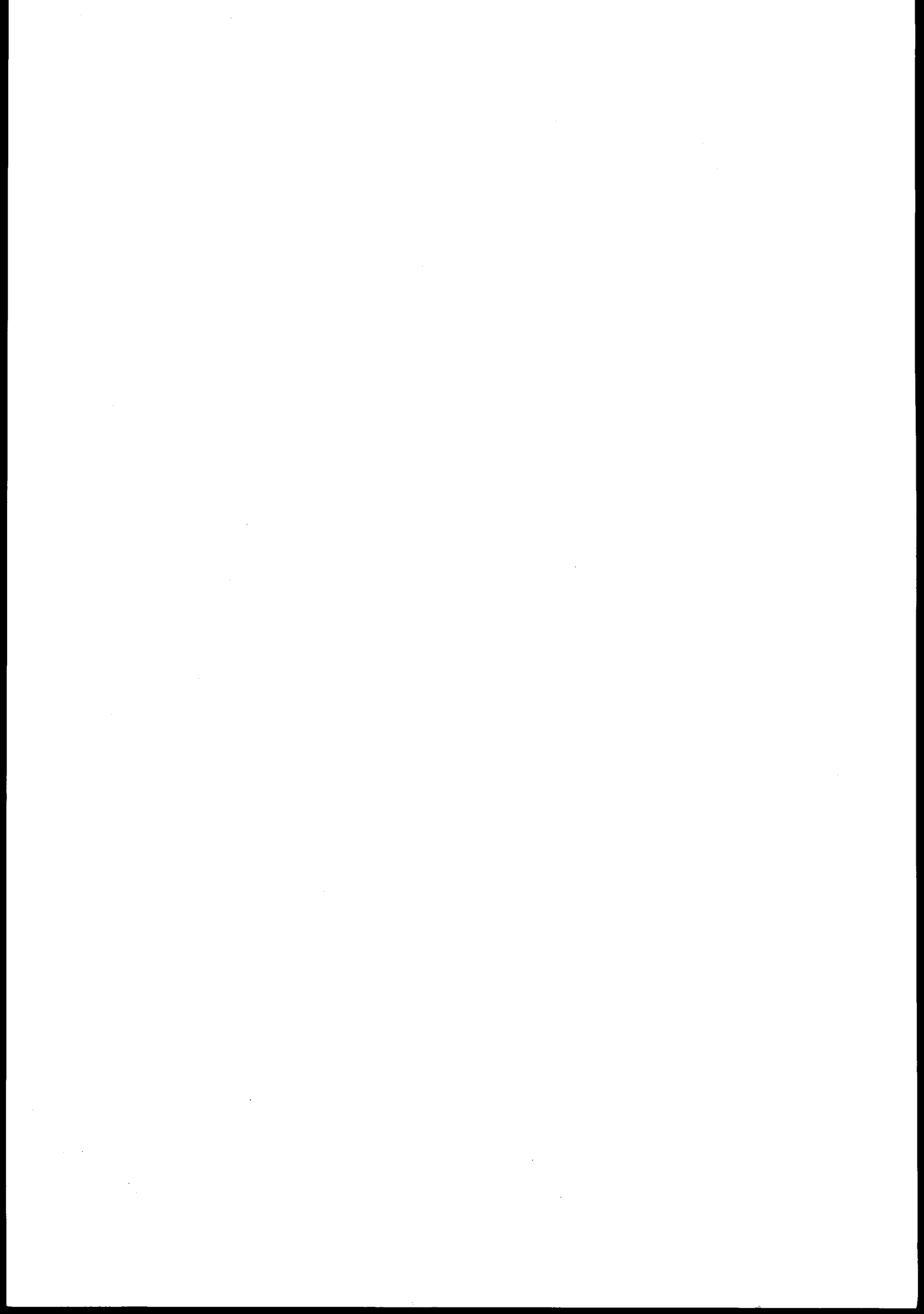
Shiro Ueno

May 1997

*Department of Physics,  
Graduate School of Science, Kyoto University, sakyoku, kyoto,  
Japan 606-01  
E-mail: Ueno@cr.scphys.kyoto-u.ac.jp*

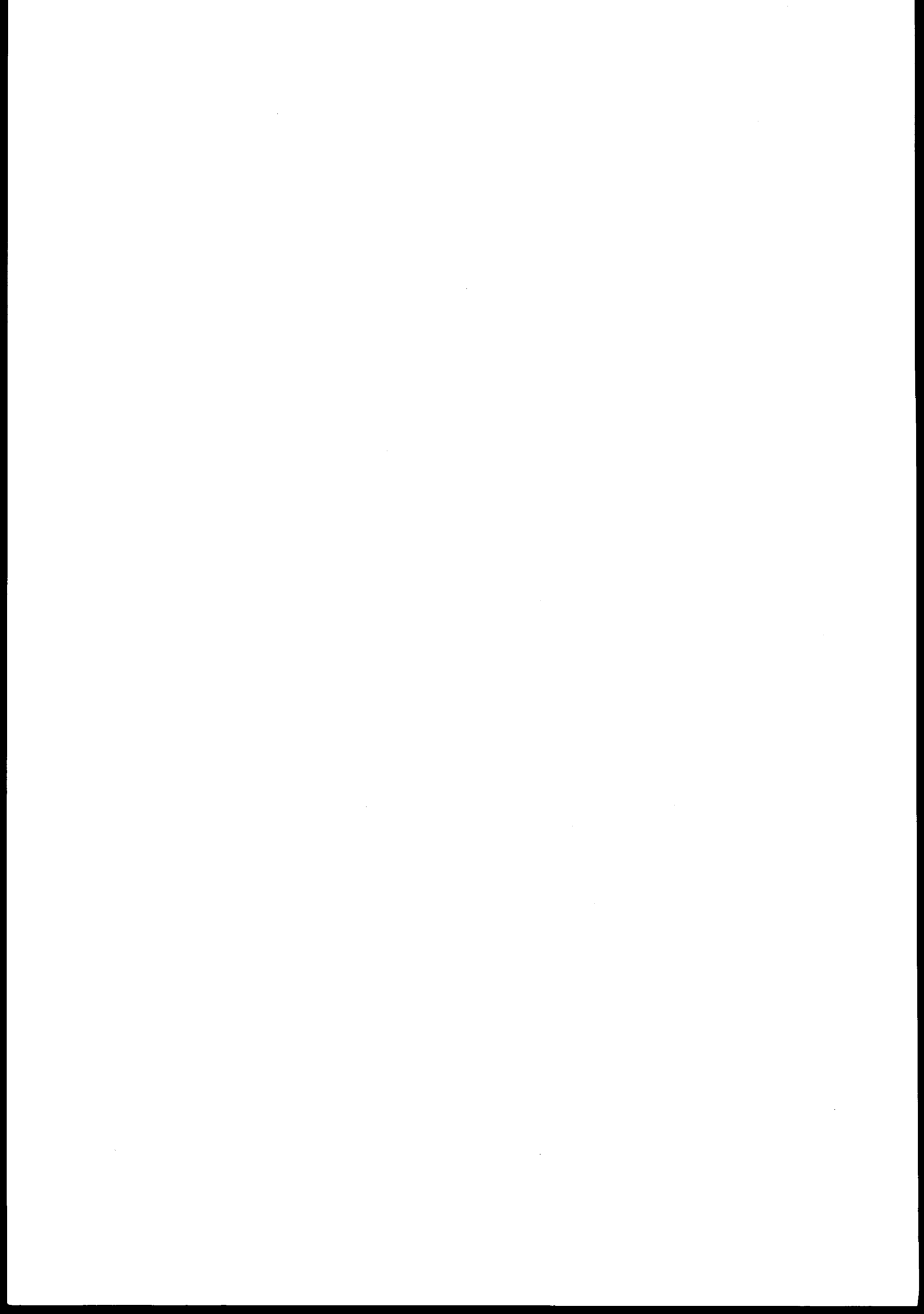
Thesis Submitted to  
the Graduate School of Science, Kyoto University  
for the Degree of Doctor of Science (Physics)  
December, 1995

This work was performed by use of data obtained with ISAS  
satellite ASCA in collaboration with ASCA team member.



# X-Ray Study of Type 2 Seyfert Galaxies

Shiro Ueno



## Abstract

This paper summarizes the ASCA results of more than a dozen Seyfert 2 galaxies. X-rays in the wide energy range of the 0.5 – 10 keV band are reported for the first time. The overall X-ray spectra from the majority of Seyfert 2s are fitted with power-law models consisting of a soft and hard components; the former with no significant absorption and the latter with a low energy cutoff. We discuss this structure in the conjecture of the unified Seyfert model coupled with possible association of starburst activities. Most of the photon indexes of the hard component lie in the range of 1.5 – 1.7, which indicates, together with the large absorption, that the hard component is due to the central emission through a large column of gas, with the photon index equal to or smaller than that of Seyfert 1s. The photon indexes of the soft component, on the other hand, exhibit a large scatter, which may be discussed with a mixture of a reflective component and a star burst activity. We report that the soft X-ray flux is almost constant in the wide range of time scales, while the hard X-ray flux shows significant variability. We show the relation of the soft X-ray flux as a function of the hard X-ray luminosity and suggest that the scattered component seen in the low energy band is a few to 10 % of the direct flux. This is a major reason why the observed fluxes of Seyfert 2s are generally weaker than those of Seyfert 1s.

# Contents

<b>Abstract</b>	<b>1</b>
<b>Contents</b>	<b>2</b>
<b>List of tables</b>	<b>5</b>
<b>List of figures</b>	<b>6</b>
<b>1 Introduction</b>	<b>8</b>
<b>2 Review</b>	<b>10</b>
2.1 Active galactic nuclei . . . . .	10
2.2 Observed optical properties of Seyfert galaxies . . . . .	10
2.3 Cylindrical structure and Unified model . . . . .	13
2.4 Observed X-ray properties of Seyfert galaxies . . . . .	15
2.4.1 Hard X-ray spectra of Seyfert 1s . . . . .	15
2.4.2 Hard X-ray spectra of Seyfert 2s . . . . .	18
2.4.3 Soft X-ray spectra of Seyfert 1s and 2s . . . . .	19
2.4.4 X-ray time variability . . . . .	21
2.5 Starburst galaxies . . . . .	22
<b>3 Instrumentation</b>	<b>23</b>
3.1 ASCA . . . . .	23
3.2 X-ray telescopes . . . . .	24
3.3 Focal plane detectors . . . . .	24
<b>4 Observations and results of individual sources</b>	<b>26</b>
4.1 The log of the ASCA observations . . . . .	26
4.2 Observation mode, Data Screening and Standard model fitting . . . . .	29
4.3 Seyfert 2s showing strong low-energy cut offs in the Ginga spectra . . . . .	30
4.3.1 IC 5063 and NGC 4507 . . . . .	30
4.3.2 Discussion for IC5063 and NGC4507: confirmation of strong cutoffs .	36
4.3.3 NGC 1808 and NGC 1667 . . . . .	39
4.3.4 Discussion for NGC1808 and NGC1667: disappearance of cutoffs . . .	43

4.4	Seyfert 2 showing a strong Fe K line in the Ginga spectra . . . . .	44
4.4.1	NGC 1068 . . . . .	44
4.4.2	Discussion for NGC 1068 . . . . .	51
4.5	Seyfert 2s showing optical polarized broad lines . . . . .	52
4.5.1	Mkn 463 . . . . .	52
4.5.2	Discussion for Mkn 463 . . . . .	58
4.5.3	Mkn 1210 . . . . .	61
4.5.4	Mkn 477 . . . . .	62
4.5.5	Discussion for Mkn 1210 and Mkn 477 . . . . .	63
4.6	Seyfert 2 showing moderate a low energy cutoff in the Ginga spectra . . . . .	64
4.6.1	NGC 2110 . . . . .	64
4.6.2	Discussion for NGC 2110 . . . . .	70
4.7	Other Seyfert 2s observed with ASCA . . . . .	73
4.7.1	PKS B1319-164 . . . . .	73
4.7.2	Discussion for PKS B1319-164 . . . . .	76
4.7.3	NGC 7319 . . . . .	77
4.7.4	Discussion for NGC 7319 . . . . .	81
4.7.5	NGC 4388 . . . . .	81
4.7.6	Discussion for NGC 4388 . . . . .	85
4.8	Starburst galaxies observed with ASCA for comparisons with Seyfert 2s . . . . .	85
4.8.1	NGC 253 . . . . .	85
4.8.2	NGC 3079 . . . . .	87
4.8.3	M82 . . . . .	88
<b>5</b>	<b>Discussion for the ASCA sample of type 2 Seyfert galaxies</b>	<b>96</b>
5.1	Properties of hard components and Comparison with Seyfert 1 galaxies . . . . .	96
5.1.1	Time Variability . . . . .	96
5.1.2	Luminosity . . . . .	97
5.1.3	Slope . . . . .	98
5.2	The origins of soft components . . . . .	99
5.2.1	X-ray variability and slopes . . . . .	99
5.2.2	Evaluation of non-AGN X-ray flux by using $L_{\text{FIR}}$ and $L_B$ . . . . .	102
5.2.3	The flux ratio of the soft and hard component . . . . .	105

5.2.4	Search for fluorescent lines . . . . .	108
5.3	Distribution of absorption column . . . . .	110
5.3.1	All polarized broad line sources show heavy absorption . . . . .	110
5.3.2	Peak in $N_{\text{H}}$ distribution and the cosmic X-ray background . . . . .	111
5.3.3	Spatial distribution of absorbing material . . . . .	112
5.3.4	The depth of Fe K edge . . . . .	113
5.4	Fe K line . . . . .	115
5.4.1	$\log N_{\text{H}}$ and equivalent width of iron line . . . . .	115
5.4.2	Emission line from warm iron . . . . .	116
<b>6</b>	<b>Conclusions</b>	<b>118</b>
<b>A</b>	<b>The O[III] <math>\lambda</math>5007 flux of Seyfert 2 galaxies</b>	<b>119</b>
<b>B</b>	<b>Ionization parameter</b>	<b>125</b>
<b>C</b>	<b>ASCA spectra of Seyfert 2 and Starburst galaxies</b>	<b>126</b>
<b>D</b>	<b>Glossary</b>	<b>139</b>
	<b>Acknowledgments</b>	<b>140</b>
	<b>References</b>	<b>141</b>

**List of Tables**

1	Performance of SIS and GIS . . . . .	25
2	Observation log . . . . .	26
3	Previous observations and Remarks . . . . .	27
4	Applied distance and Galactic absorption . . . . .	28
5	Source positions in the ASCA image of IC 5063 . . . . .	31
6	Source positions in the ASCA image of NGC 4507 . . . . .	34
7	Hard X-ray properties of IC 5063 obtained with Ginga and ASCA . . . . .	38
8	Hard X-ray properties of NGC 4507 obtained with Ginga and ASCA . . . . .	39
9	Results of two component model for NGC 1808 . . . . .	41
10	Significant low energy lines in NGC1068 . . . . .	49
11	Sources in the GIS image selected by using a sliding-cell method (Mkn 463) . . . . .	54
12	Spectral fitting results with double-component models (Mkn463) . . . . .	55
13	Scattered X-rays model for the ASCA SIS spectra of NGC 2110 . . . . .	68
14	Thermal plasma emission model for the ASCA SIS spectra of NGC 2110 . . . . .	69
15	Dual absorber model for the ASCA SIS spectra of NGC 2110 . . . . .	72
16	Results of model fits for the soft component of PKS B1319-164 . . . . .	77
17	Source positions in the ASCA SIS image of NGC 7319 . . . . .	79
18	Source positions in the ASCA SIS image of NGC 4388 . . . . .	83
19	The best-fit parameters for double power-law model . . . . .	90
20	Observed flux and luminosity for double power-law model . . . . .	92
21	Absorption-corrected flux and luminosity for double power-law model . . . . .	94
22	Normalization ratios of the soft to hard components . . . . .	106
23	Scattering efficiency . . . . .	108
24	Upper limits of fluorescent-line emission in the soft component . . . . .	109
25	Depths of Fe K edge . . . . .	114
26	O[III] $\lambda$ 5007 flux of Seyfert 2 galaxies . . . . .	119
26	— Continued . . . . .	120
26	— Continued . . . . .	121
26	— Continued . . . . .	122
26	— Continued . . . . .	123

**List of Figures**

1	A unified model for Seyfert galaxies . . . . .	14
2	Compton reflection model . . . . .	17
3	The schematic view of the ASCA satellite . . . . .	23
4	The GIS contour image of IC 5063 in the 0.5 – 2 keV band . . . . .	31
5	The GIS contour image of IC 5063 in the 4 – 10 keV band . . . . .	31
6	The result of the single power-law model for IC5063 . . . . .	32
7	The result of the double power-law model for IC5063 . . . . .	33
8	The same as in figure 6, but for NGC 4507 . . . . .	35
9	The same as in figure 7, but for NGC 4507 . . . . .	35
10	The result of the RS model for the soft component of IC 5063 . . . . .	37
11	The same as in figure 6, but for NGC 1808 . . . . .	40
12	The same as in figure 6, but for NGC 1667 . . . . .	42
13	High energy spectrum including Fe K line complex(only SIS 0 data is shown) . . . . .	46
14	Low energy spectrum of NGC 1068 (only SIS 0 data is shown) . . . . .	47
15	The ASCA SIS spectrum of NGC1068 . . . . .	50
16	X-ray spectra of Mkn 463 and Single power-law model . . . . .	55
17	Confidence contours of $N_H$ versus $\Gamma(\text{hard})$ for Mkn463 . . . . .	57
18	X-ray spectrum of Mkn 463 and double power-law model . . . . .	57
19	The same as in figure 7, but for Mkn 1210 . . . . .	62
20	The same as in figure 7, but for Mkn 477 . . . . .	63
21	The same as in figure 6, but for NGC 2110 . . . . .	66
22	The same as in figure 7, but for NGC 2110 . . . . .	67
23	The same as in figure 6, but for PKS B1319-164 . . . . .	74
24	The same as in figure 7, but for PKS B1319-164 . . . . .	75
25	The 4-10 keV contour image of NGC 7319 . . . . .	78
26	The 0.5-2 keV contour image of NGC 7319 . . . . .	78
27	The same as in figure 6, but for NGC 7319 . . . . .	79
28	The same as in figure 7, but for NGC 7319 . . . . .	80
29	The 4-10 keV countour image of NGC 4388 . . . . .	83
30	The 0.5-2 keV countour image of NGC 4388 . . . . .	83
31	The same as in figure 7, but for NGC 4388 . . . . .	84

32	The result of the single power-law model for NGC 253 . . . . .	86
33	The same as in figure 32, but for NGC 3079 . . . . .	88
34	The same as in figure 32, but for M82 . . . . .	89
35	Search for long term variability (hard flux) . . . . .	97
36	Comparison of $L_X(2-10 \text{ keV})$ between Seyfert 1 and 2 galaxies . . . . .	98
37	The photon index of hard component . . . . .	99
38	Search for long term variability (soft flux) . . . . .	101
39	The photon index of soft component . . . . .	102
40	$L_X(0.5-2 \text{ keV})$ vs. $L_{\text{FIR}}(40-120\mu\text{m})$ . . . . .	103
41	Observed $\log(L_X)$ vs. inferred $\log(L_X)$ . . . . .	105
42	$F_X(\text{soft})/F_X(\text{hard})$ vs. Photon Index(soft) . . . . .	107
43	The distribution of absorption column thickness . . . . .	111
44	The configuration of a simple torus model . . . . .	113
45	The expected distribution of column density for a simple torus model . . . . .	113
46	$N_{\text{Fe}}$ vs. $N_{\text{H}}$ . . . . .	115
47	$EW$ of Fe K line vs. Absorption column . . . . .	116
48	Fe line emission from NGC1068 . . . . .	117
49	The ASCA spectra of IC5063 . . . . .	126
50	The ASCA spectra of NGC4507 . . . . .	127
51	The ASCA spectra of NGC1808 . . . . .	128
52	The ASCA spectra of NGC1667 . . . . .	129
53	The ASCA spectra of NGC1068 . . . . .	130
54	The ASCA spectra of Mkn463 . . . . .	131
55	The ASCA spectra of Mkn 1210 . . . . .	132
56	The ASCA spectra of Mkn 477 . . . . .	133
57	The ASCA spectra of NGC2110 . . . . .	134
58	The ASCA spectra of PKS B1319-164 . . . . .	135
59	The ASCA spectra of NGC7319 . . . . .	136
60	The ASCA spectra of NGC4388 . . . . .	137
61	The ASCA SIS spectra of starburst galaxies . . . . .	138

## 1 Introduction

Active Galactic Nuclei (AGNs) emit a huge amount of energies in the wide range of the wave length, from a very compact region at the center of the host galaxies, demonstrating extremely high efficiency of the energy release. This leads us to the well-accepted paradigm that AGN is an accretion-powered massive black hole. Thus AGNs are excellent observatories for the study of high gravity physics. Due to this potential importance, many astronomers have investigated the emission mechanism and the structure of AGNs, discussed the nature of its structure, evolution and possible connection to the starburst galaxies.

Seyfert galaxies are located relatively nearby from the earth, comprise the majority of AGNs, and are classified as type 1 or 2 according to the presence or absence of broad emission lines in the optical spectra. The high velocities indicated by the broad lines in Seyfert 1 galaxies are taken to be good evidence for a compact massive object, as are suggested by the strong and variable hard X-ray emission that is also generally observed in these objects. In contrast, Seyfert 2 galaxies possess neither of these characteristics, so the scenario that they too have an accreting massive black hole is less compelling. Several attempt to unify these apparently different type of AGNs have been made. The breakthrough of this approach was given by Antonucci and Miller (1985[3]). They found faint polarized broad lines in the archetypical Seyfert 2 galaxy; NGC 1068, and concluded that the region emitting the broad lines in NGC 1068 is completely hidden by a thick matter, and a fraction of the broad lines which are scattered by electrons in an extended region surrounding the nucleus is observable, showing us as a polarized broad line component. This result has revived the long-standing hope that the two classes may be unified. The "unified Seyfert model", in which geometrically and optically thick gases are distributed as a torus around the nucleus, have been proposed. From this model, apparent differences between Seyfert 1 and 2 galaxies are explained by the difference of the viewing angle. Further improvement along this approach have been made. For example, Miller and Goodrich (1990[107]) discovered faint polarized broad emission lines in other highly polarized Seyfert 2 galaxies.

In the X-ray band, a number of Seyfert 1 galaxies have been detected so far, while only a few Seyfert 2 galaxies have been known to be X-ray emitters. The Einstein observatory revealed that the luminosity in the 0.5-4.5 keV band from Seyfert 2 galaxies was two orders

of magnitude less than that from Seyfert 1 galaxies ( Kriss et al. 1980[84]). If the soft X-rays are heavily absorbed by a possible thick torus in Seyfert 2 galaxies, either the weak detections or the upper limits on the soft X-ray flux derived from the Einstein Observatory would be naturally explained. Hard X-ray observations would provide a crucial test, because the column density of the torus may become transparent at several keV; X-rays with highly absorbed spectra would be observed. In fact, the Japanese X-ray satellite Ginga have successfully detected hard X-rays from several Seyfert 2 galaxies. The presence of the high column of the gas along the line of sight was directly observed in several Seyfert 2s including the first detection in Mkn 3 ( Awaki et al 1991[10] ). Another clue came again from the X-ray spectrum of NGC1068. Koyama et al (1989[83]), using the Ginga satellite, found an extremely strong iron K line from this galaxy, which can be uniquely interpreted to be due to a fluorescence associated with the scattering X-rays. Despite these big jumps for the unified scheme, the limited S/N ratio and the lack of a low energy sensitivity of the Ginga satellite prevent us to study Seyfert 2s further systematically. ASCA , the new Japanese X-ray astronomy satellite would provide us with a unique study of Seyfert 2s: its high energy response and high S/N ratio can peer deeply into the molecular torus even in relatively faint Seyfert 2s, behind which a Seyfert 1 type AGN may reside. ASCA may provide wider sample than the Ginga sample, which is essential to study the unified model.

The wide energy band of ASCA can be utilized for the observation of the absorbed hard X-rays and unabsorbed but scattered soft X-rays simultaneously. This simultaneous detection is also essential to study the origin of the hard and soft X-rays. Several similarity of Seyfert 2s to starburst galaxies and association of the starburst activity in Seyfert 2s have been reported. This forced us to consider evolution and formation of AGNs, which conflict the unified Seyfert model. One plausible scenario is that an AGN is born via a starburst activity at the galactic center. According as the starburst activity diminish, it will appear to be a Seyfert 2, remaining with a high column of gas. Then it evolved to a normal Seyfert 1. Thus, we have performed systematic ASCA observations of Seyfert 2s taking every opportunity during the ASCA life time. In this paper, we report the ASCA results of Seyfert 2s as well as those of some selected starburst galaxies, compare them, and separate observationally the starburst and Seyfert 2 activities.

## 2 Review

### 2.1 Active galactic nuclei

Active galactic nuclei (AGNs) emit their huge energies in all the wavelength, and are the most violent class of astronomical objects known in the universe. They, from Seyfert galaxies to quasars, and from radio galaxies to radio quasars, appear to form one family. Among them, Seyfert galaxy nuclei are the most abundant "here and now" in the universe; according to, for instance, Table 11.1 of Osterbrock (1989 [125]) they comprise 1% of the nuclei of luminous spiral galaxies. Luminous radio galaxies, which are mostly N, cD, D and E galaxies rather than spirals, are still less abundant by another factor  $10^{-2}$ . Quasars and radio quasars, the most luminous analogues of Seyfert galaxies and radio galaxies, respectively, are both down by factors  $10^{-3}$  with respect to these two classes of active galaxies. These numbers are based on the definition of Schmidt & Green (1983 [154]) that the AGNs below and above the absolute magnitude of  $M_B = -23$  are respectively classified as Seyfert galaxies and quasars. Note that there may be many more AGNs at lower luminosity levels; they would be very difficult to detect even if they exist. Accordingly at this time, the Seyfert galaxy nuclei are the most abundant and nearest, hence the most thoroughly studied type of AGNs.

### 2.2 Observed optical properties of Seyfert galaxies

The Seyfert galaxies are primarily classified by the optical spectra: Seyfert 1s with strong and broad permitted-, and narrow forbidden-lines, and Seyfert 2s, with strong narrow permitted- and forbidden-lines. The intermediate types, defined somewhat later, are Seyfert 1.5s, with strong broad and narrow components of their permitted emission lines, Seyfert 1.8s, with strong narrow and weak broad components of permitted  $H\alpha$  and  $H\beta$ , and Seyfert 1.9s, with still a weaker broad component of  $H\alpha$ , and the broad component of  $H\beta$  too faint to be easily visible. They have been thoroughly described, e.g., by Osterbrock (1988[124], 1991[126]), and are appear to form a continuous sequence from Seyfert 1s to 2s.

The broad lines are interpreted to be emitted in a region ( the broad-line region : BLR) with relatively high electron density, at least  $10^8 \text{ cm}^{-3}$ , comparable to the chromosphere, in which all the forbidden lines are the subjects of collisional deexcitation, hence are weakened to be almost unobservable (Woltjer 1959[208]) . From the line width, the gas velocity in

the BLR is estimated of  $3,000 - 10,000 \text{ km s}^{-1}$ , while the typical size of BLR is deduced to be  $0.01 - 0.1 \text{ pc}$  from the time variability of broad lines.

The narrow lines, on the other hand, are believed to be emitted in a region (the narrow-line region: NLR) of lower electron density of  $10^3 - 10^6 \text{ cm}^{-3}$ , comparable to gaseous nebulae, in which the forbidden lines are not collisionally de-excited significantly. The gas velocity in the NLR is estimated to be  $300 - 1,000 \text{ km s}^{-1}$ . The size of NLRs is believed to be far larger than BLR, because, unlike the broad lines, no significant flux variation of the narrow lines is associated with large continuum variations.

These general paradigms given above have been proposed by Oke and Sargent (1968[122]), Woltjer(1968[209]), and Souffrin(1969[162]).

Extensive studies on the narrow line profiles as functions of ionization potential and critical density for the collisional de-excitation have led to suggest that, in the NLR, the velocity and mean density decrease as the distance of NLR from AGN increases, while the mean ionization decreases or remains constant (De Robertis & Osterbnnrock 1984[34], 1986[35]; Whittle 1985[198]; Appenzellar & Östreicher 1988[5]; Wison & Nath 1990[207]).

An order-of-magnitude estimations were made on several physical parameters using the diagnostic techniques often applied to the nebulae spectroscopy. Consequently, the mean values of the temperature and electron density in NLRs are respectively  $T \sim 10^4 \text{ K}$  and  $N_e \sim 10^4 \text{ cm}^{-3}$ . From the observed luminosities in HI narrow lines (such as  $\text{H}\beta$ ), we estimate the mean size and mass to be  $r \sim 10^2 \text{ pc}$  and  $M \sim 10^6 M_\odot$  (solar mass). In fact, the size of spatially resolved NLRs in a few selected nearest Seyfert 2 galaxies are found within this order.

For the BLRs, the spectroscopic diagnostics, although are not very sensitive to the temperature, give probably  $T \sim 10^4 \text{ K}$ . The mean electron density is more reliably determined primarily from the observed presence of  $\text{C III] } \lambda 1909$ , and to be  $N_e \sim 10^{9.5} \text{ cm}^{-3}$ . The sized and mass of the ionized gas, with the parameters given above, are found typically to be  $r \sim 3 \times 10^{-2} \text{ pc}$ ,  $M \sim 10 M_\odot$ , both are very small scale compared with the host galaxy.

The low temperature of NLRs, together with the observed ionization, clearly indicates that the energy input to the gas is mainly via a photoionization. The large range of the observed ionization, from  $[\text{O I}]$ ,  $[\text{N I}]$  and  $[\text{S II}]$  lines to  $[\text{Ne V}]$  and  $[\text{Fe VII}]$  shows that the relevant photon spectrum is extending to high energies. A power-law photon spectrum of the form of  $F_\nu \propto \nu^{-n}$  with  $n \sim 1$  nicely reproduces the observations as the first approximation. X-rays from the majority of AGNs exhibit a "broken" power law

spectrum with index decreasing to  $n \sim 0.7$  at around 2 keV. Photoionization by this broken power-law spectrum often gives better fit to the data than those of a simple power-law photon distribution (Krupey, Urry, & Carnizares 1990[88]). Abundances determined from the observed emission line spectra are roughly solar, with possible exception of nitrogen of a factor of three overabundance (Veilleux & Osterbrock 1987[185]; Storchi-Bergmann 1991[163]). However, this result is highly model dependent, hence should be conservative.

For the BLR, whether or not the major energy input is photoionization is debatable. The highest-ionization lines, the "coronal" lines [Fe X]  $\lambda 6375$  and [Fe XI]  $\lambda 7892$ , found in the optical and near-IR spectra from a significant fraction of Seyfert galaxies, tend to have widths somewhat larger than most of the narrow lines, but smaller than those of the broad lines. This makes it rather uncertain that these highest-ionization lines are attributable to photoionized regions, but they currently appear to be the most likely interpretation (Korista & Ferland 1989[81])

Many Seyfert 1s, and even more quasars exhibit flux variations in the wide, continuum spectrum, keeping approximately the overall spectral shape. The broad emission lines are also found to vary. Good correlation of the continuum and broad-line variations, with a well defined time lag, is found, which probably is the best evidence for the photoionization model in BLRs (Peterson 1988[129])

With the photoionization model, the time delay between the flux of continuum and lines may provide crucial information on the size of the BLR; light delay time is given  $\tau = r/c$  for a simple spherical model for example. Early results along this idea showed that more closely separated monitoring is required (e.g. Peterson 1988[129]). Several recent results of large collaborations (Clavel et al. 1991[25]; Peterson et al. 1991[130]), intermediate ones (Netzer et al. 1990[121]), and small groups (Koratkar & Gaskell 1991[79]; Stripe & de Bruyn 1991[164]) tend to give somewhat smaller dimensions, and correspondingly give higher electron densities in the BLRs than the results from the diagnostics technique quoted above. The discrepancies are not unreasonably large, hence may not be a fundamental problem, possibly more detailed models may solve this problem.

The "time-delay mapping" results suggest that the higher ionization lines, such as CIV are emitted in the closer vicinity of, and the collisionally de-excited lines CIII] are emitted further from the nucleus, consistent with the idea that the ionization and electron density decrease with increasing distance. Further researches are currently going on in this particular area, which may greatly refine the models.

Inter stellar dust plays important rolls in the extinction effect on the emission-line ratios in nearly every AGN. On average, Seyfert 2 galaxies are more heavily reddened, indicating that they have higher dust content (Dahari & De Robertis 1988[29]). Infrared emission from “warm dust” near the nucleus, which converts significant amount of the ultraviolet and optical radiation to infrared thermal emission, is also essentially ubiquitous in AGNs (Sanders et al. 1989[152]). On average, the thermal infrared is stronger in the Seyfert 2s than Seyfert 1s.

### 2.3 Cylindrical structure and Unified model

It has long been supposed that the characteristic structure of AGNs has cylindrical symmetry rather than spherical (Shields 1977[158]; Osterbrock 1978[123]). The main observational support for this geometry is that VLA high-resolution radio maps of many Seyfert galaxies found the radio jet structures in the close vicinity of the nucleus (Wilson & Ulvestad 1982[206]; Ulvestad & Wilson 1989[182]). High spatial-resolution optical studies of the nearest objects show that the strong [O III] emission, characteristic to AGNs, is strongly associated with these radio jets (Whittle 1985[199]).

It is very unlikely that material from the host galaxy can arrive at the central AGN with zero angular momentum; the nonzero angular momentum implies a cylindrical symmetry, presumably with the momentum axis aligned to the jets directions.

The energy source in AGNs is most likely to be attributable to the deep gravitational potential. The most plausible scenario is that gravitational energies are released in an accretion disk of the infalling gas toward the center, before the gas disappears into a horizon of central black hole (Lynden-Bell 1969[93]; Rees 1984[140]). Note that it is not necessary that the axis of the central part of the AGN be aligned with the overall galaxy, as are indicated in most of the jet direction (Tohline & Osterbrock 1982[168]). Many galaxies, including our own, have warps near their centers, and probably the infalling gas merges into the interstellar medium in a continuous warp, shifting the symmetry axis of the inner part of the host galaxy to the jet direction at the center (Sanders et al. 1989[152]).

Antonucci & Miller (1985[3]), discovered that the optical polarized radiation from the Seyfert 2 galaxy NGC 1068 shows broad  $H\beta$  and Fe II emission features, like the BLR spectra of Seyfert 1s. They interpreted that there is a “hidden BLR” in the nucleus of NGC 1068, whose radiation is not directly seen from us, obscured by matters closely surrounding the central engine. Photons scattered by free electrons at above and below the

obscuration (figure 1) torus can only reach to us, hence are polarized. An observational fact that the position angle of polarization is perpendicular (to within observational error) to that of the jet further strengthens the scenario that photons from the hidden BLR are scattered out along the axis of the jets.

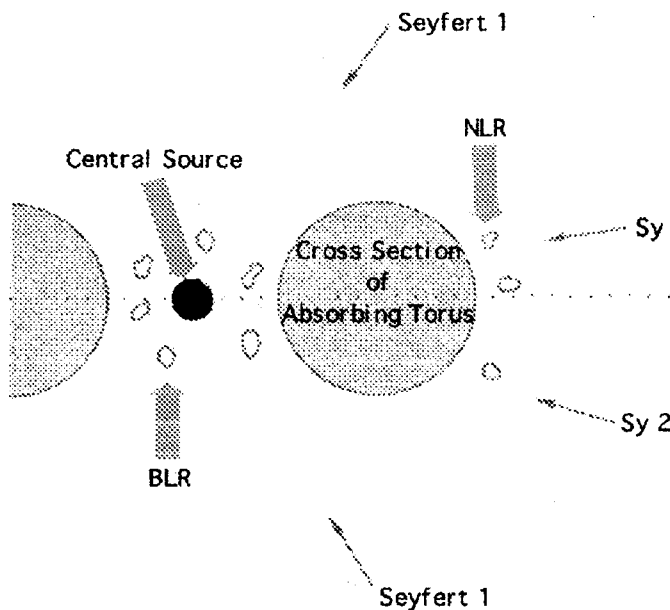


Figure 1: A unified model for Seyfert galaxies

An absorbing torus with a radius of a few pc surrounds the radiating nucleus. Inside the torus are the fast moving clouds of the Broad Line Region and outside the slower clouds of the Narrow Line Region.

Miller and Goodrich (1990[107]) have observed similar features in several other Seyfert 2 galaxies. The directions of the polarization are perpendicular to either the axis of the jets, or the elongated structure of the radio image.

The “ionization cone” along the axis of the jets may have smaller optical depth than in the equatorial plane, because there is less gas along the axis than in the equatorial plane or “torus”. This picture has been established with further observations (Miller, Goodrich, & Matthews 1991[108]). Suppose that we observe from the direction of the axis, NGC 1068 would be found to show a Seyfert 1 spectrum. Thus it would be reasonable to assume that all Seyfert galaxies may have the “universal” structure (Krolik & Begelman 1986[85], 1988[86]). Based on this hypothesis and on the number distribution of Seyferts 1, 1.5, 1.8, 1.9, and 2 within the identical and well-studied field, Osterbrock & Shaw (1988[128]) derived an opening angle to be approximately  $70^\circ$  for the “typical” ionization cone. Although a significant fraction of AGNs do have this structure, whether it is universal structure in all AGNs or not is still an open question.

## 2.4 Observed X-ray properties of Seyfert galaxies

One of the most important discoveries of the early days of X-ray astronomy (Elvis et al 1978[40]) was that X-rays are commonly found from AGNs and that a large fraction of energy from AGNs is radiated in the X-ray band. In fact, X-ray emission can be considered to be one of characteristics of AGNs on the classification. The X-ray properties of AGNs obtained before ASCA have been well reviewed by Mushotzky et al (1993[114]).

X-ray survey observations, typically in the 2-10 keV band, discovered more X-ray emitting type 1 Seyfert galaxies per unit volume than found in other wavelength band (Danese et al 1986[30]). In the 0.2-2 keV band, the surface density of X-ray discovered quasar is equal to or larger than that of optically discovered objects (Shanks et al 1991[157], Boyle et al 1992[22]). The X-ray flux shows a faster variability than any other wavelength ranges (see e.g. McHardy 1990[106]), which indicates that X-rays are originated from a small region in the close vicinity of the central object. Since a large fraction of the luminosity appears in the X-ray band and X-rays are likely to be attributable to the innermost regions of the black hole, detailed X-ray spectroscopy and timing observations undoubtedly provide crucial roles for understanding the active galaxy phenomenon.

### 2.4.1 Hard X-ray spectra of Seyfert 1s

Single power-law fits to the spectra of Seyfert 1s in the 2-20 keV band give photon indexes ( $\Gamma$ s) around 1.7 with small scatter of  $1\sigma$  width of 0.013 (Mushotzky 1984[116]; Halpern 1982[57], Turner & Pounds 1988[175], Awaki et al 1991[10], Nandra 1991[118]). Broad line radio galaxies (BLRGs) also show nearly the same X-ray spectral shape as Seyfert 1s (Mushotzky 1984[116]). Accordingly, the photon index of  $\Gamma = 1.7$  have been regarded to represent an intrinsic spectral slope, hence called as the "canonical index". Recent observations, however, indicate that the canonical index may not represent the intrinsic spectral slope, but would represent an averaged shape of a steeper intrinsic spectrum of  $\Gamma \sim 2.0$ , and an additional flatter component, which comprise preprocessed photons in materials close to the central source.

Long exposure observations with the Ginga satellite (Pounds et al 1989[137], 1990[136]; Matsuoka et al 1990[100]; Awaki et al 1991[10]; Nandra et al 1991[120]) have shown that the Fe line emission features at  $\sim 6.4$  keV, attributable to fluorescence of cold material, are commonly found in Seyfert 1s spectra. The equivalent widths (EWs) are largely scattered

in the range of  $50 < EW < 350$  eV, although the errors are large (Nandra 1991[118], Awaki et al 1991[10]). No apparent correlation of the line strength to the line-of-sight column density is found. The mean line energy of  $\langle E \rangle = 6.4$  keV is consistent with a fluorescence from low velocity and cold materials (Nandra 1991[118], Awaki 1991[7]); generally, a line at 6.7 keV, as expected from thermal emission, can be excluded. Broad lines of  $\sigma \sim 0.7$  keV give better fit than narrow lines for about 20% of the Seyfert 1s, and broad lines around this value cannot be excluded in any of the Ginga Seyferts (Nandra 1991[118]). Suppose that the lines are attributable to fluorescence from cold materials, the large EW indicates that a significant fraction of the solid angle open to the central source (continuum flux source) should be filled with materials of column density  $> 10^{22.5}$  H atoms/cm<sup>2</sup> (Inoue 1985[66], Makishima 1986[95], Matt et al 1991[102], George & Fabian 1991[51]). This picture, however, generally conflict to the absence of large absorbing material along the line of sight (Pounds et al 1989[137]).

Pounds et al (1990[136]) summed 12 separate Ginga AGN spectra from 9 AGNs to increase the signal-to-noise (the so-called Ginga-12 sample) and found, other than the Fe K line feature, data decrement between 7-8 keV and a flattening of the spectrum at higher energies from the best-fit single power-law model. Since then, the flattening at higher energies has been found even in individual objects with high signal-to-noise observations, such as IC4329A (Piro et al 1990[134]), hence appears to be common features in Seyfert 1s (Nandra 1991[118]). The flattening (here and after the "hard tail") can be explained as the decrease of the spectral index of 2-10 keV band to that of the 10-18 keV and is  $\delta\Gamma \sim 0.5$  on average (Nandra 1991[118]).

The Fe K line and "hard tail" feature are consistent with the scenario that the primary X-rays are reprocessed (or "reflected") by optically thick materials, possibly the putative accretion disk, extending a substantial solid angle seen from the central X-ray source (Lightman & White 1988[92], Guilbert & Rees 1988[56], George & Fabian 1991[51], Matt et al 1991[102]).

The reflection albedo is energy dependent. At low energies of  $E < 2$  keV, since many elements (C,N,O) will photoelectrically absorb incident X-rays, few photons can only be reflected. The albedo increases at higher energies due to the decreasing abundance of the higher Z elements, materials for photoelectric absorption at higher energies. Iron is the heaviest and abundant element that can significantly affect the reflection feature; this make a marked "pseudo-absorption feature" in the reflected spectra in the 7.1-9 keV band

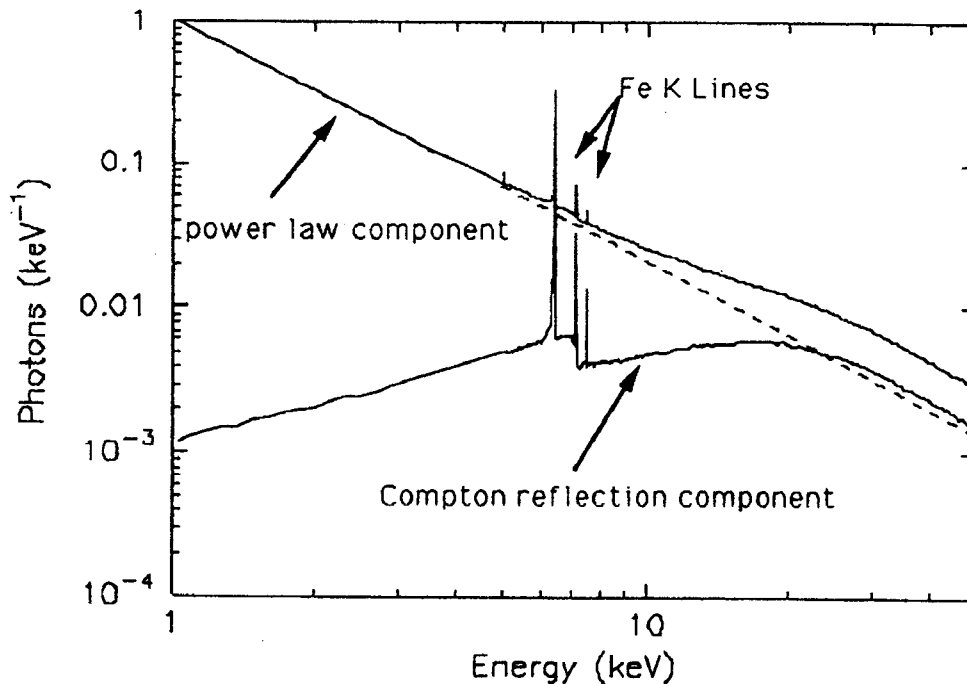


Figure 2: Compton reflection model

The theoretical distribution of flux from a Compton reflection model (George & Fabian 1991[51]).

associated with a Fe  $K\alpha$  fluorescence line with a predicted equivalent width of  $\sim 150$  eV.

At even higher energies, Compton-down-scattering and the decrease of the scattering cross-section deplete the number of reflected photons, hence make a broadband spectral bump with peaks at  $\sim 20 - 30$  keV. Thus reflection by materials lying out of the line-of-sight, provides a self-consistent explanation to the complex features of Fe  $K\alpha$  line, the decrement at  $\sim 8$  keV and the high energy excess. This so-called Compton reflection model introduces four new free parameters into a spectral fit: the fraction of reflected photons [essentially the solid angle covered by the scatterer ( $\Omega/4\pi$ )], the inclination angle of the scatterer to the line-of-sight, the metal abundances, and the ionization state of the scatterer. Figure 2 shows the Compton reflection model used in the fit to the Ginga-12 spectrum. This model gives adequate fit, with a intrinsic power-law spectrum of  $\Gamma = 1.9$  steeper than 1.7, a solid angle of  $\Omega/2\pi = 1.5$  (i.e. indicative of a flared disk) viewed close to face on, and iron abundance of twice of solar (Pounds et al 1990[136]).

An alternative scenario to explain the observed Fe K-edge and high energy excess is

that the central X-ray source is partially covered by cold, dense material, the idea firstly proposed to explain the “soft excess” in NGC 4151 (Holt et al 1980[63]).

In this scheme a fraction (which may be as much as  $\sim 98\%$ ) of the photons seen by the observer are absorbed by thick [ $N_{\text{H}} > 10^{23}$  atoms/cm<sup>2</sup>] materials (Matsuoka et al 1990[100], Piro et al 1990[134]), while the rest photons are unaffected by the absorption. This scenario requires a large column essentially opaque below  $\sim 6$ keV, hence a simple power-law fit to the overall spectrum has an apparent excess above this energy. The large column density material will also produce an iron edge feature, with an optical depth considerably larger than that predicted by the low energy absorption.

Since the reflection and partial covering models have slightly different spectral shapes, these can in principle be distinguished. However, even the Ginga spectra of most of the AGN allow no conclusive test (e.g. Piro et al 1990[134]).

In the hard X-ray selected samples (e.g. Piccinotti et al 1982[132]) a significant fraction of all AGNs exhibit large column densities of cold materials in the line of sight to be  $N_{\text{H}} > 10^{22}$  atoms/cm<sup>2</sup>. However, it now has become clear that almost all of the objects that show such absorption can be classified as either transition objects between Seyfert 1 and 2 galaxies (Seyfert 1.5), Seyfert 2s. or narrow emission line galaxies. [NELGs, which originally were objects selected on the basis of their hard X-ray emission (Wilson 1979[204]), were subsequently found to have strong narrow emission lines, and are now thought to be strongly related to Seyfert 2s.]. Thus the occurrence of large absorption by cold matter in “true” Seyfert 1 galaxies may be rather rare.

#### 2.4.2 Hard X-ray spectra of Seyfert 2s

Although the spectral shape of the 2-20 keV continuum of Seyfert 2s is similar to that of Seyfert 1s (Kruuper et al 1990[88]; Awaki et al 1990[15], 1991[10]), there are significant differences in the amount of X-ray absorption by cold material; with the singular exception of NGC 1068 (Marshall et al 1992[97], Elvis & Lawrence 1988[39], Monier & Halpern 1987[109]), all of the X-ray detected Seyfert 2s show evidence for strong absorption by cold material (Awaki et al 1991[10]).

In the unified model, the apparent lack of strong absorption in NGC 1068 implies paradoxically that the actual column density is greater than  $10^{24}$  atoms/cm<sup>2</sup>, giving the highest inferred column density among all X-ray Seyfert 2s. The high column densities in Seyfert 2s lead to the observational facts of significantly fainter soft X-ray fluxes than

those of Seyfert 1s. Although their unabsorbed X-ray luminosities may well be similar to those of the low luminosity Seyfert 1s (Awaki et al 1991[10]), there exist a few intrinsically high luminosity Seyfert 2s (Lawrence 1991[89], Mulchaey et al 1992[112], Remillard et al 1993[141], Awaki et al 1991[10]). Some narrow line radio galaxies (NLRGs) such as Cen-A, Cyg-A (Arnaud et al 1987[6]; Ueno et al 1994[179]), IC 5063 (Koyama et al 1992[82]), and 3C109 (Allen & Fabian 1992[1]) also show high X-ray column densities with the same spectral indexes as Seyfert 1 galaxies. This is consistent with unification schemes in which the NLRGs and the broad line radio galaxies (such as 3C382 and 3C111) are the radio bright versions of Seyfert 2s and Seyfert 1s respectively.

A large fraction of the X-ray detected Seyfert 2s show strong Fe K lines (Koyama et al 1989[83], Awaki et al 1990[15], Marshall et al 1992[97]), with an equivalent width (EW) up to 2 keV in the most extreme case of NGC 1068. In the two objects with moderate resolution spectra (BBXRT and ASCA data for NGC 1068 and Mkn 3), the line feature is complex with significant fluxes of both the fluorescence and recombination lines. The EWs in a larger sample of Seyfert 2s observed with Ginga is largely scattered, overlapping at the lower end with that of Seyfert 1 galaxies, but extending up to much higher equivalent widths than can be explained in the simple reflection scenario.

Whether or not Seyfert 2s show reflection is uncertain due to the poor signal-to-noise. However, some NELGs have been shown to require reflection (Matsuoka et al 1990[100], Bond et al 1992[21], Nandra 1991[118]), and possible presence of the reflection component is reported in a recent reanalysis of the Ginga spectrum of NGC 1068 (Smith et al 1993[161]).

### 2.4.3 Soft X-ray spectra of Seyfert 1s and 2s

The ultraviolet to X-ray spectra of Seyfert 1 type Active Galactic Nuclei (AGN) can be decomposed into two major distinct components: a non-thermal hard X-ray continuum and a broad excess of emission in the ultraviolet. The latter is called the "big blue bump", and is often interpreted as the prime emission from accreting matter.

In the ROSAT band (0.1-2.4 keV), the soft excess above the extrapolation of the hard X-ray spectrum is detected in 90 % of 58 Seyfert 1 type active galactic nuclei (Walter & Fink 1993[189]). Even if some fractions of this soft X-ray excess can be attributed to extended sources (Elvis et al. 1990[38]), the soft X-ray variability observed in several Seyfert 1 type AGN has led to the conclusions that the large fraction of the soft X-ray emission is produced in a small region close to the central active nucleus. The steep,

ultrasoft emission seen in some quasar and Seyfert 1 galaxies may be attributable to a central accretion disk (Wilkes & Elvis 1987[200]; Turner & Pounds 1989[177]). Partial covering of the central source by a patchy absorber has been proposed to explain the soft excesses seen in NGC 4151 (Holt et al. 1980[63]; Pounds et al. 1986[138]) and NGC 2110 (Turner & Pounds 1988[176]). Extended soft X-ray emission on scales of hundreds to thousands of pc could account for the observed excesses since such extended emission has been found in three out of five Seyferts with sufficiently good Einstein HRI data (Elvis, Briel, & Henry 1983[37]; Elvis et al. 1990[38]) and in ROSAT HRI observations of NGC 1068 (Wilson et al. 1992[205]). Einstein SSS observations of Seyfert galaxies suggest that emission line features centered around 0.8 keV may account for some of the observed excesses (Turner et al. 1991[174]).

The 0.1-3 keV flux in Seyfert 2s is clearly distinct from the heavily absorbed 3-20 keV spectra. The large intrinsic column density determined with the 3-20 keV band spectra would, completely absorb any intrinsic soft X-rays such as is seen in Seyfert 1 galaxies (Awaki 1992[8]). Thus the observed soft component may not be unabsorbed fraction of the hard energy component, nor is the soft excess seen in Seyfert 1s.

In the molecular torus model, a soft excess is expected in Seyfert 2's since the nuclear X-rays can be scattered into our line of sight. If the scatterers are electrons, the nuclear X-rays radiate isotropically and there is little or no photoelectric absorption by the scattering medium, the observed soft X-ray continuum should have the same spectral shape as the (unabsorbed) nuclear X-ray source, with reduced fluxes of a factor of  $\tau_{\text{electron}}(\Delta\Omega/4\pi)$ , where  $\tau_{\text{electron}}$  and  $\Delta\Omega$  are the electron scattering optical depth and the open angle for the scatterers at the nucleus. In addition to the scattered photons, reprocessed photons in the scattering medium are expected. Some Seyfert 2's have a large equivalent width of Fe K  $\alpha$  line (Koyama et al. 1989[83]; Awaki et al. 1991[10]; Marshall et al. 1993[96]), which may be attributable to a combination of scattering and fluorescence (Krolik & Kallman 1987[87]). Band et al.(1990[18]) have calculated the amount of associated Fe L emission expected for NGC 1068. However, a substantial contribution to the soft flux of NGC 1068 is now known to arise from an extended starburst region (Wilson et al 1992[205]; Ueno et al 1994 [180]).

#### 2.4.4 X-ray time variability

X-ray emission shows the shortest timescales for AGN variability among all the wave length band (McHardy 1990[106]; Grandi et al 1992[54]). Since substantial variability on timescales shorter than the light crossing time of the source can not be expected (Terrell 1967[167]), the time scale gives an upper limit to the size of  $R < c\delta t$ . Assuming a source size to be 5 Schwarzschild radii, this can be translated to a limit on the mass of  $M < 2 \times 10^6 \delta t_{100} M_{\odot}$ , where  $\delta t_{100}$  is the variability timescale in units of 100 seconds. The variability can also be used to derive the conversion efficiency,  $\eta$ , of the accreting matter to the luminosity (Fabian 1979[44]). A luminosity change of  $\delta L$  in a time of  $\delta t$  implies an efficiency of  $\eta = 0.05 \delta L_{43} / \delta t_{100}$ , where  $\delta L_{43} = \delta L / 10^{43} \text{ergs}^{-1}$ . Nuclear reaction processes have a maximum efficiency of  $\eta \sim 0.007$ ; gravitational energy release on accretion gives  $\eta = 0.057$  for Schwarzschild or 0.32 for extreme Kerr metrics. Several AGN require efficiencies larger than those produced in nuclear reaction processes, providing the strongest evidence to date that AGNs are indeed powered by accretion (Fabian 1992[45]).

The Aries-V sky survey made clear that significant fraction of the Seyfert 1 showed a large amplitude ( $\delta I / I > 1$ ) variability on time scales of days (Marshall et al 1981[98]). Recent reanalysis of the EXOSAT results (Grandi et al 1992[54]) revealed that  $\sim 40\%$  of AGN in a hard X-ray selected sample, show variability on a time scale of less than one day. On longer timescales (typically weeks to months) 97% of the same sample showed significant variability.

The NELGs, like the Seyfert 2 IRAS 18325-5926 (Awaki 1991[7]), seem to show the same hard X-ray variability characteristics as the Seyfert 1s. This suggests that, in all these cases, most of the the 2-20 keV photons directly come from the central object, but are not due to scattered radiation.

However, as noted by Wandel & Mushotzky(1986[190]) Seyfert 2s seem to vary more slowly than Seyfert 1s, if normalized to their dynamical mass. Mulchaey et al (1992[112]) explained the apparent difference to be the supporting evidence that the true optical-UV luminosities of Seyfert 2s have been underestimated, in agreement with the unified model.

At soft X-ray energies, the emission is expected to be scattered radiation and thus tend to vary slowly. This is indeed the case for NGC 1068 (Monier & Halpern 1987[109]). A spectacular example of this energy dependent variability is NGC4945 (Iwasawa et al 1993[71]), which shows rapid variability at high energy and little if any variability at  $E < 5\text{keV}$ .

## 2.5 Starburst galaxies

In Seyfert 2s, a possible starburst activity may be a source of the soft X-ray flux. Accordingly, we quickly review starburst galaxies .

The epoch in the life of a galaxy when the star formation rate(SFR) significantly exceeds the past averaged star formation is called the "starburst" (Junkes et al. 1995 [74]). Signature of the starbursts are large values of surface brightness in many wavelength, which may be produced by the enormous energy release of massive stars within short timescale.

A number of nearby galaxies, such as M82 and NGC253, show evidence for bursts of massive star formation in their nuclei (Rieke & Lebofsky 1979[143]; Rieke et al. 1980[144]; Jones & Rodríguez-Espinosa 1984[73]). These starburst galactic nuclei were discovered primarily through infrared observations. They are characterized by their observed mid- and far-infrared excesses, attributed to the re-radiation from dust heated by ultraviolet radiation from hot, young stars , and by several emission features in the infrared spectrum (Gillett et al. 1975[52]; Russell et al. 1977[149]; Willner et al. 1977[201]). These infrared features do not appear in the spectra of galaxies other than those with giant H II region nuclei, i.e., starburst nuclei (Roche & Aitken 1985[147] and references therein).

The region of the massive star formation or starburst also show X-ray emission (Junkes et al. 1995[74]). The integral X-ray luminosity is composed of individual sources like stars, neutron star ( or black hole ) binaries with high-mass (HMXRBs) and low-mass (LMXRBs) companions and supernova remnants, and is partly attributable to a diffuse thermal emission from the hot interstellar medium (ISM) (Fabbiano 1989[42]). Massive stars are the progenitors of type II supernovae which, together with stellar winds, supply large amounts of energy into the ISM. The ISM is heated to temperatures of the order of  $10^6$ - $10^7$  K and radiates by thermal emission in the soft X-ray regime of 0.1-1keV.

### 3 Instrumentation

#### 3.1 ASCA

The atmosphere of the earth blocks the cosmic X-rays by photoelectric absorption, hence, we are required to use balloons, rockets, or satellites for the observations of cosmic X-ray sources.

ASCA(Astro-D), the fourth Japanese X-ray astronomy satellite, was launched by the Institute of Space and Astronautical Science (ISAS) on 1993 February 20, with the M-3S-II rocket, and put into an approximately circular orbit with a perigee and apogee of 520 and 620 km, respectively, and an inclination of  $31.1^\circ$ . The orbital period is approximately 96 min. The schematic view of the ASCA satellite is show in figure 3.

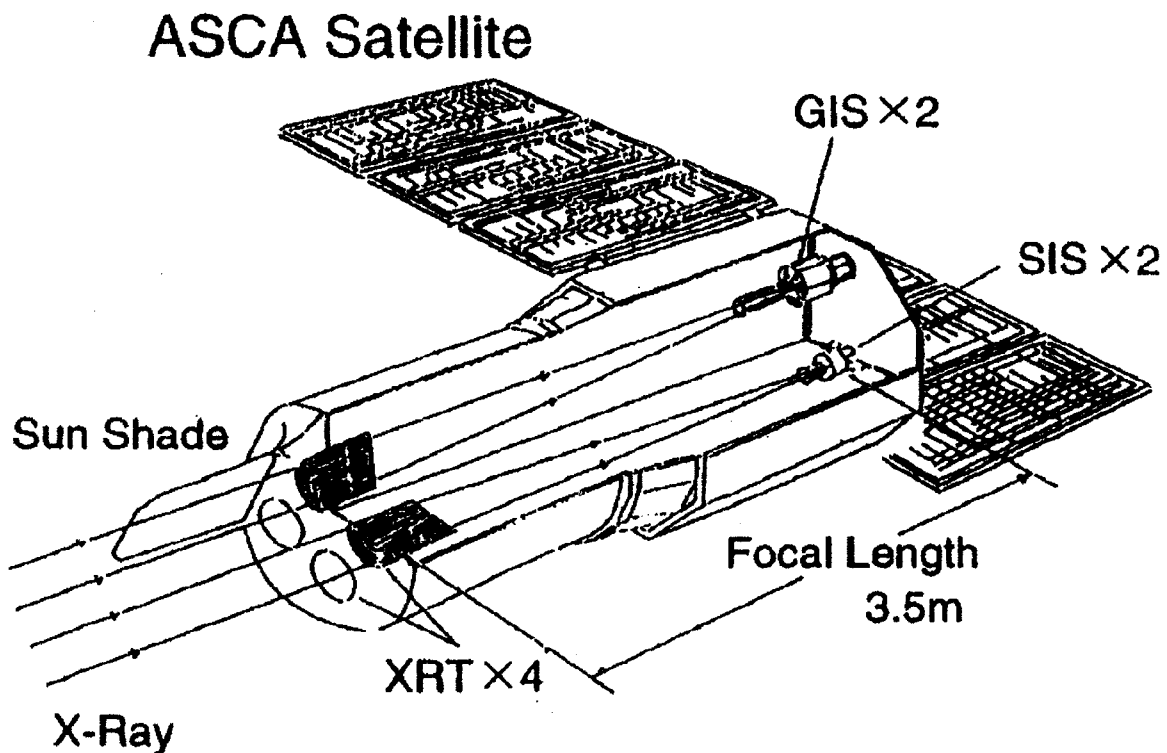


Figure 3: The schematic view of the ASCA satellite

Four focal plane detectors ( SIS $\times$ 2, GIS $\times$ 2) are indicated in the figure. Four X-ray telescope (XRT) are also shown.

The spacecraft mass is 417 kg, and its length is 4.7 m along the telescope axis. The spacecraft is three-axis stabilized; the pointing accuracy is approximately  $30''$  with a sta-

bility of better than  $10''$ . Orientation of the spacecraft is limited by the power constraint that the direction of the solar paddles must be within  $30^\circ$  from the Sun. This limits the observable sky at a time in a belt within which the Sun angle is between  $60^\circ$  and  $120^\circ$ . Thus the entire sky is accessible every half year.

The scientific instrumentation of ASCA consists of X-ray telescopes and focal plane detectors, as described below.

### 3.2 X-ray telescopes

ASCA carries four identical grazing-incidence X-ray telescopes (XRT) each equipped with an imaging spectrometer at its focal plane. The telescope utilizes multi-nested (119 layers) thin-foil conical optics, a technology developed by Serlemitsos et al (1995[156]). This technology allows maximum use of the aperture for X-ray reflection, and enables a light-weight large-effective-area X-ray telescope. The angular resolution of the telescope is modest, with a half power diameter (diameter which encircles 50% of the photons of a point source image) of approximately  $3'$ . However, the point spread functions has a cusp-shaped peak, and 20 % of photons are concentrated within a circle of  $1'$  diameter, producing a sharp image core. This feature allows us to resolves two sources separated by  $1'$ .

The focal length of the telescopes is 3.5 m. These telescopes are mounted on an extendible optical bench. Because of the limited length available within the rocket nose fairing, the optical bench was held inside the spacecraft during launch and extended by 1.2 m in orbit to achieve the designed focal length.

### 3.3 Focal plane detectors

The focal plane detectors are two CCD cameras (Solid-state Imaging Spectrometer, or SIS) and two gas scintillation imaging proportional counters (Gas Imaging Spectrometer, or GIS). All four detectors are operated simultaneously all the time, and data obtained from each of them are separately available.

The SIS has superior energy resolution, with resolving power  $E/\Delta E$  of  $\sim 50$  at 6 keV, and  $\sim 20$  at 1.5 keV, and is sensitive down to 0.5 keV ( $\Delta E$  is FWHM). The GIS energy resolving power is  $\sim 13$  at 6 keV and  $\sim 7$  at 1.5 keV. The GIS is insensitive below  $\sim 0.8$  keV because of a  $10 \mu\text{m}$ -thick beryllium window, but has a higher detection efficiency above  $\sim 3$  keV than the SIS. Therefore, the SIS and the GIS have complementary advantages with

respect to  $E/\Delta E$  and detection efficiency at high energies. The SIS has a square field of view (f.o.v.) of  $20' \times 20'$ , whereas the GIS has a larger circular f.o.v. of 50' diameter. The performance is summarized in table 1.

Table 1: Performance of SIS and GIS

	SIS	GIS
Covered Energy band	0.2-10 keV	0.7-15 keV
Energy resolution at 5.9 keV	2.1%	7.9%
Field of View	$20 \times 20$ arcmin <sup>2</sup>	radius $\sim$ 50arcmin
Pixel size	27 $\mu$ m	0.5 mm*
Spatial resolution <sup>†</sup>	$\sim$ 3arcmin	$\sim$ 3arcmin
Maximum time resolution	16 sec(4CCD mode)	60 $\mu$ sec (PH mode)
Maximum count rate	500 cts/sec	10000 cts/sec

Notes:

\* Virtual pixel in the signal process.

† When used with the XRT.

## 4 Observations and results of individual sources

### 4.1 The log of the ASCA observations

We have observed Seyfert 2 and starburst galaxies listed in table 2. For each target, we listed the name, position, type, recession velocity, and date of observation in the table. The presence or absence of previous observations and some remarks are summarized in table 3, while the distances and the Galactic absorption column are listed in table 4. Through this paper, we assume the Hubble constant to be  $H_0 = 50 \text{ km/s/Mpc}$ .

Table 2: Observation log

Target Name	Position ( $\alpha$ , $\delta_{2000}$ )	Type	Helio. radial velocity	Date
<b>Type 2 Seyferts</b>				
IC 5063	(313.011, -57.071)	SA(s)0+, Sy2	$3402 \pm 6 \text{ km/s}$	25,27 Apr 1994
NGC 4507	(188.904, -39.909)	SAB(s)ab, Sy2	$3523 \pm 12 \text{ km/s}$	12 Feb 1994
NGC 1808	( 76.926, -37.513)	(R' 1)SAB(s:)b, Sy2	$989 \pm 6 \text{ km/s}$	26 Feb 1994
NGC 1667	( 72.155, -6.320)	SAB(r)c, Sy2	$4547 \pm 17 \text{ km/s}$	6 Mar 1994
NGC 1068	( 40.670, -0.013)	(R)SA(rs)b, Sy2	$1136 \pm 4 \text{ km/s}$	24 Jul 1994
Mkn 463	(209.012, 18.372)	Sy2	$14890 \pm 50 \text{ km/s}^*$	31 Jan 1994
Mkn 1210	(121.025, 5.114)	S?, Sy2	$4046 \pm 10 \text{ km/s}$	18 Oct 1995, and 12 Nov 1995
Mkn 477	(220.159, 53.504)		$11350 \pm 90 \text{ km/s}^*$	4-5, Dec 1995
NGC2110	( 88.047, -7.456)	SAB0-, Sy2	$2284 \pm 32 \text{ km/s}$	12 Mar 1994
PKS B1319-164	(200.602, -16.729)	SB?, Sy1.8	$5152 \pm 54 \text{ km/s}$	18 Jul 1995
NGC 7319	(339.014, 33.976)	SB(s)bc pec, Sy2	$6764 \pm 28 \text{ km/s}$	7 Dec 1994
NGC 4388	(186.444, 12.661)	SA(s)b: sp, Sy2	$2524 \pm 1 \text{ km/s}$	4 Jul 1993
<b>Starbursts</b>				
M82	(148.968, 69.679)	I0	$203 \pm 4 \text{ km/s}$	19-20 Apr 1993
NGC 253	( 11.888, -25.288)	SAB(s)c	$245 \pm 5 \text{ km/s}$	12 Jun 1993
NGC 3079	(150.491, 55.680)	SB(s)c	$1125 \pm 6 \text{ km/s}$	9 May 1993

Notes: The positions, types, heliocentric radial velocity were taken from the NASA/IPAC Extragalactic Database (NED).

\*: calculated from the redshifts of  $0.04968 \pm 0.00015$  (Mkn 463), and  $0.03780 \pm 0.00030$  (Mkn 477).

Table 3: Previous observations and Remarks

Target Name	Einstein	Ginga	ROSAT	Remark*
IC 5063	○	○	○	NLRG
NGC 4507	○	○	○	
NGC 1808		○	○	SyII/H II
NGC 1667		△		SyII/H II
NGC 1068	○	○	○	PBL/IC/H II
Mkn 463	○	×	○	PBL/IC
Mkn 1210				PBL
Mkn 477				PBL
NGC2110	○	○	○	NELG/IC
PKS B1319-164				
NGC 7319	○		○	GroupG
NGC 4388	○	△	○	IC/Virgo

Notes: Circles are detections, triangles are marginal detections or a scanning observation (for N4388), and a cross is below detection limit.

\*: NLRG — Narrow Line Radio Galaxy, PBL — Polarized Broad Line, IC — Ionized Cone, GroupG — contaminated by soft emission of the group of galaxies, Virgo — belonging to Virgo cluster, NELG — Narrow Emission Line Galaxy, H II — with starburst activity

Table 4: Applied distance and Galactic absorption

Target Name	Distance Mpc	reference (see Notes)	Galactic column $10^{20}\text{H atoms cm}^{-2}$	reference (see Notes)
Type 2 Seyferts				
IC 5063	65.3	2	4.8	2
NGC 4507	69.2	1	7.1	1
NGC 1808	10.9	5	2.4	3
NGC 1667	90.9	4	5.5	3
NGC 1068	23.4	1	3.1	1
Mkn 463	302.0	1	2.2	1
Mkn 1210	81.0	4	3.5	3
Mkn 477	227.0	4	1.3	3
NGC2110	45.7	1	18.0	1
PKS B1319-164	103.0	4	5.5	3
NGC 7319	135.3	4	7.5	3
NGC 4388	27.0	2	2.7	2
Starbursts				
M82	8.4	2	4.3	2
NGC 253	3.0	2	1.3	2
NGC 3079	32.8	2	0.84	2

## Notes:

1. From Kruper, J.S., Urry, C.M., and Canizares, C.R., 1990, *ApJS*, 74, 347, using a Hubble constant of  $50 \text{ km s}^{-1}\text{Mpc}^{-1}$ .
2. From Fabbiano, G., Kim, D.-W., and Trinchieri, G. 1992, *ApJS*, 80, 531. Distances are estimated from Tully (1988), or if these were not available from the CfA redshift survey data (J. Huchra 1990, private communication), using Virgo-centric flow corrections as in Knapp, Turner, & Cunniffe (1985). A Hubble constant of  $50 \text{ km s}^{-1} \text{ Mpc}^{-1}$  was assumed.
3. From "The Einstein On-Line Service, Smithsonian Astrophysical Observatory."
4. Using a Hubble constant of  $50 \text{ km s}^{-1}\text{Mpc}^{-1}$  and the redshifts. No correction is made for rotation of the Galaxy, motion relative to the Local Group, and infall to Virgo with velocity  $250 \text{ km s}^{-1}$ .
5. From Dahlem, M., Aalto, S., Klein, U., Booth, R., Mebold, U., Wielebinski, R., and Lesch, H., 1990, *A&A*, 240, 237, using a Hubble constant of " $75 \text{ km s}^{-1}\text{Mpc}^{-1}$ ".

## 4.2 Observation mode, Data Screening and Standard model fitting

Most of the observations and the data screening are essentially the same among the sample galaxies. We therefore summarize these in this section. Unless otherwise mentioned particularly in the sections of individual target, all the data analysis follow these standard procedures.

**Observation mode** The ASCA observations of our sample targets have been performed with the two Solid-state Imaging Spectrometers (SIS0 and SIS1) and the two Gas Imaging Spectrometers (GIS2 and GIS3), all operated parallelly.

**Data Selection and Screening** In most cases, our target is the only brightest source in both the GIS and SIS fields. Then we have extracted spectra from a region of 6' diameter for SIS and GIS. We rejected data obtained under high background environments, selecting the data which satisfied the following criteria: 1) the elevation angle from the Earth edge was greater than 5 degrees, 2) the cut-off rigidity was higher than 6 GeV/c, and 3) the satellite was outside the South Atlantic Anomaly region, and only for the selection of the SIS data 4) the elevation angle from the bright Earth edge was greater than 20 degrees.

**Standard model fitting** The standard model function so far applied to active galactic nuclei is a single-power modified by a photoelectric absorption of cold material with cosmic abundance. The model function is given in the formula 1.

$$F(E)dE = NE^{-\Gamma} \exp(-\sigma(E)N_{\text{H}}) \text{ (photons s}^{-1}\text{keV}^{-1}) \quad (1)$$

where  $N$  and  $\Gamma$  are the normalization factor and photon index, respectively. The parameter of  $\sigma(E)$  is the cross section per hydrogen atom of photo-electric absorption by cold material with cosmic abundance, and is a function of the incident photon energy  $E$ . The hydrogen column density is expressed by the  $N_{\text{H}}$ . In this paper, we also apply this model as the first approximation as well as for a comparison of previous data.

As are found in the following sections, this single component model is rejected for most of our sample galaxies. A double power-law model with a narrow Gaussian component around 6.4 keV (at the rest frame), representing the Fe K-shell fluorescent line seen in

many Seyfert 1 and 2 galaxies, have been then applied. The model function is given in the formula 2.

$$F(E)dE = [N_1 E^{-\Gamma_1} \exp(-\sigma(E, z) N_{\text{H}_1}) + \{N_2 E^{-\Gamma_2} + \text{line}(E, EC, \Delta E, z)\} \exp(-\sigma(E, z) N_{\text{H}_2})] \times \exp(-\sigma(E) N_{\text{Hgal}}) \text{ (photons s}^{-1} \text{keV}^{-1})$$

$$\text{line}(E, EC, Z) = \frac{a}{\sqrt{2\pi}} \exp\left\{-\frac{(E - \frac{EC}{1+z})^2}{2(\Delta E)^2}\right\}$$

where  $N_1$ ,  $N_2$ , and  $a$  are the normalization factors, while  $\Gamma_1$  and  $\Gamma_2$  are the photon indexes.

The parameters  $EC$  and  $\Delta E$  are, respectively, the center energy of the line at the rest frame after the correction using the redshift  $z$  retrieved from table 2, and the line width fixed to be narrower than the energy resolutions of the instruments. When the statistics is large enough to constrain the line width, we set this parameter to be free.

The  $\sigma(E, z)$  is the cross section of photo-electric absorption corrected by the redshift (i.e. representing absorption by material placed around or in the target). The hydrogen column density due to our galaxy is expressed by the  $N_{\text{Hgal}}$ , fixed to the value listed in table 4, where this absorption is applied at the observer frame (i.e. at  $z=0$ ).

### 4.3 Seyfert 2s showing strong low-energy cut offs in the Ginga spectra

IC 5063, NGC 4507, NGC 1808, and NGC 1667

#### 4.3.1 IC 5063 and NGC 4507

**Introduction to IC 5063** IC5063 (PKS2048-57) is a narrow-line radio galaxy associated to a giant elliptical or S0 galaxy at  $z=0.0110$ , with a pronounced dust lane across the nucleus (Colina, Sparks, Macchetto 1991[27]). It is one of the first galaxies in which a large absorption was found with the X-ray spectroscopy by Koyama et al. (1992[82]). They, with Ginga satellite, found that the 2-20keV spectrum of IC5063 is well fitted by a power-law model ( photon index of 1.5 ) with a large absorption corresponding to the  $N_{\text{H}}$  value of  $2 \times 10^{23} \text{H atom cm}^{-2}$ . They also reported the flux variability. The 0.2-3.5 keV flux was estimated to be  $4 \times 10^{-13} \text{ergs s}^{-1} \text{cm}^{-2}$  with the Einstein IPC instruments. However, the origin of the soft X-ray emission has been unclear.

**ASCA observation of IC 5063** IC 5063 was observed on 1994 April 25 and 27. IC 5063 is the brightest source in the GIS and SIS fields of view. The GIS image in the 0.5 – 2 keV band (with a field of view of about 25 arcmin in radius) contains one obvious source in addition to IC 5063 (figure 4). However, in the 4–10 keV image, only IC 5063 is visible (figure 5). After the data screening, the effective exposure time is reduced to 33.1 and 35.6 ksec for SIS and GIS, respectively.

Table 5: Source positions in the ASCA image of IC 5063

	GIS 0.5-2 keV	GIS 4-10 keV	SIS 0.5-2 keV	SIS 4-10 keV	ID
Source	(RA, DEC) <sub>epoch2000</sub>	(RA, DEC) <sub>epoch2000</sub>	(RA, DEC) <sub>epoch2000</sub>	(RA, DEC) <sub>epoch2000</sub>	
A	313.023, -57.065	313.010, -57.069	313.022, -57.068	313.022, -57.068	IC 5063
B	313.037, -56.9178	Not detected	Out of F.O.V	Out of F.O.V	

Note. — The positions are measured in unit of degree.

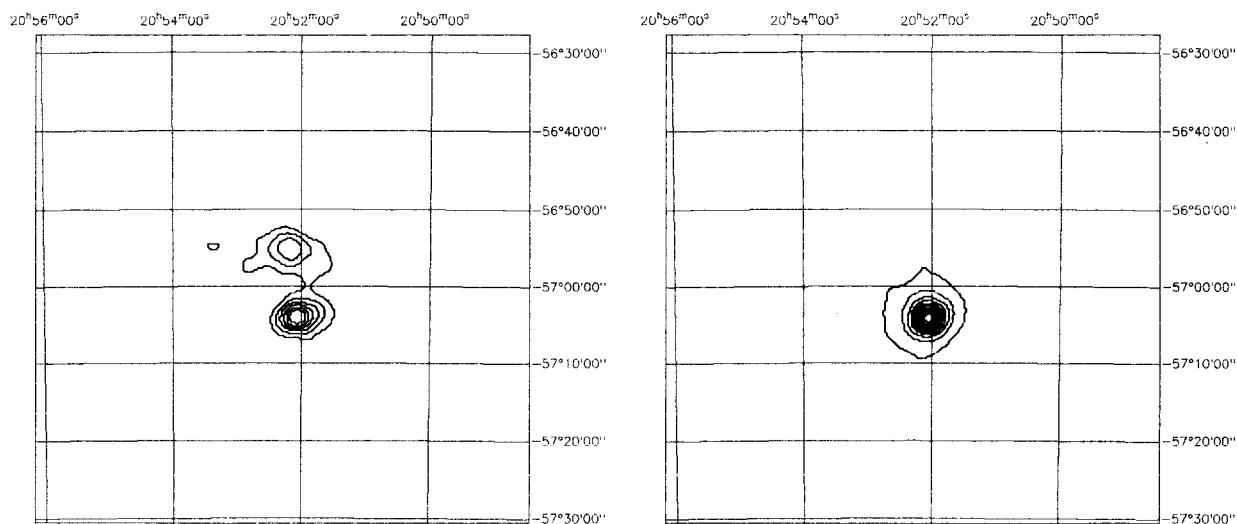


Figure 4: The GIS contour image of IC 5063 in the 0.5 – 2 keV band

The bright lower source is IC 5063, while the upper source has been unidentified yet.

Figure 5: The GIS contour image of IC 5063 in the 4 – 10 keV band

The only bright source is IC 5063.

Grids are drawn in  $(\alpha, \delta)_{\text{epoch2000}}$  coordinates.

**X-ray spectra of IC 5063** The spectra of IC 5063 is shown in figure 49. We can see a drop of the flux around 2-3 keV, which suggesting that the spectral component dominating above 3 keV is heavily absorbed. The presence of the heavily absorbed component is already

reported in IC5063 (Koyama et al 1992[82]) and in other several Seyfert 2s with the Ginga satellite and is interpreted as the direct X-ray from the nucleus seen through thick cold matter. Thus we apply a simple power-law model given in formula 1.

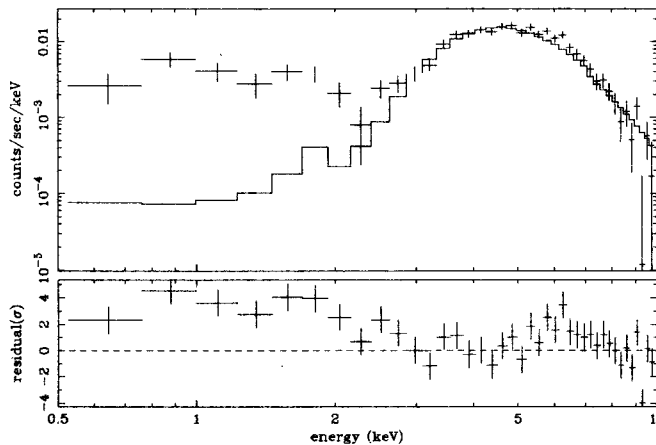


Figure 6: The result of the single power-law model for IC5063

Only the SIS1 spectrum is shown. A solid line shows the model function of the power-law modified by a photoelectric absorption (formula 1). The residuals are shown in the bottom panel. The model was fitted with SIS, SIS1, GIS2, and GIS3 data simultaneously.

This model is rejected with a reduced  $\chi^2$  of 2.61 for 177 degrees of freedom (dof). Nevertheless we show the best-fit model and data for SIS0 in figure 6 in order to see in detail. The best-fit photon-index and hydrogen-equivalent column density are 1.6(1.4-1.8) and  $2.1(1.9 - 2.3) \times 10^{23} \text{H atom cm}^{-2}$ , respectively (here and after, the 90 % confidence range of each fitted parameter is given in the parenthesis after the best-fit value). More flux is seen at soft X-ray energies than expected from a simple extrapolation of the hard X-ray continuum covered by a cold photoelectric absorber, which may require an additional component, hence we add another power-law component for the soft excess. Since, at soft energies, X-ray spectral shape become more sensitive to the absorbing matter because of the increase of photoelectric cross section, we add the Galactic absorption (the expected photoelectric absorption due to interstellar matter in our galaxy) separately. We further add a narrow Gaussian component around 6.4 keV (at the rest frame), representing the Fe K-shell fluorescent line seen in many Seyfert 1 and 2 galaxies. The model function is the same as is given in formula 2.

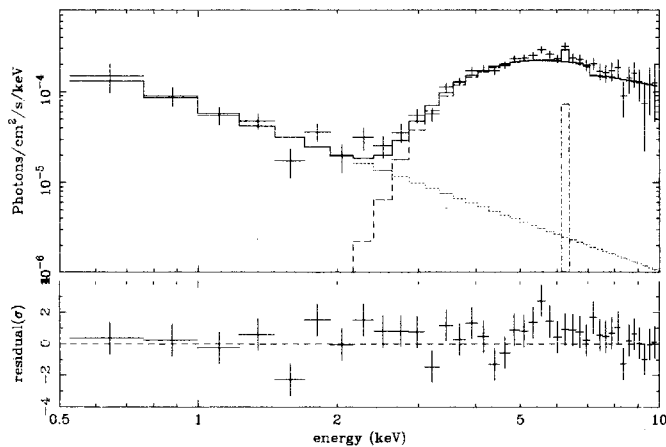


Figure 7: The result of the double power-law model for IC5063

Only the SIS0 spectrum is shown. A solid line shows the model function of two power-law modified by photoelectric absorptions with a narrow Gaussian line (formula 2). The residuals are shown in the bottom panel. The model was fitted with SIS, SIS1, GIS2, and GIS3 data simultaneously.

This model gives a nice fit with the reduced  $\chi^2$  is 1.12 for 172 degrees of freedom (dof). The best-fit model function is shown with SIS0 data in figure 7. The function is deconvolved by the response of the instruments, hence is the intrinsic spectrum of X-rays incident on the X-ray telescope. The best-fit parameters are listed in table 19.

The hard band ( $>3$  keV) flux is dominated by a power-law component having the photon index of 1.8(1.6-2.0) absorbed by the hydrogen-equivalent column density of  $2.4(2.2 - 2.6) \times 10^{23} \text{H atom cm}^{-2}$ , and is referred to as “the hard component”. The soft band ( $<3$  keV) flux, on the other hand, is dominated by the other power-law component with a photon index of 1.9(1.5-2.4) absorbed by the hydrogen-equivalent column density of  $< 1.1 \times 10^{21} \text{H atom cm}^{-2}$ , and is called as “the soft component”. The best fit center energy of line is 6.39(6.24-6.46) at the rest frame, and the equivalent width is 80(38-127) eV.

**Introduction to NGC 4507** NGC4507 is a Seyfert 2 galaxy discovered with Ginga to harbor an obscured X-ray source (Awaki et al. 1991[10]; Awaki 1991[7]). The X-ray continuum of this source is well described by a power-law model with photon index  $\Gamma \sim 1.4$  and a low-energy cutoff ( $\sim 5$  keV) corresponding to a column density of the obscuring matter of  $5 \times 10^{23} \text{H atom cm}^{-2}$ , which is sufficient to hide the broad-line region and the nucleus. The observed spectrum also shows an iron line having an equivalent width of  $\sim 400$  eV, which indicates a large covering factor for the matter around the nucleus (Awaki et al. 1991[10]).

**ASCA observation of NGC 4507** NGC 4507 was observed on 1994 February 12, with the effective exposure time of the SIS and the GIS of about 32.8 ks and 31.7 ks respectively.

In the GIS and SIS images, NGC 4507 has a soft source about 5 arcmin to the northeast. The X-ray position of NGC 4507 and the soft source (Source B) is listed in table 6.

Table 6: Source positions in the ASCA image of NGC 4507

	SIS0 0.5-2 keV	ID
Source	(RA, DEC) <sub>epock2000</sub>	
A	(188.918, -39.920)	NGC 4507
B	(189.019, -39.882)	detected with Einstein

Note. — The positions are measured in unit of degree.

The 0.5-3 keV spectrum of the source B are reproduced by a Raymond-Smith model with a temperature of  $kT = 1.0 \pm 0.1$  keV and abundances of  $0.13 \pm 0.05$  solar. The model gives the observed 0.5-2 keV flux of  $7.3 \times 10^{-13}$  ergs cm<sup>-2</sup>s<sup>-1</sup>. The spectrum also fitted by a power-law model with a photon index of  $3.4 \pm 0.4$ . In the both models, an excess of flux remains above 4 keV.

To compensate contaminations from NGC 4507, we made a background spectrum from a region having the same radius and the same distance from NGC 4507 as the region for Source B and subtracted from the source B spectrum. The excess above 4 keV then disappear, hence, the spectrum is well reproduced by a single spectral component: a Raymond-smith model of  $kT = 0.99(0.92-1.06)$  keV with abundances of 0.05(0.03-0.08) solar absorbed by  $N_{\text{H}} = 1.9(1.5 - 2.4) \times 10^{21}$  H atom cm<sup>-2</sup>, or a power-law model with the photon index of 4.0(3.4-4.7) absorbed by  $N_{\text{H}} = 4.7(3.6 - 6.1) \times 10^{21}$  H atom cm<sup>-2</sup>.

**X-ray spectra of NGC 4507** We have extracted the spectra of NGC4507 from regions of 6' and 5'diameters for SIS and GIS, respectively. Since the soft X-rays would be contaminated by the soft spectra of Source B, we subtracted the background made with the same procedure used for the spectra of Source B. The background subtracted spectra of IC 4507 is shown in figure 50. Like IC5063, the NGC 4507 spectra have a local flux minimum around 2-3 keV, also suggesting the presence of a heavily absorbed component with flux dominated above 3 keV. The presence of heavily absorbed components is already reported in NGC 4507 with the Ginga satellite. Since the overall spectral shape of NGC 4507 are almost identical to those of IC5063, we applied the same spectral fitting procedures as

described for IC5063.

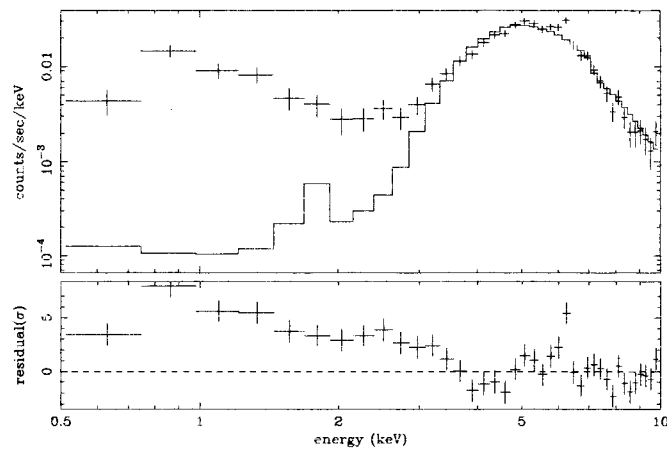


Figure 8: The same as in figure 6, but for NGC 4507.

Figure 8 is the SIS0 data and the best-fit single power-law model (formula 1) with the photon-index and hydrogen-equivalent column density of 1.57(1.41-1.74) and  $3.2(3.0-3.5)$   $H \text{ atom cm}^{-2}$ , respectively.

Figure 9 is the deconvolved spectra of the best-fit two-power-law components and iron line model ( formula 2).

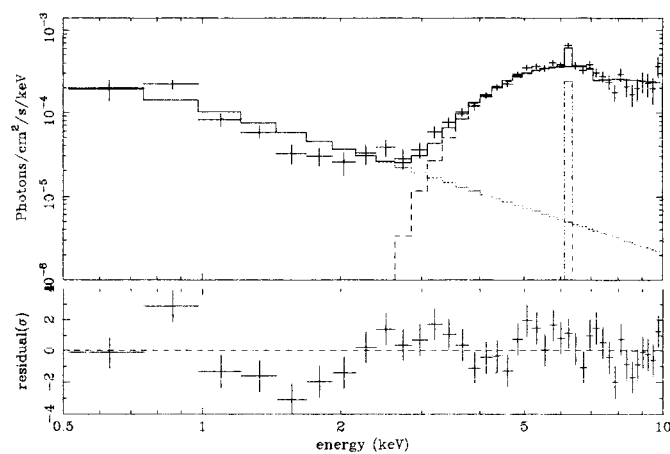


Figure 9: The same as in figure 7, but for NGC 4507

The best-fit parameters are listed in table 19 together with the reduced  $\chi^2$  is 1.54 for 172 degrees of freedom (dof). The hard component has a power-law with a photon index of 1.7(1.4-1.9) and a hydrogen-equivalent column density of  $3.7(3.4 - 3.9) \times 10^{23} \text{H atom cm}^{-2}$ , while the soft component is expressed with a photon index of 1.8(1.6-2.0) and hydrogen-equivalent column density of  $< 2.2 \times 10^{20} \text{H atom cm}^{-2}$ . The best fit center energy of line is 6.29(6.22-6.40) at the rest frame, and the equivalent width of it is 155(118-192) eV.

#### 4.3.2 Discussion for IC5063 and NGC4507: confirmation of strong cutoffs

The ASCA spectra of IC 5063 and NGC 4507 are very similar with each other; both have almost the same fluxes not only at high energies but also at low energies associated with a local minimum around 2-3 keV and moderately strong Fe K lines.

In optical wavelengths, IC 5063 and NGC 4507 exhibit different morphology; IC 5063 and NGC 4507 are "early" and "late" types, respectively. Soft X-rays are found in many "early" type galaxies and are interpreted to be a thermal emission from interstellar hot gas (Forman, Jones, Tucker 1985[49]). Accordingly we may expect additional soft X-rays in the early type galaxy IC5063, but we can see no significant difference in the soft X-rays between IC 5063 and NGC 4507.

We estimate the upper limit of contribution of X-ray emission from interstellar hot gas to the soft component of IC 5063, using the ASCA observations of early type galaxies (Awaki et al 1994[11]).

In the paper, the temperatures of early type galaxies have the mean value of 0.8 keV with a scatter from 0.7 to 1 keV, and metal abundances of 0.3-0.8 solar. First, we fit the soft component with a Raymond-Smith (RS) model, and get the best-fit  $kT$  of 2.9 keV with the metal abundance of zero and no intrinsic absorption. Thus the soft component of IC 5063 favors higher  $kT$  and lower abundance than those of early type galaxies. Alternatively, we fit the soft component to a RS model fixing the  $kT$  to the observed highest value of early type galaxies of 1 keV, and with abundances fixed to the lowest value of 0.3 solar. This mimicked model of early type galaxies nicely reproduces the soft component of IC 5063, but requires the excess of absorption column of  $N_H$  of  $5.6 \times 10^{21} \text{H atom cm}^{-2}$  above the Galactic column. The relatively large absorption is not seen in any early type galaxies so far observed with ASCA. The large absorption effectively flattens the spectrum, hence allows a lower temperature for the soft component of IC 5063 than that with only galactic absorption. We, therefore fixed the intrinsic absorption to zero then the data residuals

appear in the hard portion of soft component(around 1.5-3 keV) as seen in figure 10. This disagreement suggests the interstellar hot gas expected in IC5063, can not account for the whole soft X-ray emission.

Adding the extra component of a RS model with  $kT=1$  keV to the power-law emission having the same photon index as that of the hard component, the RS model accounts only 33% of the 0.5-2keV flux at the maximum; consistent results of no differences between the spectra of IC 5063 and NGC 4507.

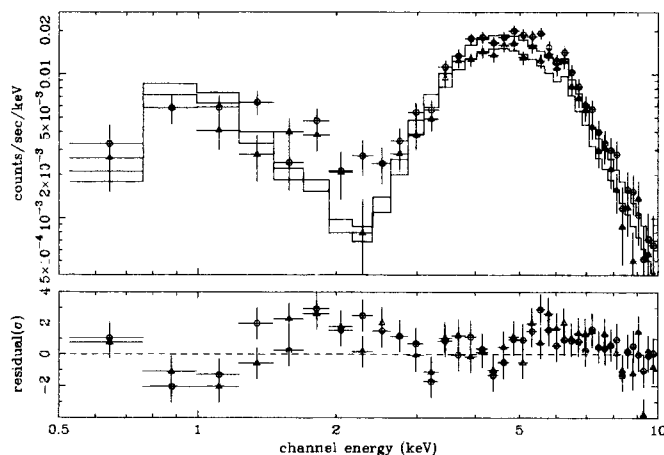


Figure 10: The result of the RS model for the soft component of IC 5063

Circles and triangles show the SIS0 and SIS0 data, respectively. Solids lines show the Raymond-Smith model with  $kT = 1$  keV and the metal abundance of 0.3 solar, convolved by the instrumental response. Only the Galactic absorption was applied to the soft component. This model mimics the X-ray spectra of early type galaxies. Residuals remains around 1.5-3 keV(The bottom panel).

Since IC 5063 and NGC 4507 are bright in hard X-rays among extragalactic sources, previous instruments provided high quality observations of hard X-ray spectra including Fe K lines. We search a long term variability of the hard X-ray properties. The variability of continuum flux is searched in the later section together with other targets.

We compared photon indexes, absorption column densities, and the equivalent widths and the fluxes of Fe K line between the Ginga[82] and the ASCA observations of IC5063, which separated by about 3.5 years. The values and 90% errors are listed in table 7.

The best-fit photon index with ASCA is in the range of the typical values for AGNs,

and is consistent with the Ginga value within the relatively large error. The apparent increase of the best-fit index may be attributable to the limited ASCA energy range, since the possible complexity found in the energy above about 7 keV ( see review) cannot be effectively included with the ASCA.

Since the reflection component found in a number of Seyfert 1 galaxies gives flat power-law index of 1.48 with Ginga (e.g., Nandra & Pounds 1994[119]), we try the fitting of the ASCA spectrum with the photon index fixed to 1.48. This procedure does not change the absorption column and the parameters of Fe K strengths as listed in table 7.

The  $N_H$  of IC 5063 shows no variability, neither change is found even if we fix the photon index to be the Ginga values. The constancy of  $N_H$  means the uniformity of absorbing matter.

To check the variability of the strength of Fe K lines, we compared both the equivalent width and the flux. Equivalent widths(EWs) are independent of the assumed distance , hence are directly related to the physical model of the target , as discussed the later section together with other sources. The EW of IC5063 appears to be decreased, but is marginally constant within errors. In contrast to EWs, the determination of the Fe K line flux is hard subject to the modeling and the variability of the continuum. The EW and flux of Fe K line of IC5063 decrease from Ginga to ASCA observations, although the significance is not high due to the large errors. The best fit Fe line energy with ASCA is 6.39(6.24-6.46) keV confirming the Ginga value ( $6.42 \pm 0.37$ ), and is consistent with the energy of neutral iron.

Table 7: Hard X-ray properties of IC 5063 obtained with Ginga and ASCA

	Observed date	Photon Index	$N_H$ ( $10^{23}$ Atom $\text{cm}^{-2}$ )	EW(Fe K) eV	Obs.flux(Fe K)ph/s/ $\text{cm}^{-2}$
Ginga	2 Oct 1990	1.48(1.34-1.62)	2.34(2.04-2.69)	230(130-330)	4.83(2.71-6.82)E-5
ASCA	25,27 Apr 1994	1.8(1.6-2.0)	2.4(2.2-2.6)	80(38-127)	1.70(0.85-2.62)E-5
ASCA		1.48(fix)	2.1(2.0-2.2)	81(39-127)	1.72(0.83-2.62)E-5

We made the same comparison for NGC 4507 as are listed in table 8. As is the case of IC5063, the photon index with ASCA is larger than Ginga. The increase can be attributable to the limited energy band as mentioned in the comparison of IC 5063.

Bassani et al(1995[19]) mentioned that combined fit including higher energy to the Ginga and the OSSE data by the power-law model with a reflection component gives the best fit photon index of  $1.7 \pm 0.2$ , more or less consistent with ASCA rather than Ginga.

The  $N_{\text{H}}$ , the EW and the flux decreased from the Ginga to the ASCA observations. The change of column density can be explained if the absorbing matter is not uniform and moving across our line of sight. The scale of the irregularity divided by the crossing speed should be less than 3.5 year, the interval time of the Ginga and the ASCA observations. However, Bassani et al(1995[19]), by the simultaneous fitting of the Ginga and OSSE data, gives the smaller values for these parameter than Awaki et al (1991[10]) does with the Ginga data, which make the above argument to be debatable.

Table 8: Hard X-ray properties of NGC 4507 obtained with Ginga and ASCA

	Observed date	Photon Index	$N_{\text{H}}$ ( $10^{23}$ Atom $\text{cm}^{-2}$ )	EW(Fe K) eV	Obs.flux(Fe K)ph/s/ $\text{cm}^{-2}$
Ginga	7 Jul 1990	1.39(1.20-1.52)	5.01(4.57-5.50)	400(350-450)	12.2(10.7-13.8)E-5
ASCA	12 Feb 1994	1.7(1.5-2.0)	3.8(3.5-4.2)	142(104-181)	5.41(3.92-6.90)E-5
ASCA		1.39(fix)	3.3(3.2-3.5)	157(119-196)	5.89(4.58-7.21)E-5

### 4.3.3 NGC 1808 and NGC 1667

**Introduction to NGC 1808** NGC1808 is a highly inclined Sbc pec spiral with several optical hot spots [47]. Véron-Cetty & Véron (1985[187]) claimed that NGC 1808 showed evidence for a composite nature with spectra characteristics of both an active galactic nucleus (AGN: black hole in the standard scenario) and starburst. They suggest that a weak Seyfert nucleus is present surrounded by circumnuclear HII regions. Philips(1993[131]) dismissed the Seyfert classification on the basis of line profiles and ratios. However, Awaki & Koyama (1993[13]) detected X-ray emission of a Seyfert nucleus with the Ginga satellite. High-resolution radio data by Saikia et al.(1990[151]) revealed the existence of a compact core and a ring of star formation regions encompassing the core. Almost all signs of activity are concentrated in the central  $16''$ . The north of the central starburst region of NGC 1808 shows clear signatures of a nuclear outflow ( Koribalski et al 1993[80]).

Jukes et al.(1995[74]) present results from ROSAT PSPC Observations of the nuclear starburst galaxy NGC 1808. The bulk of the X-ray emission comes from the (unresolved) nucleus of NGC 1808. The X-ray spectrum of this galaxy shows almost complete absorption below 0.5 keV, indicating a high intrinsic hydrogen column density towards that source ( $8 \times 10^{21} \text{cm}^{-2}$ ). Model fits for the X-ray spectrum of NGC 1808 indicate that the most of the soft X-rays are radiated from a plasma of temperature of  $\sim 0.5$  keV, or  $6 \times 10^6$  K,

which may be tracing supernova remnants (SNRs) or hot bubbles in the central starburst of NGC 1808. The total X-ray luminosity of  $1.4 \times 10^{41} \text{ erg s}^{-1}$  can be explained by a supernova rate of  $\sim 0.09 \text{ yr}^{-1}$  and a star-formation rate (SFR) of  $\sim 10 M_{\odot} \text{ yr}^{-1}$  in the nuclear starburst region, in agreement with the results of optical and FIR observations.

**ASCA observation of NGC 1808** NGC 1808 was observed on 1994 February 26 with effective exposure time of the SIS and the GIS of about 31.7 ks and 31.8 ks respectively. The ROSAT observations found an X-ray emitting star in the close vicinity of NGC 1808 (Junkes et al.1995[74]). The soft source was separately detected near NGC 1808, and the separation from NGC 1808 is 4.5 arcmin, comparable to the half power diameter of the ASCA SIS image of about 3 arcmin. We estimate that about 10 % of the source flux spills in the region of NGC 1808. In order to subtract the contamination, we selected the background region, in which the spilling flux from the star is equal to that in the NGC 1808 region. After the background subtraction, we estimate that the contamination from the star is less than 1% of the flux of NGC 1808.

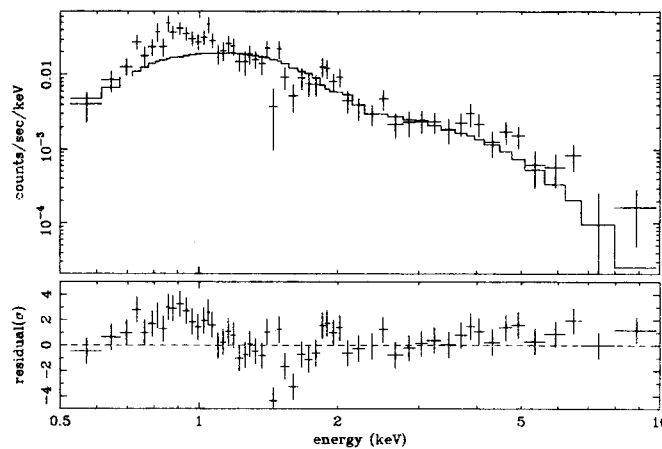


Figure 11: The same as in figure 6, but for NGC 1808

**X-ray spectra of NGC 1808** The spectra of NGC 1808 is shown in figure 51. For the comparison of spectral shapes with other targets we first apply a power-law model (formula 1). The best-fit model function is shown with the SIS0 data in figure 11. The reduced  $\chi^2$  is 2.25 for 169 degrees of freedom (dof). The best-fit photon-index and hydrogen-equivalent

column density are  $2.19(2.05-2.35)$  and  $1.4(1.0 - 1.7) \times 10^{21} \text{H atom cm}^{-2}$ , respectively.

We see emission line at 1.4 keV and 1.82 keV in the SIS spectrum. From the energies, these can be identified as He-like K shell emission of Mg and Si. Furthermore, in the GIS spectrum, we found a prominent line of He-like Si at 1.8 keV. Therefore X-rays from NGC 1808 are attributable to the thin hot plasma of a sub-keV temperature. The extended soft X-ray emission found with ROSAT support the hot plasma origin for the X-ray emission. Thus we fit the spectra with a single temperature RS plasma model, but is rejected, leaving large residual above 4 keV. This suggest an additional component in the high energy band. Accordingly, we performed a two-component model: a RS plasma model at low energies and a power law model at high energies. We have fixed the intrinsic column density for the RS plasma model to be  $0.8 \times 10^{22} \text{H atom cm}^2$ , which is determined with ROSAT. We also examined a thermal emission model plus absorption for the high energy component, taking account of the observational fact that M82 exhibits an absorbed thermal emission of several keV temperature (Tsuru et al. 1994[172]). The result of the fit is listed in table 9. The 90% confidence upper limit of a narrow 6.4 keV line is 600 eV at the rest frame.

Table 9: Results of two component model for NGC 1808

Component	$N_{\text{H}}(10^{22} \text{cm}^{-2})$	$kT(\text{keV})$ or $\Gamma$	Metal abundance(solar)
Soft	0.8(fix)	$kT=0.62(0.59-0.65)$	2(0.7<)
Hard	3 (< 4)	$kT=27(10<)$ or $\Gamma = 1.3(1.0-1.7)$	1(fix)
reduced $\chi^2(\text{dof})=1.73(120)$			

**Introduction to NGC1667** NGC 1667 is a star-forming galaxies. The morphological type and activity class are Sbc and Seyfert 2, respectively [78], which are similar to NGC1808.

**ASCA observation of NGC 1667** NGC 1667 was observed on 1994 March 6, and the effective exposure time for the SIS and the GIS are about 35.1 ks and 37.5 ks, respectively. Since the most of the characteristics are the same as NGC1808, we performed identical data analysis procedure to the NGC1808.

**X-ray spectra of NGC 1667** The spectra of NGC 1667 is shown in figure 52. We found no significant feature although the photon statistics is limited especially in hard energies.

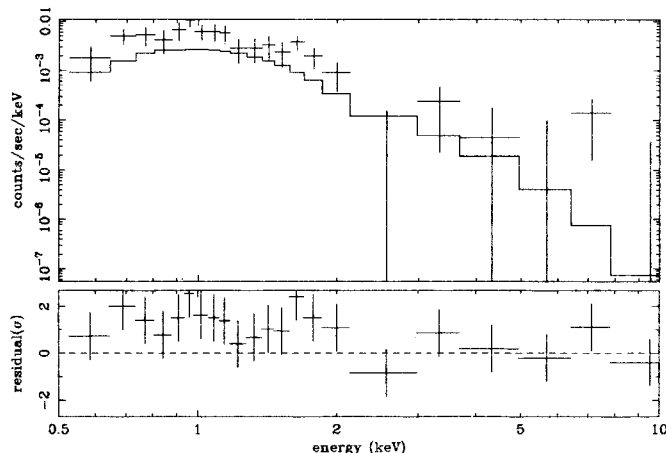


Figure 12: The same as in figure 6, but for NGC 1667

Figure 12 is the best-fit single power-law model (formula 1), with the reduced  $\chi^2$  of 1.55 for 62 degrees of freedom (dof). The best-fit photon-index and hydrogen-equivalent column density are  $3.76(2.46-7.27)$  and  $2.6(0.5 - 8.2) \times 10^{21} \text{H atom cm}^{-2}$ , respectively. The steep slope reminds us a exponential cut-off of thermal spectra. Thus we apply a RS plasma model, and get the temperature of  $kT=0.80(0.69-0.94)$ , the metal abundance of  $0.08(0.03-0.20)$ , and the intrinsic absorption of  $N_{\text{H}} < 3 \times 10^{21} \text{H atom cm}^{-2}$

In both the power-law and the RS model fits, there seems to be an excess at energies  $> 3 \text{ keV}$  although errors are large. We therefore add a power-law component fixing the slope to that determined with Ginga of the photon index of  $1.1 \pm 0.5$  and the absorption of  $N_{\text{H}} = 2.5(< 10) \times 10^{22} \text{cm}^{-2}$ , because the signal-to-noise ratios are too small to let these new parameters to be free.

The fit was improved by  $\Delta\chi^2 = -7$  from the single RS model. The unabsorbed flux of the additional power-law is  $6.7(2.6 - 10.8) \times 10^{-6} \text{photons s}^{-1} \text{cm}^{-2} \text{keV}^{-1}$  at 1keV. The sum of the soft and hard components is  $7 \times 10^{40} \text{ergs s}^{-1}$ , while the hard component alone gives  $6 \times 10^{40} \text{ergs s}^{-1}$  (the absorption-corrected one is  $7 \times 10^{40} \text{ergs s}^{-1}$ ) in the 2-10 keV band. The 90% confidence upper limit of a narrow 6.4 keV line is 2.9 keV of EW at the rest frame.

#### 4.3.4 Discussion for NGC1808 and NGC1667: disappearance of cutoffs

**NGC 1808** We have detected clear emission from He-like Mg and Si. We further obtained a better constraint on the plasma temperature of  $kT = 0.62 \pm 0.03$ . The unabsorbed luminosity of the soft component in the 0.5-2.4 keV band was about  $6 \times 40 \text{ergs}^{-1}$ , which is about 1/2 of the ROSAT result. This discrepancy is caused mainly from the difference of the best-fit temperature because observed luminosities (absorbed) are not largely different.

Since we found the prominent K-shell lines from He-like Mg and Si of roughly solar abundance, we interpret that the origin of the hot gas is interstellar gas, heated by a collisional shock. Most probable energy sources of the shock are supernova explosions associated with the starburst activity near the center of NGC 1808. We constrain that the abundance of heavy elements in the hot gas is larger than 0.7, consistent with the solar values. These "normal abundance" of NGC1808 is rather peculiar for the X-ray emitting starburst galaxies. Although number of sample galaxies is still limited, ASCA results of starburst galaxies show significant lower abundances than solar. For example, the metal abundances in the M82 hot gas are found to be only 0.1 of solar (Tsuru et al. 1994[172]). We suspect that the "normal abundance" of NGC1808 can be explained by the scenario that NGC1808 has almost finished the star burst phase (Forbes et al. 1992[47]), hence has accumulated a large amount of metals. On the other hand, M82 and possibly other ASCA sample galaxies, would be just in the middle of the burst phase.

The hard X-ray spectra are well represented with an absorbed power law of a photon index of 1.3(1.0-1.7). Due to the limited S/N in the hard X-ray band, the absorbing column density is poorly constrained ( $< 4 \times 10^{22} \text{cm}^{-2}$ ). The observed 2-10 keV flux is  $8 \times 10^{-13} \text{ergs}^{-1} \text{cm}^{-2}$ , then the 2-10 keV band luminosity is estimated to be  $10^{40} \text{ergs}^{-1}$ . The origin of the hard X-ray is not SNRs, because no SNR observed with ASCA shows such a temperature of  $> 10 \text{keV}$ , as found in NGC1808. An integrated emission from neutron star binaries is a more likely source. The ASCA hard luminosity of NGC1808 follows the relation between X-ray and blue-band luminosities found in normal galaxies (Trinchieri and Fabbiano 1985[171]; David et al 1992[31]). The high Supernova rate inferred from the soft X-rays may produced many high mass neutron star X-ray binaries (HMXB).

Thus ASCA spectrum, both the soft and hard components, are consistent with being originated from the starburst activity in the vicinity of the center of NGC1808. On the other hand, Ginga found a non-thermal emission of the 2-10 keV luminosity of  $5 \times 10^{40} \text{ergs}^{-1}$  with heavy absorption of  $N_{\text{H}} \sim 10^{23} \text{cm}^{-2}$  (Awaki & Koyama 1993[13]). The ASCA spectrum

gave the similar photon index to the Ginga result. However, the observed flux with ASCA is about 1/3 of the Ginga value. The column density with ASCA is also significantly reduced from the Ginga observation. It is hard to explain the variability in the framework of starburst activities. The straightforward interpretation is that the hard X-rays, if not all, are attributable to a single origin, like an AGN. Flux variabilities of the time scale of a few year are common among AGNs. Time variability of the column density are not so common but do exist in some Seyfert galaxies. In summary, even after the ASCA observations, whether NGC1808 harbors an obscured AGN or not is still unclear.

**NGC 1667** Model fits for the hard X-ray spectrum observed with Ginga give the best fit photon index of  $1.1 \pm 0.5$  and the hydrogen column density of  $22.4 (< 23) \text{H atom cm}^{-2}$  and the 2-10 keV flux of  $3 \times 10^{-12} \text{ergs s}^{-1} \text{cm}^{-2}$ . In the ASCA spectra, such emission does not seen. The ASCA flux of the hard component of  $6 \times 10^{-14} \text{ergs s}^{-1} \text{cm}^{-2}$  is smaller than 1/10 of the Ginga flux. The flux obeys the relation of X-ray and blue-band luminosities seen in normal and starburst galaxies.

The soft component of NGC 1667 has a steep slope of  $\Gamma = 3.76(2.46 - 7.27)$ , which is alternatively reproduced thermal plasma model with the temperature of  $kT=0.80(0.69-0.94)$ . The thermal emission with the sub-keV temperature is also seen in NGC1808. The metal abundance for NGC1667 is  $0.08(0.03-0.20)$ , much smaller than that ( $> 0.7$ ) of NGC1808.

#### 4.4 Seyfert 2 showing a strong Fe K line in the Ginga spectra

##### NGC 1068

###### 4.4.1 NGC 1068

**Introduction to NGC 1068** NGC 1068 is one of the closest and the brightest Seyfert 2 galaxy. It is known to be one of the most luminous nearby galaxies at infrared wavelength, exhibiting strong circumnuclear starburst activities. It is a unique Seyfert 2 galaxy among the samples of the Ginga (Awaki et al. 1990[15]) and IPC (Krupe et al. 1990[88]). The soft X-ray spectrum of NGC 1068 shows no evidence of absorption but shows a rather strong low energy "excess". The BBXRT spectrum of NGC 1068 (Marshall et al. 1993[96]) demonstrates that the soft emission from NGC 1068 has strong Fe L emission line features. NGC 1068, like many other Seyfert 2 galaxies, has been found to exhibit a very strong Fe

K line ( Koyama et al. 1989, Awaki 1992[9]). The BBXRT data indicate that the K shell transition lines of NGC 1068 are complex including a strong 6.4 keV fluorescent line.

The ROSAT HRI image shows that about half of the X-ray emission at  $E = 0.8$  keV comes from an unresolved point-like source and the other half is extended (Wilson et al. 1992[205]). The size and position angle of the extended emission are consistent with the region of starburst activity associated with radio sources and optical emission lines. The soft X-ray flux of the extended emission is consistent with that of the predicted luminosity using the relation of X-ray and infrared flux found in the starburst galaxies (David et al. 1992[31]). Thus NGC 1068 is likely to exhibit a significant starburst contribution in the soft X-ray spectrum. However no convincing X-ray spectral evidence for the starburst activities has been seen.

Optical polarimetry and spectroscopy (Antonucci, Miller 1985[3]) indicate that the central emission region is obscured from our direct line of sight and that it is seen only in light which is scattered by relatively cool electrons. The existence of broad lines in the polarized flux of NGC 1068 has prompted the development of the "unified model" of active galaxies (Antonucci 1993[2]) in which Seyfert 1s and Seyfert 2s are fundamentally the same objects but seen from different directions. Detailed modeling of NGC 1068 in the framework of the unified model done by Miller, Goodrich, and Mathews (1991[108]) and Marshall et al.(1993[96]) can account for most of its optical, UV, and X-ray properties.

Marshall et al.(1993[96]) present a detailed photo-ionization model of NGC 1068 which is capable of accounting for the lack of either emission or absorption features due to oxygen, and predict the presence of a wide range of ionization states which contribute to the observed Fe K lines. However the model requires a very unusual ionizing spectrum and unusual chemical abundances. Recent analysis of optical, IR, UV, and X-ray data (Pier et al. 1994 private communication) indicates that the "true" ionizing spectrum may be rather different from that inferred by Marshall et al(1993[96]).

Higher signal to noise and better energy resolution measurements with the ASCA SIS and GIS detectors, combined with the longer exposure times, would allow a reconciliation between the X-ray spectra and the evidence for spatial extent in the X-ray gas and the infra-red evidence for strong starburst activities.

**ASCA observation of NGC 1068** ASCA obtained a  $\sim 39$  ksec observation of NGC 1068 on 1993 July 24. In the GIS and SIS image NGC 1068 is the only bright target and we

have extracted spectra from a region of 10' diameter to obtain  $\sim 95\%$  of the total photons in the image.

**High Energy Continuum with Fe K Lines of NGC 1068** The SIS spectrum is shown in figure 15. The low energy region ( below about 3 keV) is very complex, while the high energy part is more simple. We therefore try to make a model spectrum in the high energy part and then extrapolate it to the low energy region. We firstly examined a power-law model with Gaussian lines at around 6–7 keV. Since the photon index of the high energy continuum depends on the shape of low energy components, we have limited the fitting region above 3 keV, excluding the iron line energy region of 6–7 keV. The best-fit photon index is found to be  $1.27 \pm 0.3$ . There is no evidence for absorption with a 90 % confidence upper limit of  $5 \times 10^{22}$  atoms  $\text{cm}^{-2}$ . By adding a Gaussian line around 6–7 keV, we found the strong line at  $6.39 \pm 0.02$  keV with  $\sigma < 0.1$  keV (corresponding to  $\sigma_v < 4700$  km/sec for the Doppler broadening). However there are still residuals that are best fitted by an additional broad line at  $6.69 \pm 0.11$  keV with  $\sigma = 0.3 \pm 0.1$  keV and a hint of a narrow line feature at 8.36 keV with a flux of  $5.4 \times 10^{-5}$  cts  $\text{cm}^{-2}\text{s}^{-1}$ . The spectra also do not require a strong 7.1 keV absorption feature, such as is predicted by reflection models, with an upper limit of  $\tau < 0.4$ . The best-fit SIS spectrum in the high energy band is given in figure 13. A thin thermal model with  $kT \sim 30$  keV can fit the continuum shape as well as a power-law model. However, the iron K complex, in particular the “6.4 keV line”, can not be explained and also needs an additional model for the line complex.

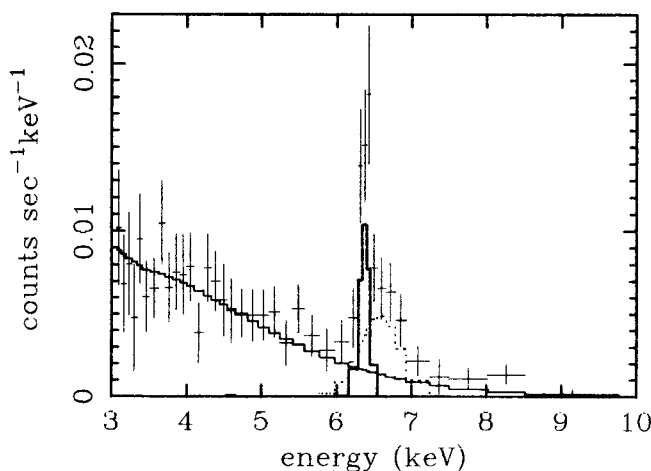


Figure 13: High energy spectrum including Fe K line complex(only SIS 0 data is shown)

The best-fit 3 components is shown; a narrow Gaussian component(solid), a broad Gaussian component(dotted), and a power-law component. The model was fitted with SIS0 and GIS2 data simultaneously in the 3–10 keV band.

The ASCA data confirm the BBXRT detection of at least 2 Fe K lines. The 8.36 keV

line is also seen in the BBXRT data at a similar flux. The equivalent widths are  $1.1 \pm 0.4$  and  $2.6 \pm 0.6$  keV for the 6.39 and 6.69 keV lines. The complex around 6–7 keV is also fitted with 3 narrow Fe K lines at  $6.38 \pm 0.01$ ,  $6.60 \pm 0.03$ , and  $6.85 \pm 0.02$  consistent with the expected energies of neutral, He and H-like Fe. The EWs are  $1.6 \pm 0.4$ ,  $1.0_{-0.5}^{+0.4}$  and  $0.6_{-0.3}^{+0.4}$  respectively. The flux-weighted center energy of the Fe K complex is consistent with the Ginga results (Koyama et al. 1989) of a "6.55" keV line. The EWs are consistent with the BBXRT results, but are larger than the Ginga results (however, see Marshall et. 1993). We note that the exact nature of the Fe line complex depends in detail on the continuum model used and further analysis is necessary.

**Low Energy Lines of NGC 1068** The SIS spectrum in the low energy band below 3 keV is given in figure 14 together with the extrapolated power-law model of photon index of 1.27 (see subsection 3.1). We find a clear soft excess above the power-law component.

We have modeled the low energy continuum with a bremsstrahlung plus power-law model (photon index of 1.27). While this model does not have an obvious physical meaning, it is capable of adequately describing the continuum in both the SIS and the GIS and thus allows a basis from which to measure the strengths and energies of the lines. As is obvious in figure 14, many line structures are found in the residuals of the model fitting.

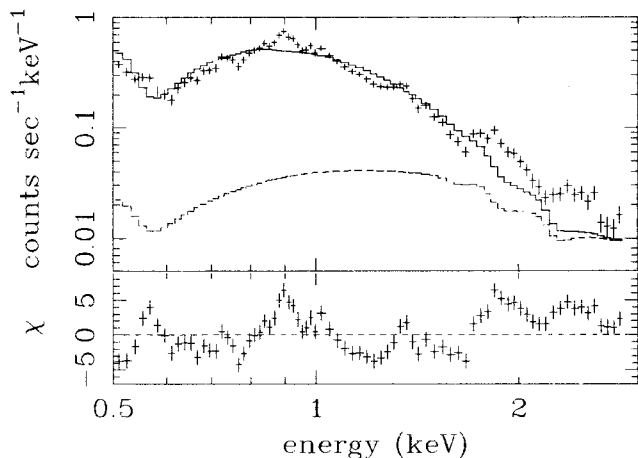


Figure 14: Low energy spectrum of NGC 1068 (only SIS 0 data is shown)

A broken line shows the extrapolated power-law component ( $\alpha_{\text{ph}} = 1.27$ ; see the text) with no absorption, determined at  $E > 3$  keV. A solid line shows a best-fit model consisting of the fixed power-law and a bremsstrahlung components. The residuals are shown in the bottom panel. The model was fitted with SIS 0 and SIS 1 data simultaneously.

Then we have added narrow Gaussian lines one by one until no significant improvement

of  $\chi^2$  value was obtained. The best-fit line parameters are given in table 10 together with candidate atomic lines (energies in parentheses). The "broad bump" at about 0.9 keV seen in the BBXRT spectrum is now resolved into multiple components. The lines with the best-fit energies at 0.74, 0.83, 0.91, and 1.01 and 1.05 keV can be assigned to various transitions in Fe L or Ne K (in particular Fe XVII at 0.73 and 0.83 keV, Fe XXI at 1.01 keV, Fe XXII at 1.04 keV, Fe XXIII 1.12 keV, Ne IX at 0.92 keV and Ne X at 1.02 keV, the 0.83 keV line may alternately be assigned to the Lyman continuum of O VIII due to photoionized gas). The ASCA energy resolution and signal to noise are not adequate to attempt an accurate spectral decomposition in the Fe L line range and some of these energies may not be precise. The line at 0.56 keV is most likely O VII, however its strength depends very strongly on the detailed calibration. The equivalent width of the 0.67 keV feature, attributed to O VIII(0.65keV), is found to be  $28_{-9}^{+10}$  eV, consistent with the BBXRT upper limit and confirms the relative absence of O emission. The lines at 1.33, 1.45, 1.83, 1.97, and 2.4 keV were not detected by BBXRT, presumably due to its poorer signal to noise and are most likely due to He-like Mg, Si, and S and H-like Mg and Si. The observed offsets of  $< 30$  eV from the atomic data are within statistical errors on the line centroids and the present uncertainty in the instrument calibration.

Table 10: Significant low energy lines in NGC1068

Best fit energy* (keV)	Best fit flux† ( $10^{-4}$ ph cm $^{-2}$ sec $^{-1}$ )	ID
0.56	$6.6^{+2.6}_{-1.4}$	O VII(0.57)
0.67	$2.4^{+0.8}_{-0.7}$	O VIII(0.65)
0.74	$2.8^{+0.6}_{-0.6}$	Fe XVII(0.73)/O VII(0.71)
0.83	$3.4^{+0.8}_{-0.4}$	Fe XVII(0.83) or O VIII Lyman continuum
0.91	$4.2^{+0.4}_{-0.3}$	Ne IX (0.92)
1.01	$1.4^{+0.3}_{-0.2}$	Fe XXI(1.01),Ne X(1.02)
1.05	$3.7^{+0.5}_{-0.5}$	Fe XXII-XXIII
1.33	$0.76^{+.11}_{-.11}$	Mg XI(1.34)
1.45	$0.19^{+.08}_{-.09}$	Mg XII(1.47)
1.83	$0.41^{+.06}_{-.07}$	Si XIII(1.87)
1.97	$0.31^{+.07}_{-.06}$	Si XIV(2.01)
2.40	$0.33^{+.06}_{-.05}$	S XV (2.46)

Note.— These were obtained by the simultaneous spectral fitting of SIS0 and SIS1 data with Gaussian lines, a bremsstrahlung and the power law determined at  $E > 3$ keV.

\* No redshift correction is applied for  $z=0.0037$ . Errors for some lines are not estimated due to coupling between adjacent line parameters. Therefore the best fit values are only listed. However nominal statistical errors are about 0.03 keV.

† 90% errors obtained with every center energy of line fixed at the best fit value.

The presence of a large number of emission lines from highly ionized ions prompts an analysis of the low energy band using thin thermal models. A good description of the data is not obtained with a simple 1 temperature coronal plasma model, either Mewe and Kaastra (MEKA, Mewe et al. 1985) or Raymond and Smith (1977). A much better description can be obtained if we include the power law component determined at the high energy band. However there are strong residuals, especially at the Si and S lines, which suggest that a non-solar elemental distribution would improve the fit for this model. We then fitted a variable abundance Raymond Smith model with a power law continuum of photon index fixed at 1.27. This model gives the reduced  $\chi^2$  values of 3.2 ( with 204 d.o.f.) with the best-fit temperature of  $0.41 \pm 0.01$  keV with non-solar abundance. In this model there is still excess emission at  $E < 0.7$  keV. Therefore we can conclude that at least 2 temperatures

are required for the low energy portion of the spectrum.

**Total Spectrum of NGC 1068** We finally have tried simultaneous fits of SIS and GIS data in the wide energy band of 0.5–10 keV using a 2-temperature MEKA model with a power-law component plus iron line complex at around 6–7 keV. We find that the total spectrum can be well fit by this model with the reduce  $\chi^2$  value of 1.38 (350 d.o.f.). The results are given in figure 15, where each component is also given separately. The best-fit power-law index was found to be  $1.28 \pm 0.14$ , which is very close to that determined with the limited energy band above 3 keV. The best-fit parameters of iron K-shell complex are essentially unchanged from that determined in subsection 3.1. The best-fit temperatures of the two thin thermal components are  $kT = \sim 0.59 \pm 0.1$  and  $0.14 \pm 0.1$  keV with the abundances of  $0.30 \pm 0.06$  and  $0.03 \pm 0.01$  of solar, respectively. The flux ratios in the 0.3–3.5 keV band are 38, 50 and 12% for the high- $kT$ , low- $kT$  and power-law components.

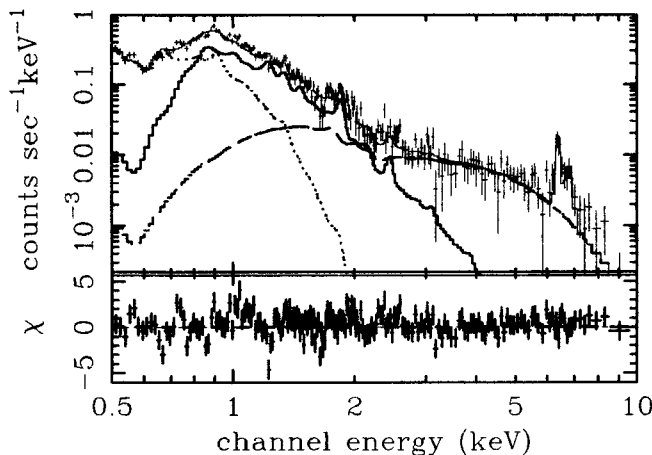


Figure 15: The ASCA SIS spectrum of NGC1068

The ASCA SIS spectrum with a best-fit model (thin line) consisting of two single-temperature MEKA, a power-law and two Gaussian components. Three thick lines show 3 components of the model; a low- $kT$  MEKA (dotted), a high- $kT$  MEKA (solid), and a power law (dashed). Two Gaussian for Fe K lines are not shown. The model was fitted with SIS 0 and GIS 2 data simultaneously, but only SIS 0 spectrum is shown.

Neither the BBXRT nor the Ginga spectra had sufficient signal to noise or energy resolution to determine the shape of the high energy continuum. Koyama et al. (1989) report that the continuum is consistent with a  $\Gamma = 1.5$  power law with no absorption. However the inclusion of a soft power law of index 3 (Monier, Halpern 1987) gives the best-fit Ginga slope to be 1.3 (Koyama et al. 1989). A re-analysis of the Ginga data by Smith, Done and Pounds (1993) finds slopes between 1.33–1.96. Therefore the photon index

derived here is generally consistent with the Ginga results and is significantly flatter than that seen from most the other AGN.

#### 4.4.2 Discussion for NGC 1068

The values of the fluxes for the 3 component models of the low energy data are close to the flux ratio from the spatially resolved components of the ROSAT results (Wilson et al. 1992[205]). We thus propose that some of the unusual features of the model proposed by Marshall et al(1993[96]) would be alleviated if one took into account the dilution of the signal of the photoionized reflector by the, presumably, thermal emission components in the source.

All the 3 component fits require one component to be very soft,  $kT < 0.2$  keV, whose abundance is poorly constrained and one component of  $kT \sim 0.4-0.7$  keV with non-solar abundance ratios. This probably represents non-equilibrium effects( mimicked by multi-temperature ) and/or non-standard abundances. For example, the relative weakness of the Fe XVII L shell to Ne K lines is reproduced by two alternative models. One is a multitemperature model, in which a low- $kT$  component is responsible for the weakness of Fe L shell to Ne K lines and is advantageous to a reconciliation with the ROSAT image. Another is a single-temperature variable-abundance model, in which a low abundance of Fe in hot gas is responsible. In this case a featureless continuum with a steep slope or a low temperature also required.

The question arises as to the origin of the very strong Fe 6.4 keV line which is not seen in the ASCA spectra of starburst galaxies. This line is not explained by thermal components and is a signature of the Seyfert II phenomenon as seen in ASCA spectra of other Seyfert IIs (Mkn 3, NGC 4388, and NGC 6552). We propose that it originates in the scattering medium as originally suggested by Krolik and Kallman (1987[87]). This model has been recently strongly confirmed by Ginga and ASCA observations of X-ray binaries in eclipse, where the X-rays are seen by scattering, bears a strong resemblance to that of NGC1068 in its flat shape and the 6.4 keV line emission.

We propose a reconciliation of the X-ray imaging data from ROSAT and the BBXRT spectra. In the ASCA data a multi-component fit with at least 2 thermal components and a power law is consistent with all the data except for the strong Fe K line. We detect for the first time line emission from He-like and/or H-like Ne, Mg, Si, and S. The high energy continuum is very flat. The origin of the strong spectral difference between NGC

1068 and the other Seyfert IIs observed by ASCA is assigned to the presence of a strong starburst component in NGC 1068 and a very high column density which completely blocks the central source. To derive the physical parameters, detailed modeling of this complex spectrum is necessary. Fluorescence and recombination lines associated with the active galactic nucleus should be taken into account in such modeling.

## 4.5 Seyfert 2s showing optical polarized broad lines

Mkn 463, Mkn 1210, and Mkn 477

### 4.5.1 Mkn 463

**Introduction to Mkn 463** Mkn 463 is a distorted pair of interacting galaxies with a redshift of 0.0506 (Wills et al. 1977[202]), containing two nuclei separated by about 4 arcsec on an east–west line. Hutchings & Neff(1989[65]) find some evidence for young hot stars near the two nuclei.

The western nucleus (Mkn 463W) has a stellar continuum and narrow emission lines with FWHM of about  $500 \text{ km s}^{-1}$  (Wills et al. 1977[202]; Hutchings, Neff 1989[65]; Blanco 1991[20]). Shuder and Osterbrock (1981[160]) classified Mkn 463W as a Seyfert 2 by using the line flux ratio of  $[\text{OIII}]\lambda 5007\text{\AA}/\text{H}\beta$ . However, Wills et al. (1977[202]) and Hutchings and Neff (1989[65]) pointed out that the observed  $[\text{OIII}]/\text{H}\beta$  ratio is outside the typical range for Seyferts.

The eastern nucleus (Mkn 463E) shows a Type 2 Seyfert spectrum with emission line profiles having extended blue wings (Wills et al. 1977[202]; Shuder, Osterbrock 1981[160]; Hutchings, Neff 1989[65]). Some well known indicators which support the presence of an obscured Seyfert 1 nucleus, as predicted by the unified model of Seyfert galaxies, have been found in Mkn 463E. Miller and Goodrich (1990[107]) and Tran (1995[169]) have detected broad Balmer lines in the polarized visible spectrum of Mkn 463E, and conclude that the light from a hidden Seyfert 1 is being scattered by electrons and/or dust into our line of sight. Mkn 463 also exhibits diffuse  $[\text{OIII}]\lambda 5007\text{\AA}$  emission extending about 20 arcsec north and south of the nuclei, roughly perpendicular to the position angle of the polarization of broad Balmer lines (Hutchings, Neff 1989[65]). The  $[\text{OIII}]$  emission is considered to be related to radio activity in Mkn 463E (Hutchings, Neff 1989[65]; Uomoto et al. 1993[183]). Hubble space telescope (HST) images of Mkn463E revealed an optical jet nearly perpendicular to

the optical position angle suggesting that the jet is the scattering mirror. Blanco (1991[20]) found Seyfert 1-like features in the near-infrared band of Mkn 463E spectrum. Although Ginga observations of Mkn 463 gave only an upper limit of  $L(2-10\text{keV}) < 4 \times 10^{43} \text{erg s}^{-1}$  (Awaki 1991[7]), Mkn 463 has been detected at lower X-ray energies by the Einstein and ROSAT satellites; the Einstein observation of Mkn 463 gave a soft X-ray flux (0.2-4 keV) of  $2 \times 10^{-13} \text{erg cm}^{-2} \text{s}^{-1}$  (Kruiper et al. 1990). The ROSAT flux (0.2-4 keV) is also  $2 \times 10^{-13} \text{erg cm}^{-2} \text{s}^{-1}$  (Blanco et al., in preparation).

From the far-infrared luminosity measured by IRAS, Mkn 463 was included in a sample of warm ( $f_{25\mu\text{m}}/f_{60\mu\text{m}} > 0.2$ ) ultraluminous ( $L(\text{bol}) \geq 10^{12} L_{\odot}$ ) galaxies by Sanders et al. (1988[153]). These authors proposed that Mkn 463 is in the transition stage between cool ultraluminous IRAS galaxies and optical quasars. To date, only a few ultraluminous IRAS galaxies have been detected in the X-rays. We therefore observed Mkn 463 with ASCA to compare the X-ray spectrum of this interacting galaxy with normal Seyfert galaxies and investigate the spectral evolution hypothesis.

**ASCA observations of Mkn 463** ASCA observations of Mkn 463 were performed on 1994 January 31. The effective exposure time was about 36 ks.

Mkn 463 is the brightest source in the GIS and SIS fields of view. The broad-band GIS image (with a field of view of about 25 arcmin in radius) contains four obvious sources in addition to Mkn 463 (table 11). However in the (hard) 4-10 keV band image, only Mkn 463 is visible.

We extracted X-ray spectra for each detector from a circular region centered on Mkn 463. The extraction radii were 3 arcmin for GIS2 and GIS3, 3.4 arcmin for SIS0, and 2.7 arcmin for SIS1 (the radii for two SISs were limited by the gaps between the mosaicked CCD chips). We also extracted background spectra from off-source regions in the same field of view. From these we produced combined SIS (SIS0+SIS1) and GIS (GIS2+GIS3) spectra. Both of these combined spectra were then binned so that each energy bin contained at least 40 counts before background subtraction. For the spectral analysis presented below, we fitted these two combined spectra simultaneously.

**X-ray spectra of Mkn 463** We attempted to fit the data with a single-component models modified by absorption in cold gas of solar abundances (Morrison, McCammon 1983): a power-law (formula 1), and a single-temperature Raymond-Smith (RS) plasma

Table 11: Sources in the GIS image selected by using a sliding-cell method (Mkn 463)

Source	GIS 0.5-2keV	GIS 4-10keV	GIS 0.5-2keV	GIS 4-10keV	ID
	(RA, DEC) <sub>epock2000</sub>	(RA, DEC) <sub>epock2000</sub>	$10^{-3}\text{cnt/sec/GIS2+3}^\dagger$	$10^{-3}\text{cnts/sec/GIS2+3}^\dagger$	
A	209.034, 18.378 <sup>†</sup>	209.022, 18.364 <sup>†</sup>	$7.5 \pm 0.9$	$10.3 \pm 1.0$	Mkn463
B	209.256, 18.592	—	$9.5 \pm 1.4$	$< 5.5^\S$	
C	208.890, 18.267	—	$9.2 \pm 1.8$	$< 6.0^\S$	
D	209.136, 18.203	—	$4.8 \pm 1.4$	$< 5.6^\S$	
E	209.138, 18.366	—	$3.0 \pm 0.7$	$< 2.2^\S$	

Notes. — The criteria for the source detection are 1) the probability that the excess in each cell is due to a background fluctuation is less than  $10^{-4}$ , and 2) the signal-to-noise ratio is larger than 3. Source A, B, and C have X-ray peaks in the Einstein IPC image obtained in 1979 January 24 (Harris et al. 1990[59]). Source A, B, and D have peaks in the ROSAT PSPC image obtained in 1992 Jan 15.

† Difference in position between two energy bands is within the uncertainty for GIS.

‡ Observed counts are corrected for vignetting effects and for the fraction of the source counts that fall outside the box where the net counts are estimated.

§  $3\sigma$  upper limits evaluated at the soft-band positions.

with variable abundances (Raymond & Smith 1977[139]). Both of these single-component models were rejected with reduced  $\chi^2 > 2.8$  for 41 of degree of freedom (dof). The best fit photon index was  $0.9 \pm 0.1$  for the power law model, and the best-fit RS temperature is  $> 60$  keV (hereafter errors are given at 90% confidence level). Finding no evidence from these fits for local absorption to the Galactic value corresponding to  $N_{\text{H}}$  of  $2.09 \times 10^{20} \text{ cm}^{-2}$  (Kruiper et al. 1990[88]). In figure 16, the best-fit function of a single power law model and residuals from the data are shown. In the residuals, we find broad features at both the low- and high-energy ends; hence we examined two-component models.

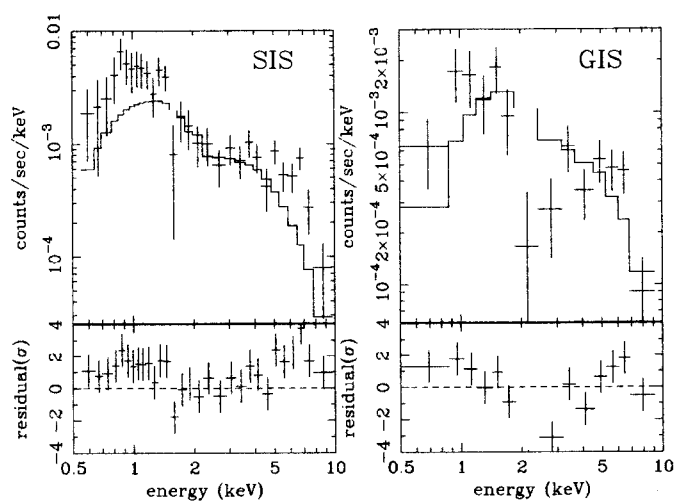


Figure 16: X-ray spectra of Mkn 463 and Single power-law model

Left panel: The SIS spectrum (SIS0+SIS1), Right panel: The GIS spectrum (GIS2+GIS3). Solid lines show a single power-law model, and the residuals are shown in lower panels.

Table 12: Spectral fitting results with double-component models (Mkn463)

Model	Component 1		Component 2		$\chi^2/\text{dof}$
	Parameter	Value	Parameter	Value	
Double Power-Law model..	$\Gamma_{\text{ph}}$	$3.2 \pm 0.5$	$\Gamma_{\text{ph}}$	$-0.3 \pm 0.4$	68/40
	$N_H(10^{20} \text{cm}^{-2})$	2.09*	$N_H(10^{20} \text{cm}^{-2})$	2.09*	
Reflected model.....	$\Gamma_{\text{ph}}$	$3.0 \pm 0.4$	$\Gamma_{\text{ph}}^\dagger$	$1.8 \pm 0.4$	60/40
	$N_H(10^{20} \text{cm}^{-2})$	2.09*	$N_H(10^{20} \text{cm}^{-2})$	2.09*	
	flux(0.5-2keV) $^\S$	$1.2 \times 10^{-13}$	flux(0.5-2keV)	$7 \times 10^{-15}$	
	flux(2-10keV) $^\S$	$3 \times 10^{-14}$	flux(2-10keV)	$4.9 \times 10^{-13}$	
			EW $^\dagger$ (eV)	< 580	
Heavily absorbed model....	$\Gamma_{\text{ph}}$	$2.7 \pm 0.3$	$\Gamma_{\text{ph}}$	$1.4 \pm 0.9$	59/39
	$N_H(10^{20} \text{cm}^{-2})$	2.09*	$N_H(10^{23} \text{cm}^{-2})$	$1.6 \pm 0.8$	
	flux(0.5-2keV) $^\S$	$1.2 \times 10^{-13}$	flux(0.5-2keV)	$5 \times 10^{-17}$	
	flux(2-10keV) $^\S$	$5 \times 10^{-14}$	flux(2-10keV)	$4.3 \times 10^{-13}$	
			EW $^\dagger$ (eV)	< 670	

\* Fixed at the Galactic absorption.

† 90% upper limit of the equivalent width of 6.1keV line(6.4 keV in the rest frame).

‡ Photon index before reflection.

§ In units of  $\text{erg cm}^{-2} \text{s}^{-1}$ .

We therefore fitted the spectra with two power-law components plus the Galactic absorption (Double power-law model in table 12). This model is only marginally consistent with the data; the best-fit reduced  $\chi^2 = 1.7$  for 40 dof. The soft band ( $<3$  keV) of the spectrum is best fitted by a power law of the photon index of  $3.2 \pm 0.5$ , and the hard band by a photon index of  $-0.3 \pm 0.4$ . The soft band was equally fitted with thermal models; replacing the soft-band power law with an RS model, for example, gave a best-fit  $kT = 0.56 \pm 0.14$  keV with abundance  $< 0.3$  solar, while the hard-band power law index remained essentially unchanged. Thus regardless of the origin of the soft component, an extremely flat, hard continuum was required. The unusual flatness of this hard component, together with the marginal value of reduced  $\chi^2$ , led us to examine other possibilities for the hard X-ray component, such as a heavily absorbed power law model and a reflection model (Lightman and White 1988[92]). In these models, the apparent slope in the hard X-ray band may be flattened due to photo-absorption in cold material.

First we tried to fit the hard portion with the reflection model (Reflected model in table 12). As described in Lightman and White (1988[92]), a photons hitting cold matter are reprocessed by photoelectric absorption and Compton down-scattering, into reflected emission with a flatter spectral shape than the incident spectrum. For realistic geometries, the direct power-law and the reflection components should be mixed together. However, we examined first the extreme case of a pure reflected component. The other extreme, which we examine later, is the heavy-absorbed power-law model, where only the direct component is included. We have fixed the solid angle sustained by the reflecting disk to  $2\pi$  steradian, and the inclination angle of the disk to zero. Additional Galactic absorption was applied to these model spectra. The reflection model gave the photon index of incident spectrum of  $1.8 \pm 0.4$  with the best-fit reduced  $\chi^2$  of 1.5 for 40 dof. In this case, the best-fit photon index for the soft component was derived to be  $3.0 \pm 0.4$ . Next, we tried the heavily absorbed power law model (Heavily absorbed model in table 12), adding a new parameter  $N_H$  for the absorption of the hard component. The best-fit  $N_H$  and photon index were found to be  $(1.6 \pm 0.8) \times 10^{23} \text{ cm}^{-2}$  and  $1.4 \pm 0.9$  respectively, with a reduced  $\chi^2$  of 1.5 for 39 dof. Since the fitted  $N_H$  and photon index are coupled to each other, we show confidence contours of these two parameters in figure 17. Fixing the photon index to be 1.7 (a typical value for Seyfert galaxies), the corresponding best-fit  $N_H$  is  $(1.8 \pm 0.4) \times 10^{23} \text{ cm}^{-2}$ , with a reduced  $\chi^2$  of 1.5 for 40 dof. The best-fit parameters of the soft component did not change within the errors. The resulting spectral model is shown in figure 18.

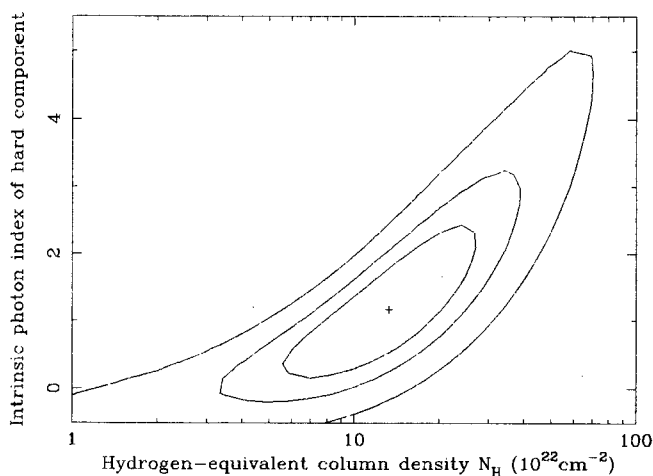


Figure 17: Confidence contours of  $N_H$  versus  $\Gamma(\text{hard})$  for Mkn463

Confidence contours of the column density versus the intrinsic photon index for the hard component at the confidence levels of 68, 90, 99 %.

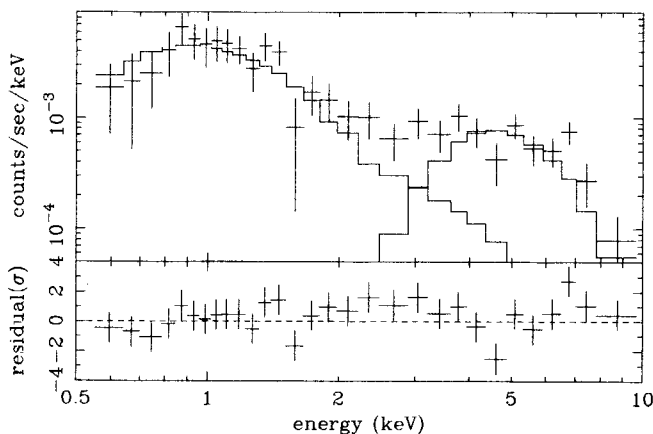


Figure 18: X-ray spectrum of Mkn 463 and double power-law model

The model was fitted with the SIS and GIS data simultaneously. Only the SIS data are shown. The solid lines are the best-fit model functions. The photon index of the hard component is fixed at the value of 1.7.

Our ASCA observations place limits on the presence of the 6.4 keV Fe K emission line, which has been observed in many AGN. At the redshifted energy of 6.1 keV we found upper limits to the equivalent width of 580 eV for the reflected model and 670 eV for the absorbed power-law model at the 90% confidence level.

We also searched for evidence for X-ray variability in the SIS0, the SIS1, the GIS2, and the GIS3 data. We constructed X-ray light curves for the 0.5–4 keV and the 4–10 keV bands with a bin size of 256 s and applied the  $\chi^2$  test to the hypothesis of constant fluxes. The reduced  $\chi^2$  values were found to be equal to or less than about one (each for about 100 dof) for the soft and hard bands of all detectors. Thus no significant time variability was found over time scales of  $10^3$  s to 10 hr.

#### 4.5.2 Discussion for Mkn 463

**Soft Component** The soft component can be reproduced by either power-law or by thermal models showing no significant line features. While a more detailed analysis of this component will be made in a future paper incorporating ROSAT data, we note here that (i) the ROSAT source is coincident with Mkn 463E, and (ii) we see no evidence of variability around 1 keV between the observations by Einstein (1979 Jan 24: Kruper et al. 1990[88]), ROSAT (1992 Jan 15) and the ASCA observations presented here.

Given the correspondence with Mkn 463(E) and the existence of scattered broad line emission (Miller, Goodrich 1990[107]), we examined the possibility that the X-ray soft component is also scattered light from Mkn 463E. The luminosity can be explained by the scattering of about 5% of the hard component, with the assumption that the intrinsic photon index of the hard component extends to 0.5 keV. Constraining the hard- and soft-component slopes to be equal gave a best fit  $N_{\text{H}}$  of  $(2.7 \pm 0.5) \times 10^{23}$  H atom  $\text{cm}^{-2}$  for the hard component, and a photon index of  $2.6 \pm 0.2$  with a reduced  $\chi^2$  of 1.6 for 39 dof. Since the fit is poor and the best-fit spectral slope is rather steep for Seyfert galaxies, we prefer the alternative possibility that the X-ray soft component has a separate, probably thermal origin.

**Hard Component** The two nuclei (Mkn 463E and Mkn 463W) cannot be resolved in the ASCA images; their 4-arcsec separation is smaller than the ASCA's spatial resolution and the accuracy of positional determination of  $\sim 1$  arcmin. However, the ionizing luminosities of the 2 nuclei are vastly different as judged from their optical spectra. On the basis of [OIII]  $\lambda 5007\text{\AA}$  line strengths, for instance, Mkn 463E is brighter by a factor of about 20 (Tull et al. 1979[173]; Uomoto et al. 1993[183]). Thus we identify Mkn 463E as the origin of the hard X-ray flux.

Modeling the hard component with a simple power law, we found that this component has an extremely flat slope with a photon index of about  $-0.3$ . Since the flat slope cannot be explained by the intrinsic spectrum of any known X-ray sources, we suspect that this hard component is due to photoelectric absorption of an intrinsically steeper spectrum. From the reduced  $\chi^2$  values of our continuum fits we cannot judge whether the reflection model or absorbed model is more realistic for the origin of the hard component. Nevertheless, we can estimate the contribution of the reflection model using the equivalent width of the iron line, since an X-ray spectrum reflected or scattered by cold material is expected to produce

a high equivalent width ( $\sim 2$  keV) fluorescent iron K-line, as seen in NGC1068 (Koyama et al. 1989[83]; Marshall et al. 1993[96]; Ueno et al. 1994[180]). On the other hand, a direct X-ray spectrum transmitted through a column  $N_{\text{H}}$  of  $1.6 \times 10^{23}$  H atom  $\text{cm}^{-2}$  would produce an equivalent width of about 200 eV (Inoue 1985[66]). Thus if we reasonably assume that the iron abundance is comparable to solar in Mkn 463E, the upper limit for the fluorescent Fe K line ( $< 670$  eV) implies that the absorbed power-law contributes at least 70% of the hard component flux.

The fitted X-ray absorption of this hard component corresponds to a dust extinction of  $A_{\text{V}} \simeq 90$  mag for a Galactic dust-to-gas ratio. This is far higher than estimates of the dust extinction, for instance the  $9.7 \mu\text{m}$  silicate feature measured by Roche et al. (1991[146]) implies  $A_{\text{V}} \simeq 7$  mag. The discrepancy is easily explained either by the different extents of the infrared and X-ray emitting regions, or by a large column of dust-free gas along the line-of-sight to the X-ray source.

From the best-fit  $N_{\text{H}}$  for the photon index of 1.7 assumed above, we therefore derive an intrinsic 2–10 keV luminosity  $L_{\text{X}}$  for the hard power law source to be  $1 \times 10^{43}$  ergs  $\text{s}^{-1}$ , very close to the upper limit obtained with the Ginga satellite (Awaki 1991[7]).

Well-established correlations exist for unobscured Seyfert 1 galaxies between their 2–10 keV luminosity and their broad-line, [OIII] and far-infrared luminosities. For Mkn 463E, all these indicators predict a much higher hard X-ray luminosity that we report here. We consider the far-infrared emission of Mkn 463, which is due mostly to Mkn 463E (Roche et al. 1991[146]). Using the correlation presented by Ward et al. (1988[191]) or Mulchaey et al. (1994[111]) between  $L_{\text{X}}$  and infrared luminosity  $L_{\text{IR}}$  for Seyfert 1s, Mkn 463E's far-infrared luminosity of  $3.4 \times 10^{45}$  ergs  $\text{s}^{-1}$  predicts  $L_{\text{X}} \simeq 10^{44}$  ergs  $\text{s}^{-1}$ . Similarly, the [OIII] luminosity of  $4.1 \times 10^{42}$  ergs  $\text{s}^{-1}$  (Shuder, Osterbrock 1981[160]; Mazzarella, Boroson 1993[103]) implies comparable values of  $L_{\text{X}}$  if Mkn 463E is a typical Seyfert 1 (Mulchaey et al. 1994[111]). Finally, broad line emission from Mkn 463E has been detected in the near-infrared by Blanco (1991[20]) and Goodrich et al. (1994[53]); these broad infrared lines may either be transmitted from the BLR, or reflected by a scattering region obscured by  $A_{\text{V}} \simeq 5$  mag. In either case, using Mkn 463E's broad Paschen  $\alpha$  flux of  $1.9 \times 10^{-13}$  ergs  $\text{cm}^{-2}$   $\text{s}^{-1}$  (Blanco 1991[20]), the corresponding  $L(\text{H}\alpha)$  of  $2.1 \times 10^{43}$  ergs  $\text{s}^{-1}$  would imply  $L_{\text{X}} \simeq 1.7 \times 10^{44}$  ergs  $\text{s}^{-1}$  from the correlation between these quantities established for Seyfert 1s (Ward et al. 1988[191]).

It appears therefore, that at least at the current epoch, Mkn 463E is underluminous in X-rays compared to our expectations for typical Seyfert galaxies. If we are seeing only a

fraction of Mkn 463E's true hard X-ray luminosity, the source must be highly anisotropic. Alternatively, by analogy with NGC1068 it may be completely obscured; however for this latter case have already argued against an origin of the observed hard component in an electron-scattered AGN continuum (due to the high  $N_{\text{H}}$  and lack of Fe K emission). While more sensitive observations of Mkn 463, extending to higher energy, are needed to determine  $N_{\text{H}}$  and the intrinsic shape of the hard component independently, the ASCA observations presented here have demonstrated that Mkn 463E does *not* conform to the simplest interpretation of the unified scheme for Seyfert galaxies, despite the persuasive evidence gathered from lower energies. If similar objects to Mkn 463 share its property of X-ray quietness (cf. Rieke 1988[142]), an extension of the unified model of Seyfert galaxies may be required to incorporate such a new class of AGN.

- Summary of Mkn463**
1. The ASCA spectra of Mkn 463 require at least two components: soft and hard. No evidence was found for a strong fluorescent iron K line ( $\text{EW} < 670 \text{ eV}$ ).
  2. The soft component can either be explained by a non-thermal (photon index=2.7) or a thermal continuum ( $kT = 1 \text{ keV}$ ), with no evidence for long-term variability. We suggest that the steep spectral slope makes it unlikely that this soft component is due to electron scattering of an intrinsic AGN continuum.
  3. The hard component has extremely flat slope. This is interpreted to be due to heavy absorption and/or reflection of an intrinsic Seyfert 1 continuum. From the limits on iron equivalent width, we suggest that more than 70% of these X-rays are due to the heavily absorbed transmitted component. For a typical photon index of 1.7, the intrinsic  $N_{\text{H}}$  and luminosity of this continuum are respectively estimated to be  $1.8 \times 10^{23} \text{ H atom cm}^{-2}$  and  $1 \times 10^{43} \text{ ergs s}^{-1}$ .
  4. This inferred intrinsic hard X-ray luminosity is much smaller than that expected by comparison with Seyfert 1s of comparable broad line, [OIII], and far-infrared luminosities. This implies that at least at the current epoch, Mkn 463E is an X-ray quiet AGN. Similar hard X-ray observations of other infrared-luminous Seyfert 2s will be able to establish whether this is a general property of this class of active galaxy.

### 4.5.3 Mkn 1210

**Introduction to Mkn 1210** Mkn 1210 appears to be an isolated compact galaxy, and the wide band spectrum exhibits many features characteristic to Seyfert galaxies (Tran et al. 1992 [170]); they found clear evidence for broad components of  $H\alpha$  and  $H\beta$  emission lines in the polarized flux spectra of this object. No report on the hard X-ray spectrum has been found.

**ASCA observation of Mkn 1210** ASCA observations were performed on 1995 October 18 and November 12. After the data screening, the remaining effective exposure time of the SIS and the GIS were 12.2 ks and 12.4 ks for October 18, and 5.7 ks and 6.0 ks for November 12. We have extracted spectra from a region of 6' and 10' diameters for SIS and GIS, respectively.

**X-ray spectra of Mkn 1210** We found no significant variability during the ASCA observation because of the limited photon numbers. Thus we add all data for the spectral fit. To keep the grade of the data, we made the GIS background spectra from the blank-sky data accumulated by the Goddard Space Flight Center with the long exposure of 324.6 ks. On the other hand, the SIS blank-sky data accumulated in the 4CCD mode has different internal background level from that of our observation mode (1CCD). For the background subtraction of the SIS data of Mkn 1210, we used the near sky spectra in the same exposure that Mkn 1210 was observed in.

The ASCA spectra are shown in figure 55 after the background subtraction. We found a soft and a hard components as seen in other Seyfert galaxies in this paper. We also found a line structure around 6 – 7 keV, which is apparent in the SIS0, SIS1, and GIS3 in common.

We applied a two-component power-law model (formula 2). The best-fit parameters are listed in table 19. The reduced  $\chi^2$  is 0.87 for 92 degrees of freedom (dof). The hard component has the photon index of 0.9(–0.2–1.9) absorbed by the hydrogen-equivalent column density of  $1.2(< 2.3) \times 10^{23} \text{H atom cm}^{-2}$ . The soft component has the photon index of 2.6(>2.2) absorbed by the hydrogen-equivalent column density of  $< 1.3 \times 10^{22} \text{H atom cm}^{-2}$ . The best fit center energy of line is 6.53(6.37–6.62) at the rest frame, and the equivalent width of it is 820(460–1250) eV.

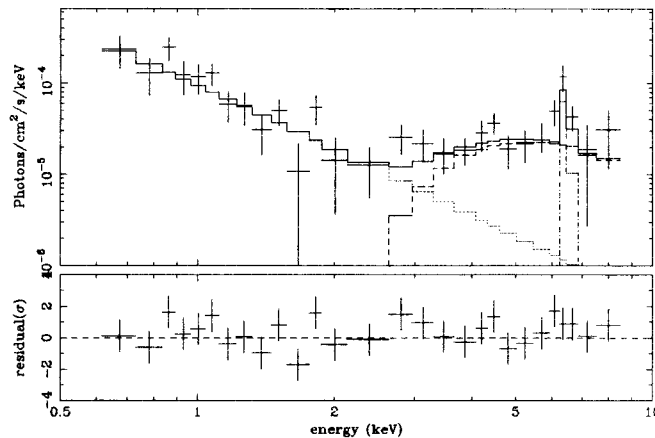


Figure 19: The same as in figure 7, but for Mkn 1210

The photon index is slightly smaller than the typical value ( $\sim 1.7$ ) seen in Seyfert galaxies. We performed another fit where the photon index of the hard component is frozen to 1.7. The best-fit model function is shown with the SIS0 data in figure 19. The best-fit parameters are shown in table 19. The reduced  $\chi^2$  is 0.88 for 93 dof. Then, the best-fit column density for the hard component is limited to be  $2.0(1.4 - 2.8) \times 10^{23} \text{H atom cm}^{-2}$ . The slope of the soft component is also determined to be  $2.4(2.0-3.5)$ . The other parameters do not change within the errors.

#### 4.5.4 Mkn 477

**Introduction to Mkn 477** Tran et al (1992[170]) found clear evidence for polarized broad lines in Mkn 477. However, it is disputable whether the central ionizing source in Mkn477 is obscured from direct view or not (Tran et al 1992; Kinney et al 1991 [77]). The ASCA observation is the crucial test.

**ASCA observation of Mkn 477** The observations were performed on 1995 December 4-5, with the effective exposure time of the SIS and the GIS of 45.1 ks and 44.2 ks, respectively. We have extracted spectra from a region of 6' and 10' diameters for SIS and GIS, respectively.

**X-ray spectra of Mkn 477** We found no significant variability during the ASCA observation. For the background subtractions we followed the procedure described for Mkn 1210.

The spectra of NGC 477 are shown in figure 56 after the background subtraction. We found at least two components for continuum emission, a soft and a hard ones, and a line structure around the energy of Fe K line especially apparent in the GIS2 spectrum.

Thus we applied a model given in formula 2 and listed the best-fit parameters in table 19. The reduced  $\chi^2$  is 0.90 for 129 degrees of freedom (dof). The hard component has the photon index of 0.2(-0.5-1.0) absorbed by the hydrogen-equivalent column density of  $9(< 21) \times 10^{23} \text{H atom cm}^{-2}$ . The soft component has the photon index of 2.0(1.0-8.6) absorbed by the hydrogen-equivalent column density of  $< 9.3 \times 10^{21} \text{H atom cm}^{-2}$ . The best fit center energy of line is 6.40(6.34-6.45) at the rest frame, and the equivalent width is 490(290-740) eV.

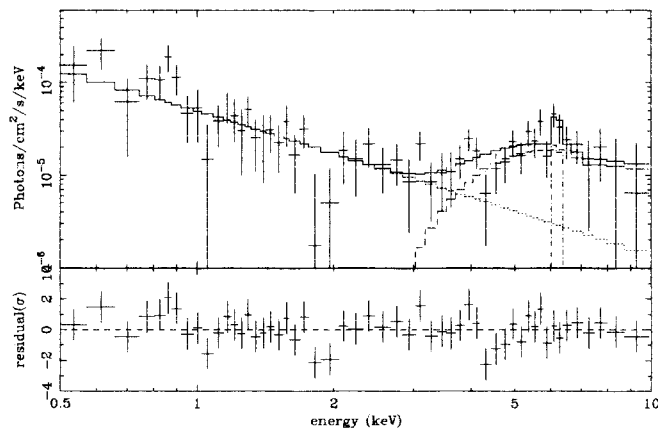


Figure 20: The same as in figure 7, but for Mkn 477

The photon index is much smaller than the typical value ( $\sim 1.7$ ) seen in Seyfert galaxies. By fixing the photon index at 1.7, the absorbing column density for the hard component increased to be  $3.4(2.5 - 4.6) \times 10^{23} \text{H atom cm}^{-2}$ , and the equivalent width of Fe K line slightly reduced to be 370(170-610) eV. The best-fit model function is shown with the unfolded SIS0 data in figure 20. The best-fit parameters are shown in table 19.

#### 4.5.5 Discussion for Mkn 1210 and Mkn 477

Mkn 1210 and Mkn 477 have similar X-ray spectra although the X-ray luminosities of Mkn 477 is seven times larger than that of Mkn 1210. The discovery of the hard components in these sources supports the scenario that type 2 Seyferts showing optical polarized broad line harbor obscured X-ray nuclei as well as masked broad line regions.

We found a strong Fe K line in each sources. Especially Mkn 1210 has the large equivalent width of 830(460-1250) eV. If the cold matter with solar abundance surrounds around isotropic ionizing X-ray sources, an Fe-K equivalent width (EW) of  $\sim 100f(N_{\text{H}}/10^{23}\text{cm}^{-2})$  eV is expected for the hydrogen-equivalent column density of  $N_{\text{H}} < 10^{24}\text{cm}^{-2}$ , where  $f$  is the covering factor (eg. Awaki et al. 1991 [14]). Assuming the absorption of the hard component is due to the cold matter, the expected Fe-K EW for Mkn 1210 is 200(120-280) eV even for the  $f$  of 1. The observed large EW would imply that some amount of direct emission from ionizing X-ray source is perfectly blocked. For an extreme, we applied the reflection model employed for Mkn 463 and get a acceptable fit with the reduced  $\chi^2$  of 0.82 for 92 degree of freedom. The best-fit photon index of the intrinsic ionizing photon is 2.0(1.6-2.8). We estimate the most probable ratio of the heavily absorbed and the reflected continuums to be 6:4 assuming that those continuums are accompanied by Fe K line with EWs of 200 and 2000 eV, respectively; the same assumption that we employed for Mkn 463.

## 4.6 Seyfert 2 showing moderate a low energy cutoff in the Ginga spectra

### NGC 2110

#### 4.6.1 NGC 2110

**Introduction to NGC 2110** This galaxy is classified a narrow emission-line galaxy (NELG). The Narrow Emission Line Galaxies (NELGs) comprise a class of Active Galactic Nuclei (AGN) which were originally recognized to be strong X-ray emitters, and were subsequently found to exhibit narrow emission line ( $< 600 \text{ km s}^{-1}$  FWHM) regions near their galactic centers (e.g., Shuder 1980[159] and references therein). They are now usually classified as Seyfert 2's, although some authors call them 1.9's because of the faint broad-line component of  $\text{H}\alpha$ . Extensive discussions have been made whether or not their optical properties are different from those of Seyfert 2 galaxies (e.g., Rubin 1978[148]; McClintock et al. 1979[105]; Veron et al. 1980[186]). For example, McClintock et al. (1979[105]) concluded that most of the NELGs are not different from Seyfert 2's because they have the line ratio of  $[\text{OIII}]\lambda 5007/\text{H}\beta$  similar to that of Seyfert 2's (the classification scheme adopted by Weedman 1977[197]). On the other hand, Veron et al. (1980[186]) and Shuder (1980[159]) detected a faint broad  $\text{H}\alpha$  component from some NELGs. Thus, Lawrence and

Elvis (1982[90]) suggested that NELGs are classified as AGN in transition from Seyfert 1's to Seyfert 2's.

In order to address the nature of NELGs, we selected NGC 2110 as a typical example. Optical line ratios plotted on the "BPT" diagrams (Baldwin et al. 1981[17]) indicate that the line emission is due to photoionization by non-thermal power-law photons (Wilson et al. 1985[203]). Ulvestad & Wilson (1983[181]) and Pogge (1989[135]) reported on extended and elongated ionized gas in the S0 galaxy NGC 2110. Pogge's(1989[135]) ionization map of  $[OIII]/(H\alpha+[NII])$  shows a conelike structure fanning out from the nucleus on one side, similar to that observed in NGC1068. Spectropolarimetrically, this object had an uncorrected polarization of 0.3 %, low enough to be consistent with an interstellar origin. A marginal broad  $H\alpha$  component with the line width of 2300 - 3600  $\text{km s}^{-1}$  (FWZI) was reported by Shuder (1980[159]).

X-ray emission of NGC 2110 was first detected by Bradt et al. (1978[23]) with the SAS-3 satellite. From the HEAO-1 observations, Mushotzky (1982[113]) suggested that NGC 2110 is a Seyfert 1 in disguise since the hard X-ray luminosity, spectrum and time variability resemble to those of low luminosity Seyfert 1's. Turner and Pounds (1989[177]) reported a soft excess emission below  $\simeq 1$  keV from the EXOSAT observation, which was confirmed and suggested to be spatially extended by Weaver et al. (1995[194]) on the basis of the BBXRT and ROSAT observations. With Ginga, Hayashi et al. (1996[60]) have found the variability of a few hours . This fast time variability is firm evidence that NGC 2110 harbors a compact active galactic nucleus.

**ASCA observation of NGC 2110** NGC 2110 was observed on 1994 March 12; after the standard data selection, the effective exposure time of the SIS and the GIS were about 35.4 ks and 37.1 ks respectively.

**X-ray spectra of NGC 2110** The spectra of NGC 2110 are shown in figure 57. The overall spectra are different from those of IC5063 and NGC 4507. There is no steep fall of flux around 2-3 keV in the spectra. This suggests that the spectral component dominating above 3 keV is less absorbed. We first apply a power-law model (formula 1)

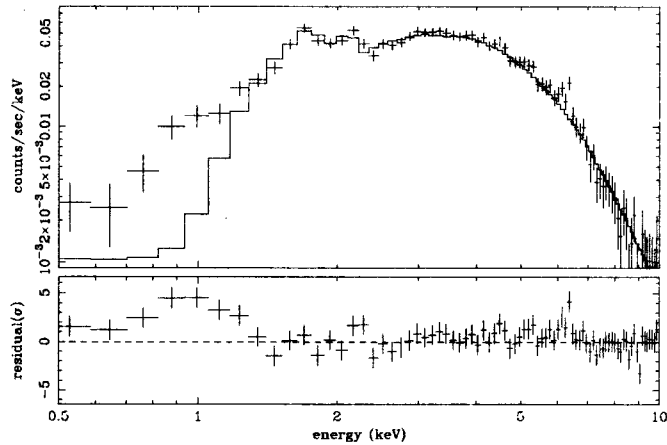


Figure 21: The same as in figure 6, but for NGC 2110

The best-fit model function is shown with the SIS1 data in figure 21. This model was rejected with a reduced  $\chi^2$  of 2.1 for 361 degrees of freedom (dof). The best-fit photon-index and hydrogen-equivalent column density are 1.29(1.25-1.33) and  $2.4(2.3-2.5) \times 10^{22} \text{H atom cm}^{-2}$ , respectively.

The column density is only about one tenth as thick as those of the above objects (IC 5063 and NGC 4507). However, more flux is still seen at soft X-ray energies than expected from a simple extrapolation of the hard X-ray continuum covered by a cold photoelectric absorber, requiring an additional component to be fit. We add another power-law component for the soft excess. The SIS spectra of NGC 2110 show a line feature around 6.0-6.5 keV at the observer frame. We then try two-component model with a Gaussian line (formula 2)

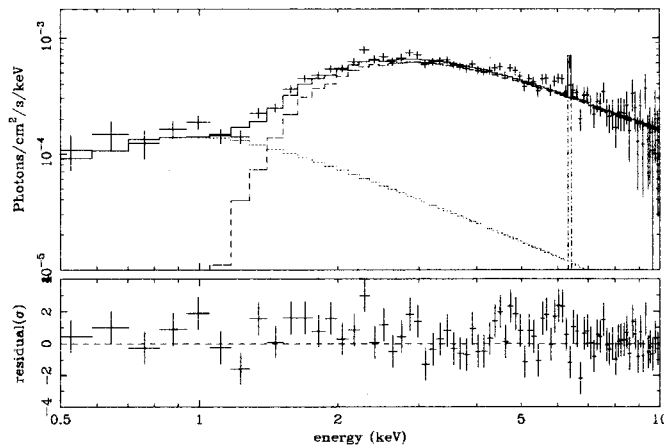


Figure 22: The same as in figure 7, but for NGC 2110

The best-fit model function is shown with SIS0 data in figure 22. The function is unfolded by the response of the instruments, showing the intrinsic spectrum of X-rays incident on the X-ray telescope. The best-fit parameters are listed in table 19. The reduced  $\chi^2$  is 1.36 for 356 degrees of freedom (dof). The hard band ( $> 1.5$  keV) flux is dominated by a power-law component having the photon index of 1.5(1.4-1.6) absorbed by the hydrogen-equivalent column density of  $3.2(2.9 - 3.5) \times 10^{22}$  H atom  $\text{cm}^{-2}$  (hard component). The soft band ( $< 1.5$  keV) flux is dominated by a power-law component having the photon index of 1.7(1.0-5.3) absorbed by the hydrogen-equivalent column density of  $< 6.3 \times 10^{21}$  H atom  $\text{cm}^{-2}$  (soft component). The best fit center energy of line is 6.41(6.38-6.45) at the rest frame, and the equivalent width of it is 151(115-184) eV. The extra soft X-ray emission below  $\simeq 1.2$  keV shows a broad peak around 1 keV, which presumably is a blend of an Fe L-shell complex and Ne K-shell lines.

Firstly, we have considered electron-scattered and reprocessed X-rays from photoionized materials around the nucleus. This idea was applied in terms of the unified scheme, for example, to NGC 1068 (e.g., Marshall et al. 1993). We have simply modeled the scattered component with a power-law continuum, where the photon index was assumed to be the same as that of the primary power-law component in the high energy band. The reprocessed spectrum was calculated using XSTAR (Kallman, Krolik 1993) in the optically thin limit, where the photon index of the input power-law continuum was fixed to be 1.5. The emergent spectrum was given as a function of ionization parameter  $\xi = L/nr^2$ , where  $L$ ,  $n$ , and  $r$  are

the central source luminosity, density of the material, and distance from the central source to the material, respectively. The absorption for these scattered and reprocessed components was assumed to be the Galactic value of  $1.86 \times 10^{21} \text{cm}^{-2}$  (Elvis et al. 1989). The model formula is

$$F(E) = [\{K_{abs}E^{-\Gamma} + \text{Gaussian}\} \exp(-\sigma(E)N_{H_{int}}) + K_{scat}E^{-\Gamma} + S(E, \xi, EM)] \exp(-\sigma(E)N_{H_{Gal}}),$$

where  $K_{abs}$  and  $K_{scat}$  are respectively the normalizations of the absorbed and the scattered power-law components;  $N_{H_{int}}$  and  $N_{H_{Gal}}$  are respectively the intrinsic and the Galactic equivalent hydrogen column densities of cold absorbing materials;  $S(E, \xi, EM)$  is the reprocessed emission as a function of  $E, \xi$  and the emission measure  $EM$ . The best-fit parameters and their 90% confidence ranges are given in table . The intensity ratio of the scattered to the primary power-law component ( $K_{scat}/K_{abs}$ ) was estimated to be  $\simeq 4\%$ .

Table 13: Scattered X-rays model for the ASCA SIS spectra of NGC 2110

	Parameter[Unit]	Best-fit value (90% range)
Absorption	$N_{H_{Gal}}[10^{22}\text{cm}^{-2}]$	0.186(fixed)
	$N_{H_{int}}[10^{22}\text{cm}^{-2}]$	2.89(2.64-3.09)
Power-law	$\Gamma$	1.36(1.28-1.43)
	$K_{abs}[10^{-3}\text{photonss}^{-1}\text{keV}^{-1}\text{cm}^{-2}]$	4.3(3.8-4.8)
Gaussian line	Energy [keV]	6.38(6.35-6.41)
	Width [keV]	0 (fixed)
	Intensity [ $10^{-5}\text{photonss}^{-1}\text{cm}^{-2}$ ]	4.5(3.3-5.7)
Scattered X-rays	$\log\xi$	2.1
	$K_{scat}[10^{-3}\text{photoness}^{-1}\text{cm}^{-2}]$	0.19(0.06-0.22)
2-10 keV flux	Observed [ $10^{-11}\text{ergs}^{-1}\text{cm}^{-2}$ ]	2.6
	Absorption corrected [ $10^{-11}\text{ergs}^{-1}\text{cm}^{-2}$ ]	3.2
reduced $\chi^2$ (dof)		1.0 (393)

Note: Redshift is taken into account for all values except the Galactic absorption.

As the second possibility, we have examined optically thin thermal plasma in ionization equilibrium. The applied model is

$$F(E) = [\{K_{abs}E^{-\Gamma} + \text{Gaussian}\} \exp(-\sigma(E)N_{H_{int}}) + T(E, T_e, Z, EM)] \exp(-\sigma(E)N_{H_{Gal}}),$$

where  $T(E, T_e, Z, EM)$  is the thermal plasma model originally developed by Raymond and Smith (1977), in which  $T_e$ ,  $Z$ , and  $EM$  are the electron temperature, metal abundance, and emission measure, respectively. We have at first fixed the abundance  $Z$  at the solar

value and then allowed it to be free, which procedure was justified with larger than 99.9% significance level by the F-test. This model also well reproduced the SIS spectra with  $\chi^2_\nu$  of 1.0 for 393 d.o.f. The best-fit parameters and their 90% confidence ranges are given in .

Table 14: Thermal plasma emission model for the ASCA SIS spectra of NGC 2110

	Parameter[Unit]	Best-fit value (90% range)
Absorption	$N_{HGal}[10^{22}\text{cm}^{-2}]$	0.186(fixed)
	$N_{Hint}[10^{22}\text{cm}^{-2}]$	2.67(2.48-2.87)
Power-law	$\Gamma$	1.33(1.26-1.40)
	$K_{abs}[10^{-3}\text{photons}\text{s}^{-1}\text{keV}^{-1}\text{cm}^{-2}]$	4.2(3.8-4.7)
Gaussian line	Energy [keV]	6.38(6.35-6.41)
	Width [keV]	0 (fixed)
	Intensity [ $10^{-5}\text{photons}\text{s}^{-1}\text{cm}^{-2}$ ]	4.4(3.2-5.7)
Thermal plasma	$kT_e$ [keV]	1.03(0.88-1.19)
	Z [relative to solar]	0.07(0.02-0.18)
2-10 keV flux	Observed [ $10^{-11}\text{ergs}^{-1}\text{cm}^{-2}$ ]	2.7
	Absorption corrected [ $10^{-11}\text{ergs}^{-1}\text{cm}^{-2}$ ]	3.2
reduced $\chi^2$ (dof)		1.0 (393)

Note: Redshift is taken into account for all values except the Galactic absorption.

We can notice a broad data deficiency around the 7 - 9 keV energy range. We also present data residuals from the narrow line model for the GIS2 and GIS3. Similar data deficiency is seen in the energy range above  $\simeq 7$  keV.

Since this feature is likely due to iron edge absorption, we have added an absorption edge with the edge energy and absorption optical depth as free parameters. Significant improvement was obtained with more than 99 % confidence. The best-fit edge energy and the optical depth were 7.2 keV and 0.2, respectively. The edge energy and optical depth were estimated to be 7.1 - 8.0 keV and 0.05 - 0.4, respectively, in the 90 % confidence level when the width of Fe K line is fix to  $\sigma = 0$ . This edge energy is consistent with "cold" iron inferred by the iron line energy. Then the optical depth of 0.05 - 0.4 gives the equivalent hydrogen column density to be  $\simeq (10 \pm 8) \times 10^{22}\text{cm}^{-2}$  using the cross section of Morrison and McCammon (1983).

#### 4.6.2 Discussion for NGC 2110

The hard X-ray properties of NGC 2110 such as the X-ray luminosity, fast time variability, photon index and iron line equivalent width resemble to those of Seyfert 1's. However, NGC 2110 shows two X-ray properties significantly different from those of typical Seyfert 1's. One is that the reflection component from a cold material is less than 17%, significantly smaller than found in Seyfert 1's with typical value of 100 - 200% (e.g., Piro et al. 1990[134]). The other is the amount of low energy absorption. The hydrogen column density of NGC 2110 is larger than that of Seyfert 1's by roughly one order, while smaller than that of Seyfert 2's by one order (see Awaki et al. 1991[14]).

Optical properties of NGC 2110 rather resemble to Seyfert 2's than Seyfert 1's, with the marginal "broad" H $\alpha$  emission line (Shuder 1980[159]). We have estimated "broad" H $\alpha$  luminosity of NGC 2110 to be about  $10^{42}$  ergs s $^{-1}$ , using the  $L_{H\alpha}$  -  $L_X$  relation (Ward et al. 1988[191]). By absorption due to the moderate  $N_H$ , this flux would become to  $\sim 4 \times 10^{-15}$  ergs s $^{-1}$  cm $^{-2}$ , which value does not conflict with the marginal detection of Shuder (1980[159]). Therefore even the  $N_H$  value obtained from the soft X-ray absorption is sufficient to obscure the Seyfert 1 like BLR, if any. Thus we can conclude that NGC 2110 have essentially the same AGN as Seyfert 1's. Significant difference would be the structure of the circumnuclear gas, which is responsible to the low energy absorption and the reflection component.

We have detected the iron line with equivalent width of 151(115-184) eV from the ASCA observation. We have also found the iron edge structure in the ASCA spectrum with the column density of  $2 - 18 \times 10^{22}$  cm $^{-2}$ . From the line and edge energy, we have given a constraint that the ionization state of iron is less than Fe XVII. Between the Ginga and the ASCA observations, we find no significant variation, or at least no increase, of the equivalent width of the iron line, while the observed flux have decreased by about 40%. This indicates that the iron line emitting region is close ( $< 1.4$  pc) to the continuum emitting region.

The cold matter in our line of sight inferred from the low energy absorption ( $2 - 3 \times 10^{22}$  cm $^{-2}$ ) can only give an iron line equivalent width of 20 - 30 eV even if the matter covers  $4\pi$  steradian around the nucleus (Inoue 1990[67]). The apparent excess of the iron equivalent width over the value expected from the absorption column density has often been found in Seyfert 1's. On the analogy of Seyfert 1's, one may argue two possibility to explain this "excess" iron line: the reflection and warm absorber models. The first model (reflection), however, is rejected for NGC 2110, because no significant reflection component

is required in the Ginga spectrum. The second model (warm absorber) is also implausible because the observed line and edge energy requires low ionization iron which would make significant L-shell absorption.

Here we propose a two-phase "cold" matter model for the origin of the iron features. One "cold" (to iron) material has an equivalent hydrogen column density larger than  $\sim 10^{23}\text{cm}^{-2}$ , but still thin against the Thomson scattering ( $< 10^{25}\text{cm}^{-2}$ ). This material partially covers the nucleus and produces the main part of the iron line and edge features. In addition, the other cold material of  $\sim 10^{22}\text{cm}^{-2}$  totally covers the nucleus and BLR. This material is responsible to the optical obscuration and the X-ray low energy absorption. Geometrically, it should be doughnut-shaped in order to explain the asymmetrical structure observed in the optical and radio wavelength.

Accordingly, we have examined the following dual absorber model, where the extra soft X-ray emission is represented by a thermal plasma model.

$$F(E) = \{[K_{abs}E^{-\Gamma} + \text{Gaussian}] \exp(-\sigma(E)N_{H_{int}}) \times \{C_f \exp(-\sigma(E)N_{H_{pc}}) + (1 - C_f)\} + T(E, T_e, Z, EM)\} \exp(-\sigma(E)N_{H_{Gal}}),$$

where  $N_{H_{pc}}$  and  $C_f$  are the equivalent hydrogen column density and the covering fraction of a partially covering material, respectively. This model satisfactorily reproduced the SIS spectra with  $\chi^2_\nu$  of 1.0 for 391 d.o.f. The best-fit parameters and their 90% confidence ranges are given in table 15. This parameter set can produce an iron line with equivalent width of  $\simeq 100$  eV, even with the cosmic abundance material (Inoue 1990[67]).

Table 15: Dual absorber model for the ASCA SIS spectra of NGC 2110

	Parameter[Unit]	Best-fit value (90% range)
Absorption	$N_{HGal}[10^{22}\text{cm}^{-2}]$	0.186(fixed)
	$N_{Hint}[10^{22}\text{cm}^{-2}]$	2.99(2.6-3.4)
	$N_{Hpc}[10^{22}\text{cm}^{-2}]$	18.6(7.8-32.3)
	$C_f$	0.32(0.13-0.47)
Power-law	$\Gamma$	1.69(1.44-1.94)
	$K_{abs}[10^{-3}\text{photonss}^{-1}\text{keV}^{-1}\text{cm}^{-2}]$	9.2(5.4-16)
Gaussian line	Energy [keV]	6.38(6.35-6.41)
	Width [keV]	0.05 (fixed)
	Intensity [ $10^{-5}\text{photonss}^{-1}\text{cm}^{-2}$ ]	4.7(3.3-6.1)
Thermal plasma	$kT_e[\text{keV}]$	1.05(0.88-1.29)
	Z [relative to solar]	0.07(0.02-0.17)
2-10 keV flux	Observed [ $10^{-11}\text{ergs}^{-1}\text{cm}^{-2}$ ]	2.6
	Absorption corrected [ $10^{-11}\text{ergs}^{-1}\text{cm}^{-2}$ ]	3.8
reduced $\chi^2$ (dof)		1.0 (391)

Note: Redshift is taken into account for all values except the Galactic absorption.

We further expect that the partially covering material and the totally covering material are respectively the BLR clouds and the obscuring torus in the unified scheme. The FWHM of the 6.4 keV iron line gives the Doppler velocity to be less than  $1 \times 10^4 \text{ km s}^{-1}$ . This is reasonable for the velocity of the BLR clouds. On the other hand, Mushotzky et al. (1995[115]) recently reported the detection of "broad" iron  $K\alpha$  lines from two Seyfert 1's with the ASCA satellite. They obtained the FWHM corresponding to the Doppler velocity larger than 2 or  $3.5 \times 10^4 \text{ km s}^{-1}$  and interpreted these to be the accretion disc origin.

We have found that the extra soft X-ray emission can be modeled by either electron scattered X-rays or thermal plasma emission. From the ASCA observation alone, however, we cannot discriminate these two possibility. Our extrapolated 0.1 - 2.4 keV observed flux of this emission is  $4.2 \times 10^{-13} \text{ ergs s}^{-1} \text{ cm}^{-2}$  for the scattered X-rays model and  $2.8 \times 10^{-13} \text{ ergs s}^{-1} \text{ cm}^{-2}$  for the thermal plasma emission model; both are the same as the BBXRT estimation of  $3 - 4.5 \times 10^{-13} \text{ ergs s}^{-1} \text{ cm}^{-2}$  (Weaver et al. 1995[194]). Therefore we conclude that the extra soft X-ray emission has been almost constant at least between the BBXRT and the ASCA observations. This supports the suggestion by Weaver et al. (1995[194]) that the extra soft X-ray emission comes from the extended region resolved with the ROSAT HRI.

## 4.7 Other Seyfert 2s observed with ASCA

PKS B1319-164, NGC 7319, and NGC 4388

### 4.7.1 PKS B1319-164

**Introduction to PKS B1319-164** There was no X-ray data for PKS B1319-164 before ASCA ( The ROSAT all sky survey may have detected the soft X-rays from PKS B1319-164, but it was not listed in the paper titled "ROSAT All Sky Survey observations of IRAS galaxies" by Boller et al. 1992 ).

This "warm" IRAS AGN was labeled a reddened Seyfert 2 by Osterbrock & De Robertis (1985 [127]) and is one of the brightest Seyfert 2's discovered by IRAS (De Grijp et al. 1985 [32]). Further discussion of the optical spectra, IUE spectra, and optical imaging of this galaxy are presented in De Robertis, Hutchings, & Pitts (1988[33]). The nucleus is reddened by  $E_{B-V}=0.3$  mag, both in the lines and continuum. This galaxy had exceptionally interesting emission line characteristics. For example, the emission-line profiles were among the broadest for Seyfert 2's, having full widths at zero intensity (FWZI) of over 4000 km s<sup>-1</sup>. Since it was not clear whether the IRAS selected AGNs were intrinsically similar to or different from optically selected AGNs at all wavelengths, and because PKS B1319-164 was an interesting and apparently bright Seyfert galaxy, it was a good candidate to study in the X-ray with the ASCA satellite. After correcting for Galactic interstellar polarization and the fraction of the total flux due to starlight  $F_g$  of 85 %, the continuum polarization is about 7.4 % (Kay 1994 [76]). The polarization and polarized flux seem basically constant with wavelength.

**ASCA observation of PKS B1319-164** PKS B1319-164 was observed on 1995 July 18 of effective exposure time for the SIS and the GIS, respectively of about 36.1 ks and 38.0 ks.

PKS B1319-164 has a bright companion galaxy about 2' to the east (De Robertis, Hutchings, & Pitts 1988[33]). This galaxy similar in size and brightness in optical wavelengths and is clearly an inclined spiral. There is no apparent luminous connection between the two in optical wavelengths, but they may be at the same distance . To check whether the X-ray flux observed by the ASCA comes from 1319-164 or the bright companion, We made the X-ray images in in the 0.5-2 keV and 4-10 keV band. Both images have only one bright source at  $(\alpha, \delta_{2000}) = (203.603, -16.731)[\text{deg}, \text{deg}]$ , which is identified with PKS B1319-164.

**X-ray spectra of PKS B1319-164** The spectra of PKS B1319-164 is shown in figure 58. The overall spectra is similar to those of IC5063 and NGC 4507, except that the flux ratio of the soft excess to the hard flux is larger than in IC5063 and NGC 4507 spectra. The fall of flux in PKS B1319-164 spectra around 2-3 keV suggests that the spectral component dominating above 3 keV is suffering heavy absorption. We first apply a power-law model given in formula 1.

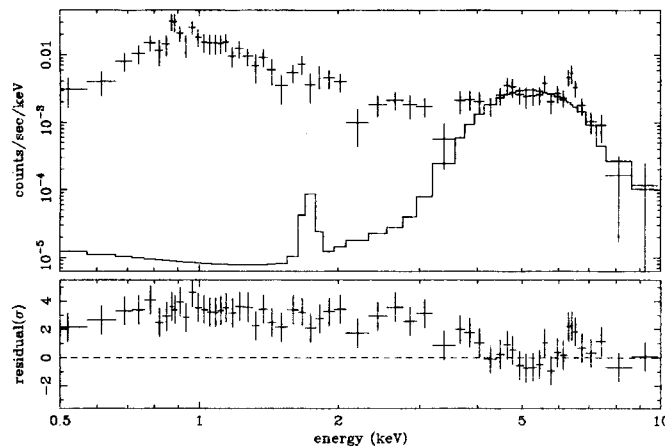


Figure 23: The same as in figure 6, but for PKS B1319-164

The best-fit model function is shown with the SIS1 data in figure 23. This model was rejected with a reduced  $\chi^2$  of 6.4 for 227 degrees of freedom (dof). The best-fit photon-index and hydrogen-equivalent column density are 3.68(3.31-4.06) and 6.2(5.6-6.7)  $\text{H atom cm}^{-2}$ , respectively.

More flux is seen at soft X-ray energies than expected from a simple extrapolation of the hard X-ray continuum covered by a cold photoelectric absorber, requiring an additional component to be fit. We therefore moved to a model function given in the formula 2.

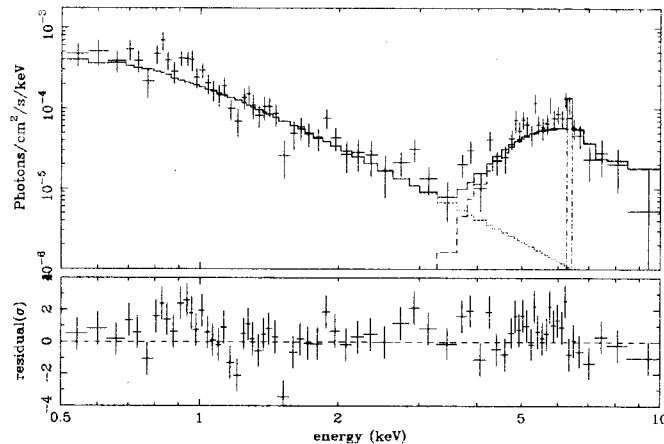


Figure 24: The same as in figure 7, but for PKS B1319-164

The best-fit model function de-convolved with the response is shown with SIS0 data in figure 9. The best-fit parameters are listed in table 19. The reduced  $\chi^2$  is 1.34 for 222 degrees of freedom (dof). The hard band ( $>3$  keV) flux is dominated by a power-law component having the photon index of 4.1(3.3-4.9) absorbed by the hydrogen-equivalent column density of  $< 7.6(6.4 - 8.9) \times 10^{23} \text{H atom cm}^{-2}$  (hard component). The soft band ( $<3$  keV) flux is dominated by a power-law component having the photon index of 3.0(2.7-3.4) absorbed by the hydrogen-equivalent column density of  $< 1.2(0.7 - 1.9) \times 10^{21} \text{H atom cm}^{-2}$  (soft component). The best fit center energy of line is 6.51(6.36-6.57) at the rest frame, and the equivalent width of it is 201(104-311) eV.

The photon index is much larger than the typical value ( $\sim 1.7$ ) seen in Seyfert galaxies. So we try another fit where the photon index of the hard component is fixed to 1.7. The best-fit parameters are shown in table 19. The reduced  $\chi^2$  is 1.50 for 223 degrees of freedom (dof). The hard component is fitted with a power-law component having the photon index of 1.7(fixed) absorbed by the hydrogen-equivalent column density of  $4.1(3.7 - 4.6) \times 10^{23} \text{H atom cm}^{-2}$ . The soft component is reproduced by a power-law component having the photon index of 3.2(2.9-3.6) absorbed by the hydrogen-equivalent column density of  $1.6(1.0 - 2.3) \times 10^{21} \text{cm}^{-2}$ . The best fit center energy of line is 6.39(6.35-6.54) at the rest frame, and the equivalent width of it is 327(220-450) eV. The column density for the hard component reduced, and the equivalent width of  $\sim 6.4$  keV line increased. The other parameters for the soft component and the line do not change within the errors.

#### 4.7.2 Discussion for PKS B1319-164

The ASCA spectra of PKS B1319-164 also show the heavily absorbed component with an Fe K line at hard energies, suggesting the Sy1-like nucleus obscured at the center of the galaxy. The intrinsic photon index of the hard component was found to be 4.1(3.3-4.9), which is much larger than the typical value for AGNs. We could attributed the steep slope to the limited energy band used in the fitting. As seen in figure 24, the spectral parameters of the hard component was determined mainly from the data above 4keV. In most portion of the energy band, the intrinsic photon index is subject to a heavy absorption. Moreover the energy band includes Fe K lines. So the fitted photon index could be systematically larger than the true value except in the ideal case, in which the model perfectly describes the true spectrum and no significant systematic error is introduced during the data reduction. To determine the intrinsic slope of PKS B1319-164, we needs more photons and a energy band extended to higher energies. Because of the lack of information about the slope, we also try the fit with the photon index fitted to 1.7, the typical value for AGNs. As the results, the spectral parameter for the soft component and the Fe K line does not change with in errors except the absorption column for the hard component (table 19). The center energy of Fe K line is 6.51(6.36-6.57) consistent with that of the neutral iron.

The most prominent feature of PKS B1319-164 is the large flux and the steepness of the soft component compared with IC 5063 and NGC 4507. The photon index of the soft component is 3.0(2.7-3.4), reminding us the exponential cut-off of thermal emission. Many line-like features are seen around 0.8-1 keV in the spectra. We fit the features with a narrow Gaussian profile and get the center energy of 0.96(0.90-0.99)keV and the flux of  $2.9(1.9-3.9) \times 10^{-5}$  photons  $s^{-1} cm^{-2}$ , which can be interpreted as an emission-line blend of various L-shell transitions of Fe XVII-FeXXIV and NeIX-NeX  $K\alpha$  from thermal or photoionized plasma.

We fit the soft component of PKS B1319-164 with the RS model instead of the power-law model. The model improves the fit by  $\Delta\chi^2 = -17$  and gives the temperature of  $kT = 1.0(0.9-1.1)$  with the metal abundance of 0.07(0.04-0.11) solar. This temperature with the low metal abundance reminds us X-ray spectra from early type galaxies. The 0.5-4.5 keV luminosity of the soft component of PKS B1319-164 is  $\log(L_X/ergs s^{-1}) = 41.8$ , which is comparable with that of the most luminous early type galaxies observed with ASCA (Matsumoto 1994[99]). However, whether PKS B1319-164 is a early type galaxy is not clear. The optical images, by De Robertis et al. (1988[33]), indicates that PKS B1319-164

is rather bright, with an overall elliptical shape. No normal spiral features are seen, broad asymmetries on the E and NE of the galaxy. The most significant structure, however, is seen within  $8''$  of the nucleus. There is a loop to the SW and a region of higher luminosity to the E and NE. These also do not resemble normal spiral features and suggest rather some disturbance in the inner galaxy, possibly direct associated with the nucleus.

We also try the power-law model with recombination lines from photo ionized plasma by using the code, XSTAR. Recombination lines from thin plasma with the ionization parameter (see Appendix B) of  $\log(\xi) = 1.4$  also accounts for the feature around 0.9-1 keV.

The results of three different models for soft component are summarized in table 16. For these models, the fitted spectral parameter for the hard component and the Fe K line do not change from those listed in table 19, within errors. We could not distinguish between thermal and photo-ionized plasmas with the ASCA spectra of PKS1319-164.

Table 16: Results of model fits for the soft component of PKS B1319-164

	Photon index or $kT$	$\log(\xi^*)$	$A_b^\dagger$ (solar)	reduced $\chi^2$ (dof)	$\Delta\chi^2$
Power law	3.2(2.9-3.6)	—	—	1.34(222)	0
Thermal plasma	1.0(0.9-1.1) keV	—	0.07(0.04-0.11)	1.27(221)	-17
Photo ionized plasma	3.0(2.6-3.4)	1.4(1.3-1.6)	1 (fixed)	1.22(220)	-30

Note:

\*  $\xi$  is a ionization parameter ( see Appendix B)

†  $A_b$  is a metal abundance.

### 4.7.3 NGC 7319

**Introduction to NGC 7319** This galaxy in Stephan's quintet was identified as a Seyfert 2 by Huchra et al.(1982[64]). It has a classical Seyfert 2 spectrum. The flux spectrum is weak in the blue, so the polarization data are quiet noisy below  $400 \text{ \AA}$ . The uncorrected polarization is about 1%, the starlight corrected polarization is about 5.6 %, and the [OIII] and  $H\beta$  lines can be seen weakly in the noisy polarized flux spectrum. It is quite possible that the galaxy polarization is interstellar in origin [76].

**ASCA observation of NGC 7319** NGC 7319 was observed on 1994 December 7 with the effective exposure time of the SIS and the GIS of about 31.9 ks and 31.5 ks respectively. NGC 7319 is located in Stephan's quintet, a group of galaxies. We show the SIS images

around NGC 7319 in the 4-10 keV and the 0.5-2 keV bands (figure 25 and 26). In the GIS and SIS image obtained in the 4-10 keV band, NGC 7319 is the only brightest target. In contrast, we can see at least 3 peaks in the soft image. One of them can be attributed to the hard source, though there is a discrepancy in position of about 10 arcsec. The remaining two sources is probably associated with a group of galaxies. We lists the peak positions in table 17.

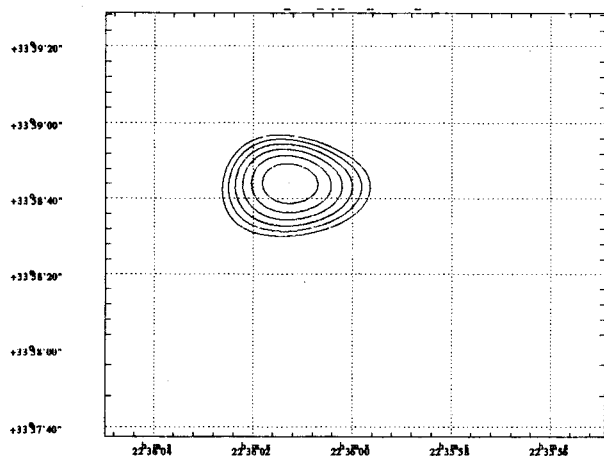


Figure 25: The 4-10 keV contour image of NGC 7319

This is the combined image from two detectors, SIS0 and SIS1. The only bright source is NGC 7319. Grids are drawn in  $(\alpha, \delta)$  coordinates of epoch 2000.

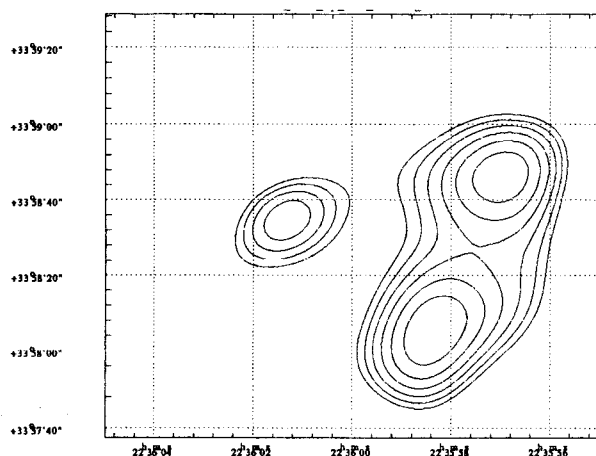


Figure 26: The 0.5-2 keV contour image of NGC 7319

This is the combined image in 0.5-2keV band from two detectors, SIS0 and SIS1. Near the position of the hard X-ray source seen in figure 25, we can also see a soft X-ray peak. The peaks has a offset of  $\sim 10$  arcsec.

Other two peak are detected in soft X-ray, which is probably associated with Stephan's quintet, a group of galaxies. however, the positions of X-ray peak does not coincident with those of any galaxies in the group, but is placed in the intergalactic region.

Table 17: Source positions in the ASCA SIS image of NGC 7319

	SIS 0.5-2 keV	SIS 4-10 keV	ID
Source	(RA, DEC) <sub>epoch2000</sub>	(RA, DEC) <sub>epoch2000</sub>	
A	(339.006, 33.976)	(339.003, 33.978)	NGC 7319
B	(338.987, 33.981)	—	—
C	(338.993, 33.968)	—	—

**X-ray spectra of NGC 7319** We have extracted spectra from a region of 6' diameter for SIS and GIS. This region includes all three soft peaks mentioned above. Thus the extracted soft spectrum does not describes the true one of NGC 7319, and the flux is overestimated. However, the extracted hard spectrum is still expected to give the intrinsic spectrum of NGC 7319, because of the absence of hard sources except NGC 7319.

The spectra of NGC 7319 is shown in figure 59. The overall spectra is similar to those of PKS B1319-164. There is a fall of flux around 3 keV in the spectra. This suggests that the spectral component dominating above 3 keV is heavily absorbed.

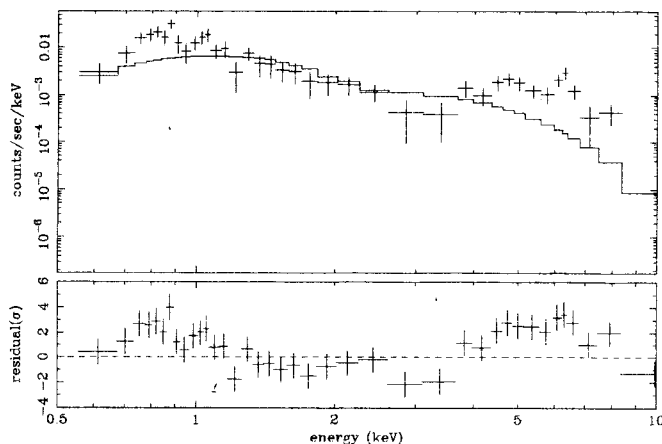


Figure 27: The same as in figure 6, but for NGC 7319

We apply the model of formula 1 and the best-fit model function is shown with the SIS0 data in figure 27, although the model was rejected with a reduced  $\chi^2$  of 3.60 for 118 degrees of freedom (dof).

The best-fit photon-index and hydrogen-equivalent column density are 1.64(1.46-1.83) and  $< 2.5 \times 10^{20} \text{H atom cm}^{-2}$ , respectively.

More flux is seen at soft and hard X-ray energies than expected from a simple power-law model. The soft excess is a sum of the soft X-rays intrinsic to NGC 7319 and those from Stephan's quintet.

We then tried a model of formula 2: two-component model with an iron line. The best-fit model function is shown with SIS0 data in figure 28 and the best-fit parameters are listed in table 19. The reduced  $\chi^2$  is 1.37 for 113 degrees of freedom (dof). The hard band ( $> 3 \text{ keV}$ ) flux is dominated by a power-law component having the photon index of 1.4(1.6-3.0) absorbed by the hydrogen-equivalent column density of  $3.3(1.1 - 4.7) \times 10^{23} \text{H atom cm}^{-2}$ . The soft band ( $< 3 \text{ keV}$ ) flux is dominated by a power-law component having the photon index of 4.5(3.8-5.5) absorbed by the hydrogen-equivalent column density of  $3.5(2.3 - 5.1) \times 10^{21} \text{H atom cm}^{-2}$ . The best fit center energy of line is 6.49(6.40-6.55) at the rest frame, and the equivalent width of it is 624(358-852) eV.

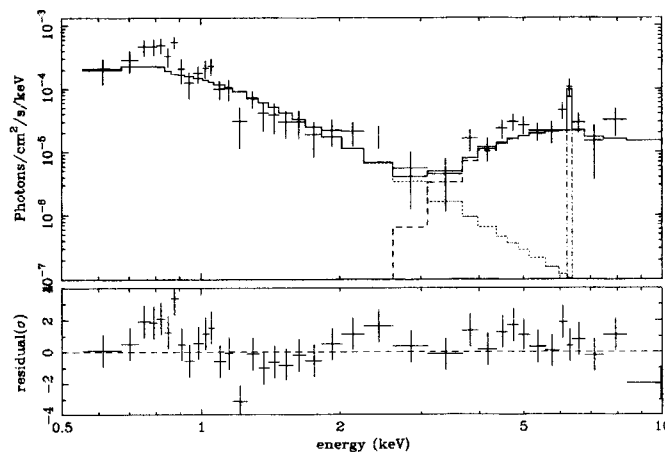


Figure 28: The same as in figure 7, but for NGC 7319

The steep slope of the soft component reminds us thermal component. In fact, the soft spectra have excess around 0.9-1.1 keV above the power-law model, attributable to Fe L and Ne  $K\alpha$  emission lines. However, we can not resolve individual sets of lines as we did in NGC 1068 spectra. We fit the soft component with the RS thermal plasma model, and get a improved fit with  $\Delta\chi^2 = -30$ . The best fit temperature and the metal abundance are

$kT = 0.80(0.70-0.87)$  and  $A_b = 0.08(0.04-0.14)$ solar, respectively, with the reduced  $\chi^2 = 1.11$  for dof of 112.

#### 4.7.4 Discussion for NGC 7319

We detected the hard X-ray in Stephan's quintet. The source position coincides with a type 2 Seyfert galaxy NGC 7319. The hard X-ray spectra show a low energy cutoffs and strong Fe K emission which is characteristic of type 2 Seyferts.

We estimated what fraction of soft X-ray emission in Stephan's quintet is attributable to NGC 7319. We try the decomposition of the soft component. We made spectra of three soft X-ray peak listed in 17. Each spectra was extracted from the small region centered on the peak with the diameter of 1 arcmin. Because of limited numbers of photons, we sum up the photons into 5 bins, whose energy ranges are 0.5-1 keV, 1-2 keV, 2-4 keV, 4-8 keV and 8-10 keV. To comparison of the spectral slopes of the X-ray peak A, B, and C, we fit the spectra with a double power-law model after the background subtraction. The parameters for the hard component (the photon index, the absorption, and the parameters for the Fe K line) were fixed at the values obtained with the hard source spectra extracted from the 6 arcmin-diameter region, except the normalizations. We allowed the normalization of the hard component and the Fe K line to change in the fit, but forced the ratio of them to be constant. This would reproduce the leak emission from the hard X-ray. For soft component, the normalization of the soft component was allowed to change independently, and the intrinsic absorption was fixed to zero for the sake of good quantifying the slopes with limited S/N spectra. We get the best fit slope of Source A, B, and C are 3.8(3.1-4.5), 4.4(3.0-6.0), and 5.0(4.2-6.1). We found no difference in the photon indexes of Source A, B, and C spectra within the errors.

Source A, B, and C account for 30, 50, and 20 percent of the soft flux dropped in the 6 arcmin-diameter region, assuming that the whole soft flux is decomposed to those from tree point sources located at Source A, B, and C. Thus the soft emission intrinsic to NGC 7319 is less than 1/3 of observed flux in the 6 arcmin-diameter region.

#### 4.7.5 NGC 4388

**Introduction to NGC 4388** NGC4388 is known to have Seyfert 2 nucleus and extended emission line region which require a powerful ionizing source hidden from our view (Colina 1992[26]). Hanson et al. (1990[58]) discovered NGC4388 is the most luminous source at hard

X-ray in the Virgo cluster using a coded mask X-ray telescope (SL2XRT). Their spectrum shows strongly absorbed continuum of power-law which has photon index 1.5(1.0-2.4) and  $N_{\text{H}} = 2.1(0.7 - 4.9) \times 10^{23} \text{H atom cm}^{-2}$ .

**ASCA observation of NGC 4388** NGC4388 is present in the GIS and the SIS f.o.v. during a observation of the Virgo cluster of galaxies region. We observed this source on 1993 July 4 and obtained the effective exposure time of the SIS and the GIS of 20.0 ks and 20.7 ks respectively.

**X-ray image around NGC 4388** The sliced profile across NGC4406-NGC4388 region (along X-axis of the GIS detector) demonstrates that the emission of NGC4406 is spread to the NGC4388 position. Thus the underlying diffuse emission other than NGC 4388 is a sum of the intracluster gas of the Virgo, extent from the NGC 4406 and the CXB. NGC 4388 is the brightest source at hard X-rays of  $E > 4 \text{ keV}$  ( figure 29). In the soft X-ray band below 2 keV, X-rays from NGC 4388 is also detected, although faint, at the flux level of about  $2 \times 10^{13} \text{ erg s}^{-1} \text{ cm}^{-2}$ ( figure 30). We lists the X-ray positions of sources in table 18. The position of soft X-ray emission from NGC 4388 coincides with that of hard emission.

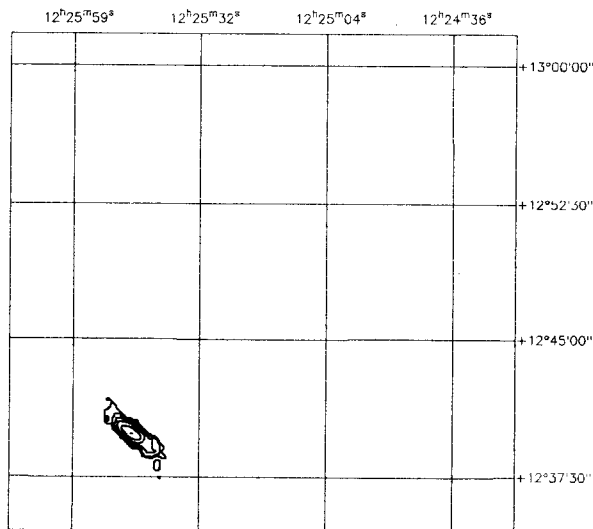


Figure 29: The 4-10 keV countour image of NGC 4388

This is the combine image from two detectors, SIS0 and SIS1. The only bright source is NGC4388. The elongation of contour is not intrinsic, but due to the response of X-ray telescope.

Grids are drawn in  $(\alpha, \delta)_{\text{epoch2000}}$  coordinates.

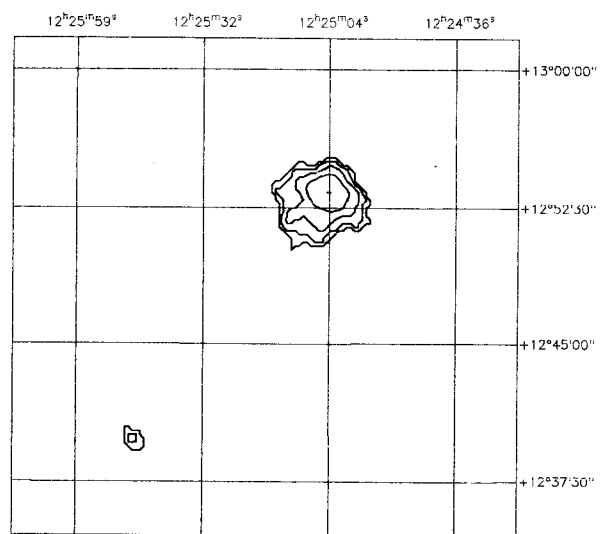


Figure 30: The 0.5-2 keV countour image of NGC 4388

This is the combine image in 0.5-2keV band from two detectors, SIS0 and SIS1. Though the emission from NGC4388 is faint at these energies, still the ASCA detected it.

The bright source seen in the upper-right of NGC4388 is a early type galaxy, NGC 4374 ( or called M 84).

Table 18: Source positions in the ASCA SIS image of NGC 4388

	SIS 0.5-2 keV	SIS 4-10 keV	ID
Source	$(\text{RA}, \text{DEC})_{\text{epoch2000}}$	$(\text{RA}, \text{DEC})_{\text{epoch2000}}$	
A	(186.446, 12.664)	(186.445, 12.665)	NGC 4388
B	(186.268, 12.890)	—	M84(N4374)

**X-ray spectra of NGC 4388** We made background spectra from the near sky to cancel the contaminations from the Virgo cluster and the member galaxies. The spectra of NGC 4388 is shown in figure 60. There is a drop of flux around 3 keV in the spectra. This suggests that the spectral component dominant above 3 keV is heavily absorbed.

A simple power-law model (formula 1) is rejected with reduced  $\chi^2$  is 1.9 for 164 degrees of freedom (dof). The best-fit photon-index and hydrogen-equivalent column density are 0.90(0.51-1.30) and  $2.6(2.1 - 3.2) \times 10^{23} \text{H atom cm}^{-2}$ , respectively. We therefore tried formula 2 and obtained nice fit with the reduced  $\chi^2$  is 1.03 for 159 degrees of freedom (dof).

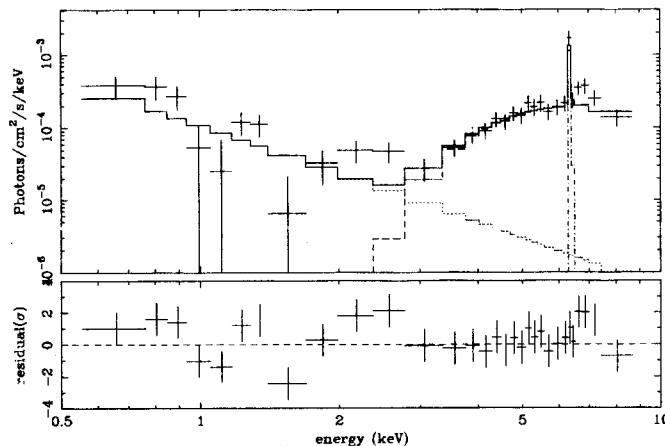


Figure 31: The same as in figure 7, but for NGC 4388

The best-fit model function is shown with SIS0 data in figure 31, while the best-fit parameters are listed in table 19. The hard band ( $>3$  keV) flux is dominated by a power-law component having the photon index of 0.8(0.40-1.2) absorbed by the hydrogen-equivalent column density of  $2.5(1.9 - 3.1) \times 10^{23} \text{H atom cm}^{-2}$ . The soft band ( $< 3$  keV) flux is dominated by a power-law component having the photon index of 2.2(1.7-3.0) absorbed by the hydrogen-equivalent column density of  $< 1.0 \times 10^{21} \text{H atom cm}^{-2}$ . The best fit center energy of line is 6.44(6.40-6.49) at the rest frame, and the equivalent width of it is 515(392-650) eV.

The photon index is a bit smaller than the typical value ( $\sim 1.7$ ) seen in Seyfert galaxies. So we try another fit where the photon index of the hard component is fixed to 1.7, and check the influence to the other parameters. We show the best-fit parameters in table 19. The reduced  $\chi^2$  is 1.09 for 160 degrees of freedom (dof). The hard component ( $>3$  keV) is fitted by a power-law component having the photon index of 1.7(fixed) absorbed by the hydrogen-equivalent column density of  $3.7(3.3 - 4.2) \times 10^{23} \text{H atom cm}^{-2}$ . The soft component ( $< 3$  keV) is fitted by a power-law component having the photon index of 1.9(1.0-

2.5) absorbed by the hydrogen-equivalent column density of  $< 0.5 \times 10^{21} \text{H atom cm}^{-2}$ . The best fit center energy of line is 6.45(6.41-6.50) at the rest frame, and the equivalent width of it is 464(345-593) eV. The column density for the hard component increased. The other parameters for soft components and the line does not change within the errors.

#### 4.7.6 Discussion for NGC 4388

This ASCA observation confirms the result of Hanson et al. and found Fe K emission line at 6.4 keV with EW about 500eV. The ASCA observed flux in the 2-10keV band is lower than that during the SL2XRT observation in 1985 ( $2.1 \times 10^{-11} \text{ erg s}^{-1} \text{cm}^{-2}$ ). It may due to the time variability characteristic of active nucleus.

In the Seyfert 2 galaxies, in addition to the heavily absorbed continuum, the scattered light which appears in soft X-ray band with little absorption is commonly seen. There are some fraction of the light of the hidden nucleus escaping the obscuration to ionize the optical emission line region (Colina 1992[26]). The soft X-ray emission with ASCA is very weak and the spectral shape is reproduced by power-law model with  $\Gamma = 2.2(1.7-3.0)$  However, the ROSAT HRI image of NGC4388 shows an extended X-ray emission in which the nucleus component has small fraction (about 1 per cent : Piro et al.1994[133]). preferring the starburst origin.

### 4.8 Starburst galaxies observed with ASCA for comparisons with Seyfert 2s

NGC 253, NGC 3079, and M82

We observed three starburst galaxies in which strong Seyfert activity is not observed. To compare with the soft components of Seyfert 2 galaxies, we quantify the shape of the soft spectra with a power-law model. We also took the X-ray flux and luminosity and listed them in table 19, 20 and 21

#### 4.8.1 NGC 253

**Introduction to NGC 253** NGC 253 is a well-studied, nearby example of a starburst/LINER galaxy (McCarthy et al. 1987[104]). Evidence for vigorous star formation in the nucleus of NGC 253 includes large far-infrared luminosity and CO line emission

(Scoville et al. 1985[155]), X-ray emission (Fabbiano and Trinchieri 1984[43]), compact radio sources (Antonucci and Ulvestad 1988[4]), strong narrow-line emission (Moorwood and Oliva 1988[110]; Wright and Joseph 1989[210]), and spectral signatures indicating high velocity outflows (McCarthy et al. 1987[104]). The high rate of gas consumption and evidence for massive stars in NGC 253 suggest a prodigious star formation rate and a correspondingly high supernova rate. Radio observations using the VLA have detected families of compact radio sources, which are believed to be young supernova remnants (SNRs). The supernova rate in the nucleus estimated from these observation is about one every 3 yr (Antonucci and Ulvestad 1988[4]). However, there is no direct optical confirmation of these supernovae(SNs), presumably due to the enormous dust obscuration present (Rieke and Low 1975[145]; Waller et al. 1988[188]).

**ASCA observation of NGC 253** NGC 253 was observed on 1993 June 12, giving the effective exposure time of the SIS of about 22.4 ks.

**X-ray spectra of NGC 253** The spectra of NGC 253 is shown in figure 61.

A power-law model (formula 1) fit , although rejected with the reduced  $\chi^2$  is 1.50 for 129 degrees of freedom (dof), is given in figure 32 together with the SIS data. The best-fit photon-index and hydrogen-equivalent column density are 1.82(1.74-1.91) and  $4.6(1.5 - 7.7) \times 10^{20} \text{Hatomcm}^{-2}$ , respectively.

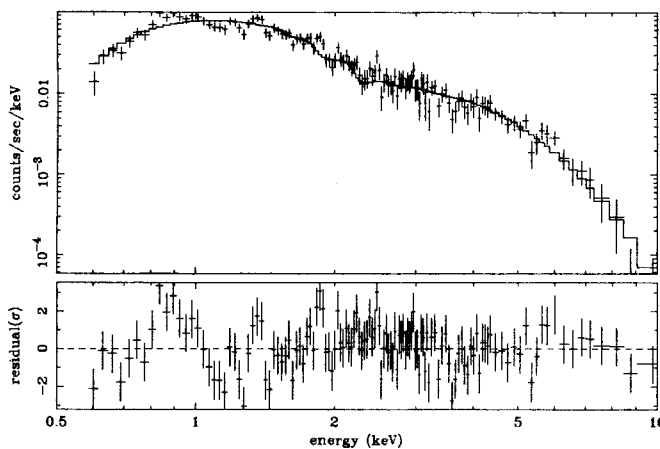


Figure 32: The result of the single power-law model for NGC 253

Only the SIS spectra is shown. A solid line shows the model function of the pow-law modified by a photoelectric absorption (formula 1). The residuals are shown in the bottom panel. The model was fitted with SIS0+1 data.

#### 4.8.2 NGC 3079

**Introduction to NGC 3079** The edge-on Sc spiral galaxy NGC 3079 has been studied extensively at many wavelengths. The galaxy is optically disturbed and dusty, having a Sy2/Liner spectrum (Heckman 1980[62]), extended  $10\mu\text{m}$  emission (Lawrence et al. 1985[91]), and a far-infrared excess (IRAS Point Source Catalog 1985). NGC 3079 shows evidence for compact nuclear activity as well as starburst activity. The galaxy displays two kpc-scale radio lobes (Duric & Seaquist 1988[36]) as well as a smaller  $\text{H}\alpha$  loop (Ford et al. 1986[48]) or superbubble (Veilleux et al. 1994[184]), extended along its minor axis. At high resolution the lobes display significant complexity and appear to originate from a compact VLBI double core (Irwin & Seaquist 1988[69]). The superwind as evidenced from the radio and  $\text{H}\alpha$  emission along the minor axis may be powered by the AGN (Filippenko & Sargent 1992[46]) or a nuclear starburst (Heckman, Armus, & Miley 1990[61]).

**ASCA observation of NGC 3079** NGC 3079 was observed on 1993 May 9 and the effective exposure time of the SIS was about 32.0 ks.

**X-ray spectra of NGC 3079** The spectra of NGC 3079 is shown in figure 61. A power-law model (formula 1) is rejected with the reduced  $\chi^2$  is 2.40 for 29 degrees of freedom (dof), Nevertheless we show the best-fit result in figure 33 with the SIS data. The best-fit photon-index and hydrogen-equivalent column density are 2.49(2.33-2.73) and  $< 4.6 \times 10^{20} \text{H atom cm}^{-2}$ , respectively.

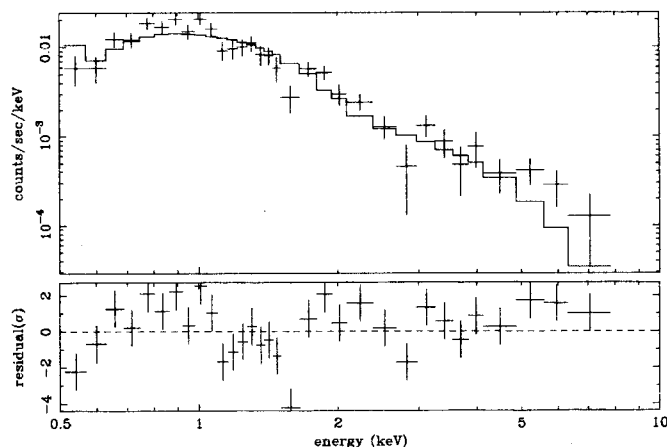


Figure 33: The same as in figure 32, but for NGC 3079

### 4.8.3 M82

**Introduction to M82** M82 is the most active starburst galaxy among nearby galaxies. The supernovae rate in the starburst is estimated to be 0.1-0.3 SNe yr<sup>-1</sup> (Rieke et al. 1980[144]). In the X-ray band, extended hot gas reaching  $\sim$  kpc from the nucleus elongated along the minor axis of the galaxy has been discovered from the Einstein observations (Watson, Stanger and Griffiths 1984[192]; Fabbiano 1988[41]). The inferred temperature of the hot gas ( $> 1$ keV) and the density profile ( $n_e \propto r^{-2}$ ) suggest that the gas is unlikely to be bound by M82 but outflowing from the system at rate of  $\sim 0.7M_{\odot}\text{yr}^{-1}$  (Fabbiano 1988[41]). The X-ray luminosity of M82 is two orders of magnitude higher than other spiral galaxies when  $L_X$  is normalized with  $L_B$ , which is probably related to its unusual starburst activity.

**ASCA observation of M82** M82 was observed on 1993 Apr 19-20, with the effective exposure time of the SIS of about 10.3 ks. The spectra of M82 is shown in figure 61.

**X-ray spectra of M82** A single power law model given in formula 1 is also rejected with the reduced  $\chi^2$  is 2.95 for 173 degrees of freedom (dof). Still for a comparison, we show the best-fit model function with the SIS data in figure 34, where the best-fit photon-index and hydrogen-equivalent column density are 1.67(1.64-1.72) and  $< 1.4 \times 10^{20} \text{H atom cm}^{-2}$ ,

respectively.

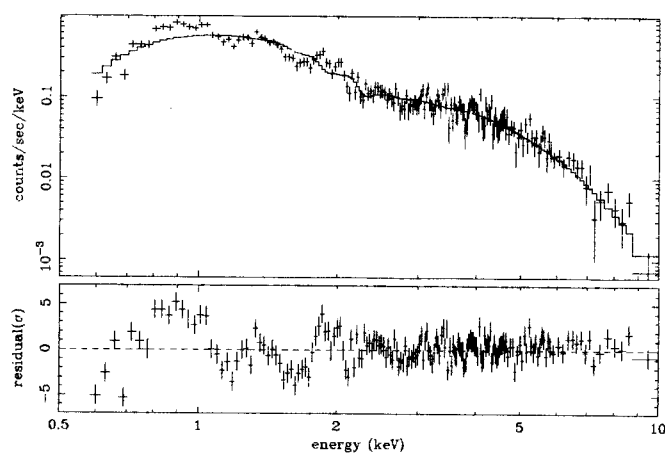


Figure 34: The same as in figure 32, but for M82

Table 19: The best-fit parameters for double power-law model

Fitted component		Hard component		Soft component		Fe K line		$\chi^2$ /d.o.f.	d.o.f.
Parameter	$N_{\text{Hgal}}$ $10^{22} \text{ cm}^{-2}$	$\Gamma_{\text{photon}}$	$N_{\text{H}}$ $10^{22} \text{ cm}^{-2}$	$\Gamma_{\text{photon}}$	$N_{\text{H}}$ $10^{22} \text{ cm}^{-2}$	$E_{\text{C}}$ (rest frame) keV	$EW$ eV		
Units									
[Type 2 Seyferts]									
IC 5063	0.048	1.8(1.6-2.0)	24(22-26)	1.9(1.5-2.4)	<0.11	6.39(6.24-6.46)	80(38-130)	1.12	172
NGC 4507	0.071	1.7(1.5-2.0)	38(35-42)	1.6(1.2-1.9)	<0.043	6.40(6.22-6.42)	140(100-180)	1.19	172
NGC 1808	0.024			2.2(2.1-2.4)	0.13(0.09-0.16)			2.25	169
NGC 1667	0.055			3.8(2.5-7.2)	0.24(0.02-0.80)			1.54	62
NGC 1068	0.031	1.0(0.8-1.3)	2.5(1.7-3.2)	4.9(4.7-5.1)	0.27(0.24-0.30)	6.42(6.40-6.44)	1570(1350-1870)	2.67	672
Mkn 463	0.022	1.4(0.5-2.3)	16(8-24)	2.7(2.4-3.0)	<0.12	6.4(fix)	<670	1.51	39
Mkn 1210	0.035	0.9(-0.2-1.9)	12(<23)	2.6(>2.2)	<1.3	6.53(6.37-6.62)	820(460-1250)	0.87	92
(Mkn 1210)#	0.035	1.7(fix)	20(14-28)	2.4(2.0-3.5)	<0.24	6.45(6.34-6.54)	830(460-1280)	0.88	93
Mkn 477	0.013	0.2(-0.5-1.0)	9(<21)	2.0(1.0-8.6)	<0.93	6.40(6.34-6.45)	490(290-740)	0.90	129
(Mkn 477)#	0.013	1.7(fix)	34(25-46)	1.6(1.2-2.0)	<0.05	6.41(6.33-6.49)	370(170-610)	0.95	130
NGC 2110	0.18	1.5(1.4-1.6)	3.2(2.9-3.5)	1.7(1.0-5.3)	<0.63	6.41(6.38-6.45)	150(110-190)	1.36	356
PKS B1319-164	0.055	4.1(3.3-4.9)	76(64-89)	3.0(2.7-3.4)	0.12(0.07-0.19)	6.51(6.36-6.57)	200(100-310)	1.34	222
(PKS B1319-164)#	0.055	1.7(fix)	41(37-46)	3.2(2.9-3.6)	0.16(0.10-0.23)	6.39(6.35-6.54)	330(220-450)	1.50	223
NGC 7319	0.075	1.4(-0.2-2.2)	33(11-47)	4.5(3.8-5.5)	0.35(0.23-0.51)	6.49(6.40-6.55)	620(360-850)	1.37	113
NGC 4388	0.027	0.8(0.40-1.2)	25(19-31)	2.2(1.7-3.0)	<0.10	6.44(6.40-6.49)	520(390-650)	1.03	159
(NGC 4388)#	0.027	1.7(fix)	37(33-42)	1.9(1.0-2.5)	<0.053	6.45(6.41-6.50)	460(340-590)	1.09	160
[Starburst]									
M 82	0.043			1.76(1.73-1.81)	<0.004			3.04	173
NGC 253	0.013			1.83(1.76-1.93)	0.03(0.01-0.07)			1.50	126
NGC 3079	0.0084			2.52(2.36-2.76)	<0.04			2.41	29

Notes. Table 19, 20, and 21 give fitted parameters, flux, and luminosity when we applied a double power-law model. These values are used in the next section to discuss the statistical properties of type 2 Seyfert galaxies. The 90% confidence regions are given in parentheses.

For the sake of comparison of soft-band emission, we applied a single power-low model and listed the parameterized values for flux NGC 1808, NGC 1667. See the individual source's part for the results of applying a two-component model, in which the soft components are fitted with a thermal plasma model.

We also list three starburst galaxies, whose soft-band emission were parameterized with a single power low model to be used in the next section for the comparison of soft-band activity between type 2 Seyferts and starburst galaxies.

#: Photon indexes of hard component were frozen to be 1.7.



#### 4 OBSERVATIONS AND RESULTS OF INDIVIDUAL SOURCES

93

Notes. See the notes of table 19.

To calculate luminosity, we assumed the distances listed in table 4.

#: Photon indexes of hard component were frozen to be 1.7.



Notes. See the notes of table 19.

To calculate luminosity, we assumed the distances listed in table 4.

#: Photon indexes of hard component were frozen to be 1.7.

\*: These "absorption-corrected" values are given when we assume all observed photons in the iron emission line cross the absorbing column which is evaluated from the cutoff of hard X-ray component. Note that this is the extreme case because the absorber itself emits iron-line photons.

## 5 Discussion for the ASCA sample of type 2 Seyfert galaxies

### 5.1 Properties of hard components and Comparison with Seyfert 1 galaxies

#### 5.1.1 Time Variability

Short time variabilities provide compelling evidence that the emission comes from a compact active galactic nucleus. Variabilities of a few hours have been found in IC 5063 (Koyama et al 1992[82]) and NGC 2110 (Hayashi et al 1996[60]) during the Ginga observations. The present ASCA observations, including IC 5063 and NGC 2110, show no significant variability of time scale shorter than one day, the typical observational time span for each target. Thus we search for a longer term variability by comparing the ASCA flux with the previous observations.

The 2-10 keV fluxes obtained with EXOSAT, Ginga, SL2XRT (for NGC4388), and ASCA are given in figure 35 with the epochs of the observations for each data point. We found most of the Seyfert 2s, except for NGC4507 show the flux decrease from EXOSAT and Ginga to ASCA observations. Since the mutual calibration with different response and energy band, in particular for the absolute flux, is difficult and may have larger systematic errors than the nominal statistical error, we can not conclude for a small variability. However, we safely say that the large variations by factor of 2-3 between the Ginga and ASCA observations found in IC5063, NGC2110, and NGC1808 are real. In the period of the ASCA observation, the hard X-ray emission of NGC1808 can be explained by only LMXB's flux evaluated from the blue-band luminosity  $L_B$ , and does not require the AGN emission.

Since general trend of apparent flux decrease would be partly due to a systematic error between these different instruments, flux increase found in NGC 4507 would be more realistic. Typical interval of the observations between these satellites is  $\sim 5$  year. Thus we can conclude that at least about half of the total hard X-rays comes from a compact region smaller than 2 pc. NGC 4388 and NGC 1068 show small flux variation, but perhaps would be constant within possible systematic errors. The absence or no large variability in NGC 1068 is consistent with the scenario that even the hard X-rays are due the scattering, hence possible X-ray variability of the central source would be smeared by the intrinsically large scattering region.

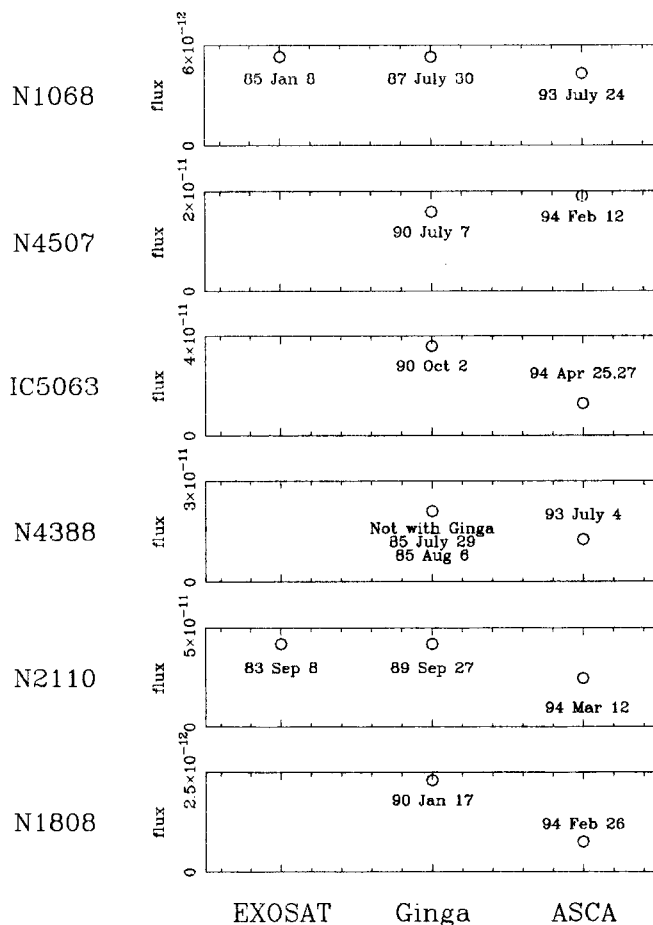


Figure 35: Search for long term variability (hard flux)

We plotted 2-10 keV band fluxes obtained with EXOSAT, Ginga, and ASCA. The decrease of flux by factor of 2 or 3 is seen in several targets between the Ginga and ASCA observations.

The EXOSAT and Ginga fluxes are from Awaki (1991[7])

The data point of NGC 4388 dated on 1985 July 29 and August 6 is obtained with a coded mask X-ray telescope, SL2XRT (Hanson et al 1990[58])

### 5.1.2 Luminosity

We compared luminosities of Seyfert 1 and 2 galaxies in figure 36. For Seyfert 2s we correct absorption using the best-fit value. To take into account the selection effect due to detection limits, we plot the luminosities against the redshifts.

NGC 1068, NGC 1808, and NGC 1667 are fainter than Seyfert 1s. The faintness of NGC 1068 has been explained by the scattering model, in which only a few % of the total luminosity is scattered and come into our line of sight. The same explanation is not excluded for NGC 1808 and NGC 1667, because the large upper limits of the equivalent widths of 6.4 keV line of 0.6 and 2.9 keV, respectively, are at least consistent with the scattering model. However, the weak [OIII] $\lambda$ 5007 emission lines coming from the narrow line region prefer a simple idea that NGC 1808 and NGC 1667 have intrinsically low AGN activity.

The other Seyfert 2s which show heavily absorbed hard X-ray components, have intrinsic luminosities similar to those of Seyfert 1s. Therefore, our X-ray data suggest that most of the Seyfert 2 galaxies have the same level of activities as those of Seyfert 1s.

High luminosity type-1 AGNs (Seyfert 1s) in figure 36 are usually called quasars instead of Seyfert 1s. Extensive searches for a heavily absorbed quasar have been performed, but no AGN with X-ray luminosity of  $L_X > 10^{45}$  erg s $^{-1}$  and an apparent low-energy cutoff corresponding the absorption column of  $N_H > 10^{23}$  (typical thickness for Seyfert 2s) has been found. An unique exception would be Cygnus A; a spectral deconvolution of the X-rays observed with the Ginga satellite led us to a suggestion that Cygnus A is a proto-type of heavy absorbed quasars (Ueno et al. 1994[179]).

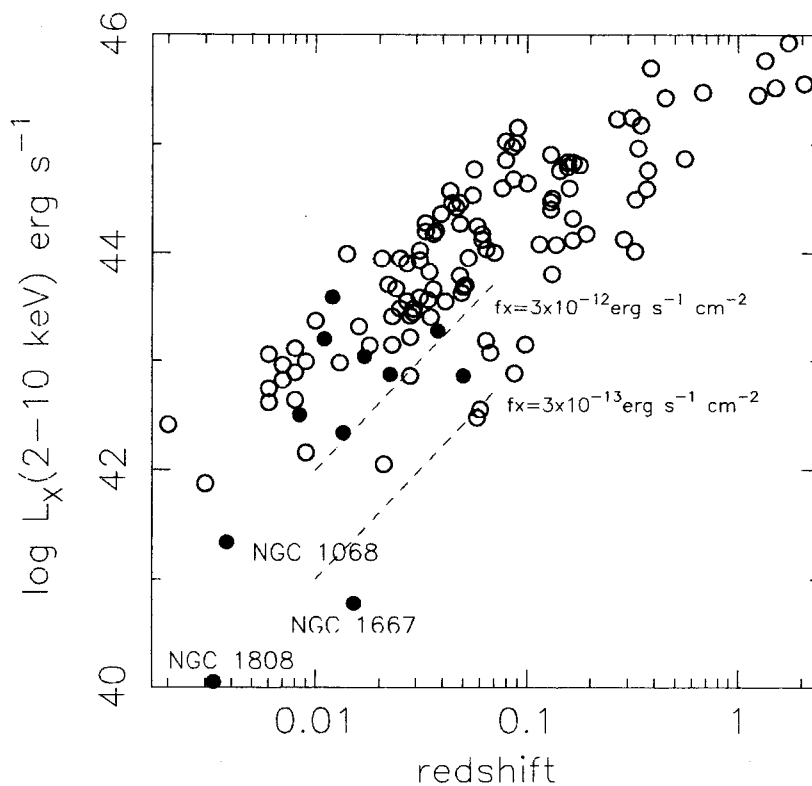


Figure 36: Comparison of  $L_X(2-10 \text{ keV})$  between Seyfert 1 and 2 galaxies

Open and closed circle display type 1 and 2, respectively. We plot the luminosities after corrections for absorption which were evaluated from the spectral fit.

### 5.1.3 Slope

We show the photon indexes of the hard components of our targets in figure 37. Most of the targets have the spectral slopes within the typical range for the type 1s

The simple power-law fit for NGC 1068 and NGC 2110 gives the photon indexes smaller than 1.7, typical value for Seyfert 1s, as show in figure 37. Suppose that the hard emission of NGC 1068 is reflected by cold matter, the intrinsic photon index before the reflection

can be  $\sim 1.9$ . For NGC 2110, the dual absorber model gives the intrinsic photon index of 1.69(1.44-1.94) as shown in the individual section. Thus, both NGC 1068 and NGC 2110 are likely to have photon indexes consistent with those of Seyfert 1s.

The photon indexes of Mkn 1210, Mkn 477, PKS B1319-164, and NGC 4388 also show deviations from the typical value. However we need further observations to conclude on the slope of the hard components, since the limited energy ranges and photon numbers, coupled with the strong low-energy cutoff, make the precise index determination rather difficult for the data of the present exposure time observations.

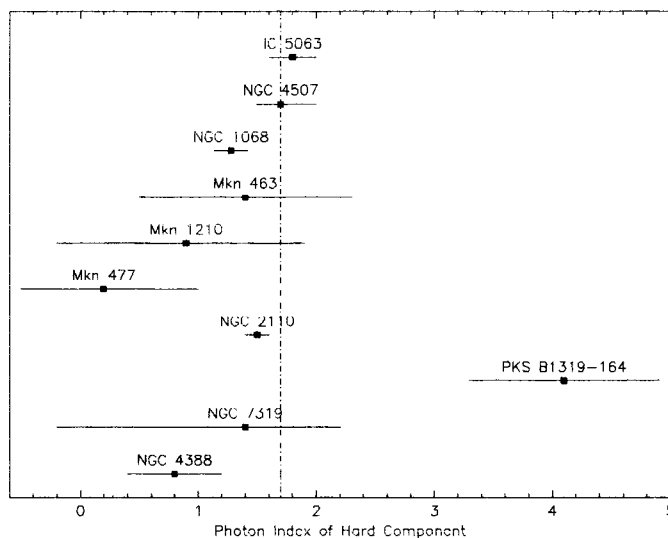


Figure 37: The photon index of hard component

The photon index of hard component and the 90 % error bar are plotted for each objects. The vertical line shows the typical value for AGNs( $\Gamma = 1.7$ ).

## 5.2 The origins of soft components

### 5.2.1 X-ray variability and slopes

A search for soft X-ray variability is particularly important for the unified model. Presence of short time variability, for example, gives strong support that the soft X-rays are directly from a compact AGN in spite of large absorption. The present observations give null constraint on the compact AGN origin, because no short time variability is found in the soft X-rays.

For longer time scale variation, we show the 0.2-4 keV flux obtained with Einstein, ROSAT, and ASCA in Figure 38, with a label of the dates of observations under the data circles.

For the flux comparisons between the different instruments, we have to take into account the differences of energy responses and passbands. When the source has two spectral

components as generally seen in Seyfert 2s, the Einstein and ROSAT fluxes would be dominated by the soft component, while the ASCA soft flux may include both components.

Accordingly, for the ASCA fluxes of NGC4507, IC5063, NGC4388, and Mkn463, we plot 2 circles: the upper is the sum of the soft and hard components while the lower is for the soft component only. For NGC4507, IC5063, and Mkn463, the lower circles are well coincident with the previous results. This may imply that ROSAT and Einstein have detected only the soft component. Here we assume no variability of the soft X-rays from these Seyfert 2s. This assumption is self-consistent with the observed thick absorption column to the AGNs hence no soft X-ray from the AGNs (compact source) can be expected. Also the high-energy cutoff of the detection efficiency of the ROSAT around 2-3keV and the low-energy cut of the flux of heavily absorbed hard component limited the observable flux to be only from the soft component. By using the Einstein energy response and the best-fit model for the ASCA data of NGC4507 and IC5063, we further confirmed above scenario.

For NGC 1068 and NGC 1808, since no prominent hard components are found, we plotted only one circle.

For NGC 2110, the soft component is a small fraction of the whole 0.2-4 keV flux, hence unless the employed model represents the true spectral shape precisely, the apparent flux would largely scatter from an instrument to another instrument. Thus in mind, we plotted 3 circles for NGC 2110: the upper and lower are the same as those for NGC4507 etc. To mimic the flux determination employed with the Einstein data, we fit the corresponding soft band of the ASCA data with a single power law with the fixed photon index of 1.7, and plotted the obtained flux as the middle circle. Again we found no large variability for the soft component of NGC2110.

As we noted in the previous section, absolute flux comparison between different instruments may have larger error than the nominal statistical errors. This situation is more severe in the present soft X-rays, because the soft X-ray flux is largely coupled with the absorption and steep cutoff of the efficiency of Einstein and Rosat near the present energy band boundary (2 keV). Nevertheless we can safely conclude that no significant variability in the 0.2-4 keV band is found from any of the sample Seyfert 2s.

Since the hard components of NGC 4507, IC 5063, and NGC 1808 show variability, the absence of soft-band variability prefer either the scattered emission from extended region or the diffuse thermal emission as the origin of soft emission rather than the leaky absorber model.

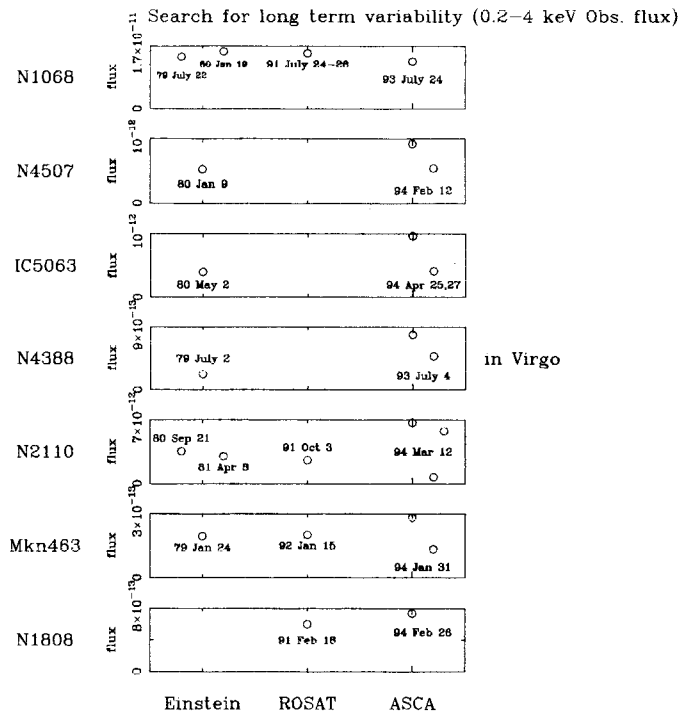


Figure 38: Search for long term variability (soft flux)

We plotted 0.2-4 keV band fluxes obtained with Einstein, ROSAT, and ASCA. Since ASCA covers energies above 0.5 keV, we extrapolated the best fit spectrum to 0.2 keV to obtain the flux. Significant variation was not found.

We show the photon indexes of the soft components of our targets in figure 39. We found no systematic difference of the slopes between the soft components of Seyfert 2s and the slopes of starburst galaxies (M82, NGC 253, and NGC 3079) at soft energies. Accordingly, we can not distinguish the starburst emission in active galaxies and the possible scattered emission of AGNs by using only the spectral slope.

For the origin of much steep soft component, we can reject the simple scattering model to be a unique origin because we can reasonably assume that the soft scattered X-rays have the same slope of the hard component. Although the spectral steepening is expected by the dust scattering, it can not account for a large fraction of soft X-rays due to limited grazing angle to give enough cross section of dust scattering.

Steep slopes are seen in NGC 1808, NGC 1667, NGC 1068, MKN 463, MKN 1210, PKS 1319-164, and NGC 7319 implying that the soft components may be partly due to diffuse thermal plasma such as supernova remnants in the case of starburst activity, and a nucleus-driven wind in the case of AGN activity (Raymond and Smith 1977[139]; Wilson et al 1992[205]).

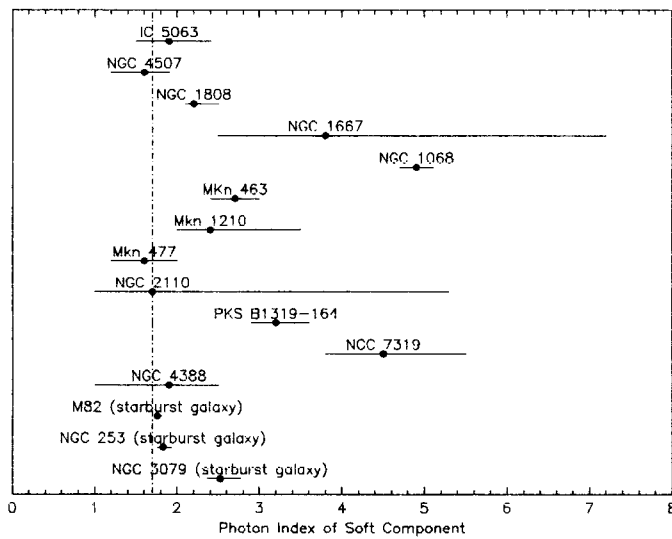


Figure 39: The photon index of soft component

The photon index of soft component and the 90 % error bar are plotted for each objects. Those were derived from a double power-law model. For NGC 1808, NGC 1667, M 82, NGC 253, and NGC 3079, the photon index plotted here are from fitting the 0.5-10 keV spectrum with a single power-law model.

### 5.2.2 Evaluation of non-AGN X-ray flux by using $L_{\text{FIR}}$ and $L_B$

Far infrared (here after FIR) luminosity is one of the indicators of the starburst activities (David et al. 1992[31]). We compare the FIR (40-120 $\mu\text{m}$ ) and the soft X-ray(0.5-2keV) luminosities in figure 40. The starburst galaxies, M82, NGC 253, and NGC 3079, are along a relation,  $L_{\text{FIR}}/L_X \sim 10^4$ .

Most of type 2 Seyferts are plotted around a linear relation,  $L_{\text{FIR}}/L_X \sim 10^3$ . The inferred X-ray emission due to starburst activity would be overestimated, because the FIR emission from nucleus torus in Seyfert galaxies could account for the significant fraction of the total FIR luminosity (Telesco et al 1984[166]). Nevertheless many Seyfert 2s have systematically larger emission than the inferred from FIR for possible starburst activity.

The  $L_{\text{FIR}}/L_X$  of two Seyfert 2s, NGC1808 and N1667 suggests the soft X-rays are solely attributable to the starburst activities.

Most of the soft X-rays from NGC 1068 are explained by starburst activities in terms of the spatial and spectral distribution (Wilson et al. 1992; Ueno et al 1994). Thus NGC 1068 may merely be one of the most deviated sources in the  $L_X/L_{\text{FIR}}$  of starburst activity (see the scatter around the relation in David et al 1992 [31]). Wilson et al (1992[205]) mentioned that the spatially extended flux of NGC 1068 obey the  $L_X/L_{\text{FIR}}$  relations showed by Griffis and Padovani (1990[55]) for IRAS galaxies and starburst/interacting galaxies.

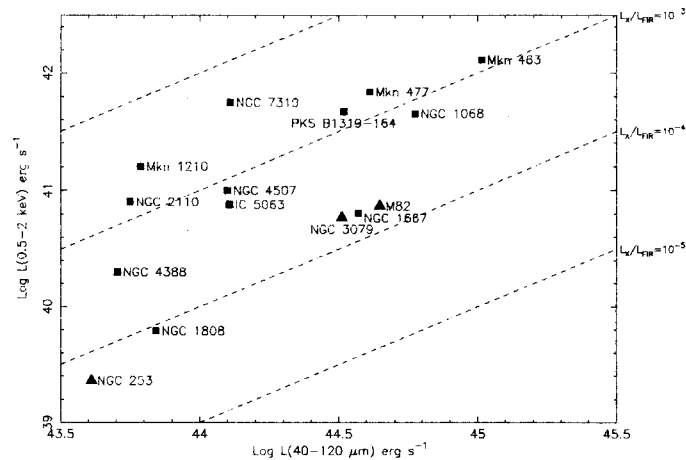


Figure 40:  $L_X(0.5-2 \text{ keV})$  vs.  $L_{\text{FIR}}(40-120\mu\text{m})$

$L_X(0.5-2)$  is the 0.5-2 keV band flux of the soft component.  $L_{\text{FIR}}(40-120\mu\text{m})$  is a far infrared luminosity calculated from FIR fluxes listed in "CATALOGED GALAXIES AND QUASARS OBSERVED IN THE IRAS SURVEY Version 2", using distances in Table 4.

Since the X-ray luminosity of spiral galaxies ranges from  $10^{38}$  to  $10^{41}$   $\text{erg s}^{-1}$ , it is still a possible origin of the soft component for IC5063, NGC4507, NGC4388 and NGC2110, whose soft luminosities are smaller than  $10^{41}$   $\text{erg s}^{-1}$ . For the luminous FIR sources such as starburst galaxies, the FIR luminosities are indeed correlated with the X-ray luminosities. However, The X-ray emission of normal galaxies is correlated not only with the FIR luminosity but also with the blue-band luminosity  $L_B$ , because a good fraction of the X-ray emission is due to a collection of individual bright sources, such as close binary stars with a compact companion, and supernova remnants.

Thus we have to check whether there is excess emission above the total non-AGN X-ray emission. In figure 41 we compare the observed luminosities of our targets with those inferred from the relation by David et al (1992[31]),  $L_X = 9.9 \times 10^{-5}L_B + 9.3 \times 10^{-5}L_{\text{FIR}}$ .

David et al found a strong correlation between the far-infrared and X-ray luminosities among the normal and starburst (NSB) galaxies with,  $L_X \propto L_{\text{FIR}}^{0.90-1.01}$  (90% confidence limits). They also shows the relation between the X-ray and blue luminosity of the NSB galaxies is also consistent with a linear relation,  $L_X \propto L_B^{1.03-1.18}$  (90% confidence limits) but exhibits increasing scatter with increasing  $L_B$ . The residuals in  $L_X$  around the best-fit relation are strongly correlated with the ratio  $L_{\text{FIR}}/L_B$  which is a measure of the current star formation rate. These correlation in the NSB sample can be understood through a

two-component model for the X-ray emission from spirals. One component consists of relatively old objects (Type I supernovae and low-mass X-ray binaries) and is proportional to  $L_B$ , while the second component comprise young objects (Type II supernovae, O star, and high-mass X-ray binaries) and is proportional to the far-infrared luminosity from active regions of star formation. The first component dominates in more quiescent galaxies, while the second component dominates in star burst activity.

In figure 41, we found the excess emission in the actually observed soft X-rays of Seyfert 2s. However, the relation used here have uncertainty with  $\Delta \log(L_X) \sim 1$  at full width. Thus we can not persist in the excess emission in IC5063, NGC4507, and NGC4388. In the other Seyfert 2s we found larger excess. If the excess is associated with the AGN, one problem is steepening of the spectral slope at the soft energies. As mentioned on the comparison of the soft slope, it is hard to reproduce the steepening (or soft excess) by the scattering. The steepening at low energies are also observed in type 1 Seyfert galaxies (Seyfert 1s) and quasars, but they are usually seen below the ASCA energy band. One possibility is thermal emission from a nucleus-driven wind (Raymond and Smith 1977[139]; Wilson et al 1992[205]) or photoionized plasma illuminated by the central source of the AGN.

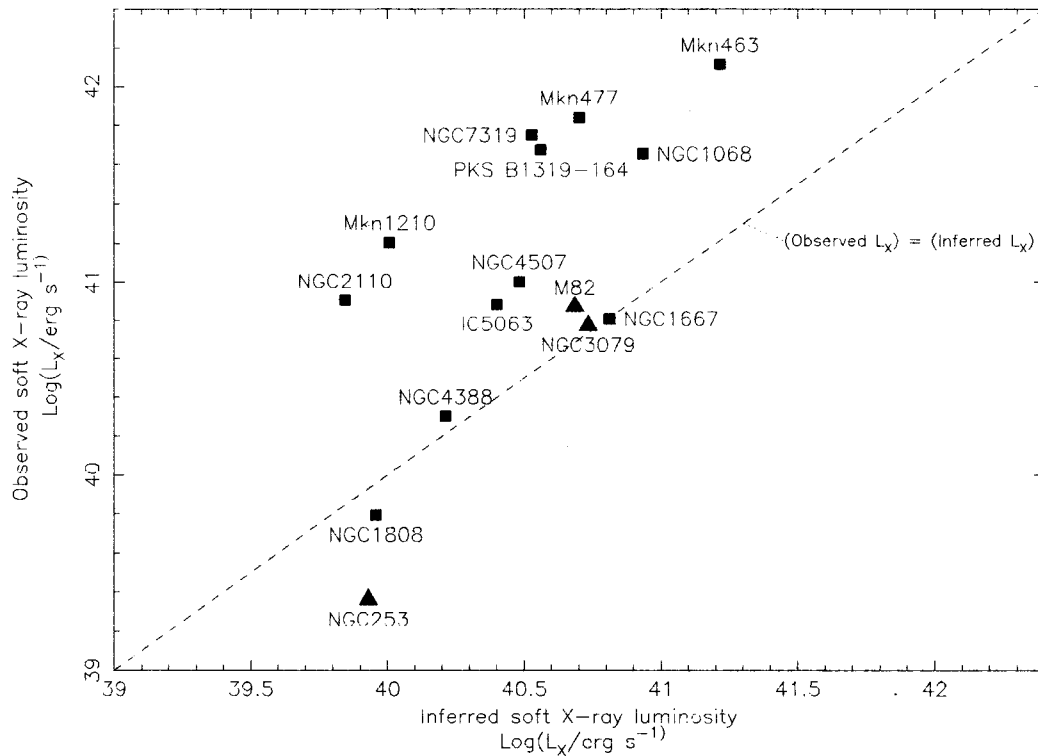


Figure 41: Observed  $\log(L_X)$  vs. inferred  $\log(L_X)$

Inferred  $\log(L_X)$  are given by the relation,  $L_X = 9.9 \times 10^{-5} L_B + 9.3 \times 10^{-5} L_{\text{FIR}}$ , which were presented by David et al (1992[31]) for normal and starburst galaxies. The soft X-ray emission from Seyfert 2 galaxies show excess emission above the inferred flux.

### 5.2.3 The flux ratio of the soft and hard component

To get the ratio of the soft to hard flux, we fit the the spectra with the slopes of the soft and hard components to be linked but allowed to change simultaneously. When the scattered emission from the hidden nucleus accounts for the total soft emission, the normalization ratio of the two components can be called the scattering efficiency. The fitted ratios are listed in the upper part of table 22.

The plausible origin of the soft X-ray emission is scattered X-rays for IC 5063, NGC 4507, Mkn1210, Mkn477, NGC 2110, and NGC 4388 in terms of the spectral slopes in the typical range for the hard component of Seyfert galaxies. However, 1319-164, NGC7319 and Mkn463 give steep slopes due to the steep soft spectra. The normalization ratio employed here largely depends on the photon index. Thus we fixed the slope to 1.7 and called the resultant ratio merely the ratio of the soft and hard component. The results are listed in

the lower part of table 22.

Table 22: Normalization ratios of the soft to hard components

	Photon index	$N_{Hhard}$ ( $10^{22} \text{ cm}^{-2}$ )	$N_{Hsoft}$ ( $10^{22} \text{ cm}^{-2}$ )	Soft/Hard (%)	reduced $\chi^2$ (dof)
IC 5063	1.82(1.67–1.97)	24.2(22.8–25.6)	<0.07	0.8(0.6–1.1)	1.11(173)
NGC 4507	1.70(1.69–1.71)	37.0(36.9–37.1)	<2e-4	0.6(0.5–0.8)	1.18(173)
Mkn 463	2.78(2.26–3.95)	24.1(16.5–37.5)	<0.32	4.8(1.3–10.6)	1.57(38)
Mkn 1210	2.23(1.87–2.62)	26.9(20.8–34.7)	<0.08	4.9(2.6–9.1)	0.91(93)
Mkn 477	1.50(1.20–1.79)	32.6(25.4–41.6)	<0.04	10.2(.60–17.3)	0.94(130)
NGC 2110	1.52(1.47–1.58)	3.26(3.07–3.46)	<0.17	4.8(3.9–5.9)	1.36(357)
PKS B1319-164	3.24(2.99–3.56)	63.0(58.1–68.9)	0.16(0.11–0.22)	0.5(0.3–0.8)	1.36(223)
NGC 7319	3.69(3.21–4.34)	65.6(54.6–80.3)	0.22(0.14–0.34)	0.4(0.2–0.9)	1.47(114)
NGC 4388	1.28(0.91–1.64)	33.7(29.1–38.4)	<0.05	2.2(1.1–3.8)	1.07(160)
IC 5063	1.7(fix)	23.3(22.4–24.2)	<0.05	1.0(0.9–1.1)	1.12(174)
NGC 4507	1.7(fix)	37.0(35.8–38.0)	<0.05	0.7(0.5–0.7)	1.18(174)
Mkn 463	1.7(fix)	31.4(17.3–60.2)	<0.04	18.6(8.6–35.7)	1.93(39)
Mkn 1210	1.7(fix)	27.7(20.4–37.4)	<0.03	10.8(7.8–14.9)	0.96(94)
Mkn 477	1.7(fix)	31.9(25.3–39.8)	<0.06	7.4(5.8–9.5)	0.94(131)
NGC 2110	1.7(fix)	3.82(3.68–3.98)	0.19(0.10–0.31)	5.1(4.1–6.5)	1.43(358)
PKS B1319-164	1.7(fix)	54.5(49.4–60.1)	<3e-3	5.5(4.7–6.4)	2.14(224)
NGC 7319	1.7(fix)	66.4(52.5–84.8)	<8e-3	5.9(3.9–8.7)	2.20(115)
NGC 4388	1.7(fix)	37.3(34.0–40.9)	<0.05	1.1(0.9–1.4)	1.09(161)

Note. — We fitted the spectra with a double power-law model with their photon indexes linked.

We listed the normalization ratio of the soft to hard components as Soft/Hard.

First we allow the slopes to change simultaneously, and listed the results in the upper part. Then we fixed the slopes at 1.7 and listed the normalization ratio in the lower part, which we call merely the ratio of the soft and hard component hereafter.

The ratios of the soft to hard components are about 1 % for IC 5063, NGC 4507, and NGC 4388. The other sources have larger ratios. We plotted the normalization ratio of the soft to hard components against the photon indexes in figure 42. We found that the sources with steep soft components tend to have the large ratios of the soft to hard components, implying that thermal emission could account for the large soft emission of these sources. As mentioned in the individual section of NGC 7319, at least 2/3 of the soft emission of the extracted spectra does not associate with NGC 7319. Thus the real ratio of the soft

and hard components reduces below 2%, comparable to those of NGC 5063, NGC 4507, and NGC 4388.

One remarkable point is that all polarized broad line (PBL) sources in our sample have the large ratios of the soft to hard components. Iwasawa et al (1994[72]) showed another PBL source, Mkn 3, also have the large ratio ( 3% in the BBXRT observation; 11% in the period of the ASCA observation). Kay (1994[76]) performed blue spectropolarimetries for NGC 4388, NGC 2110, NGC 7319, and PKS B1319-164. They have no significant evidence of PBLs. He reported the continuum polarization of 7.4% in PKS B1319-164. Although there are difficulties in measurements of the weak PBLs, our result gives a hint that the X-ray emitting or scattering region seen in the soft component has a close relation with that for optical polarized broad lines.

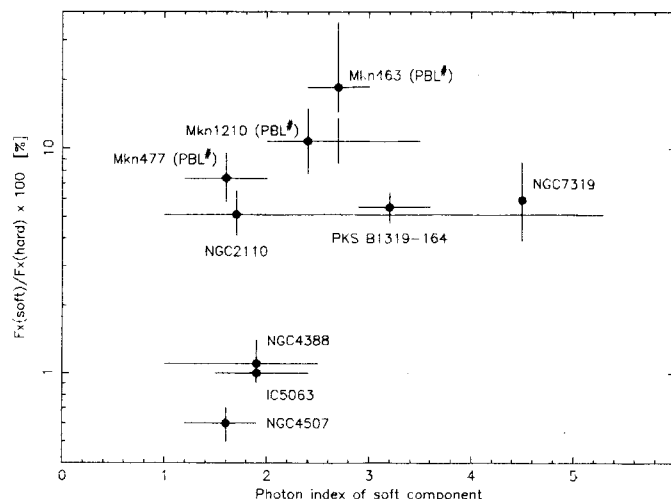


Figure 42:  $F_X(\text{soft})/F_X(\text{hard})$  vs. Photon Index(soft)

$F_X(\text{soft})/F_X(\text{hard})$  is the normalization ratio of the soft to hard components for a double power-law model, in which both the photon indexes are fixed to 1.7.

#: Optical polarized broad lines (PBL) have been observed in the source.

Since the steepness of the soft spectra rejects the scattering model as the unique origin of the soft emission, we have been concerned with thermal emission from hot plasma seen in early type galaxies. In figure 42 only two sources, IC 5063 and NGC 2110, are classified in early-type galaxies, and show no significant soft excess compared with the other sources. Thus, thermal emission from the hot plasma is rejected for a possible origin of the soft emission in our sample.

For the sources which have the steep soft components, the ratio, Soft/Hard, in table 22 does not give the good measures for true scattering efficiency, because they may have a steep extra emission above scattered emission. We add the RS model for the extra emission and listed the results in table 23. The scattering efficiencies distributes in the range of about 1–10 %.

Note the scattered fractions  $f_{\text{scat}}$ s given here are still the upper limit of the true value, because of a possibility that the soft emission include the non-scattered emission with the similar photon index (e.g. the soft component of M82 and NGC253).

Table 23: Scattering efficiency

	$f_{\text{scat}}\%$	KT(keV) of the RS	metal abundance (solar) of the RS model	reduced $\chi^2$ (dof)
IC 5063	1.0(0.9–1.1)	—	—	1.12(174)
NGC 4507	0.6(0.5–0.7)	—	—	1.18(174)
Mkn 463	0 (<12.1)	1.0(0.3–1.4)	0.04(<0.45)	1.51(37)
Mkn 1210	8.5(1.7–12.8)	0.8(0.2–1.2)	0.2(<5)	0.86(92)
Mkn 477	7.3(<8.8)	0.7(<64)	2.1(<5)	0.95(129)
NGC 2110	5.1(4.1–6.5)	—	—	1.43(358)
PKS B1319-164	2.7(1.9–3.6)	0.8(0.7–0.9)	0.13(0.07–0.26)	1.28(222)
NGC 7319	3.0(1.6–4.9)	0.8(0.7–0.9)	0.19(0.09–0.87)	1.05(113)
NGC 4388	1.1(0.9–1.4)	—	—	1.09(161)

#### 5.2.4 Search for fluorescent lines

A photoionized plasma of high ionization emits recombination lines. We can not distinguish the center energies and profiles of recombination lines from those of thermal plasma with existing instruments. One feasible method to distinguish the two plasmas is a comparison of temperatures determined from lines and the continuum. The elements in photoionized plasma are in higher ionization stages than those in thermal (collisional ionized) plasma in the same continuum temperature (electron temperature). However, the comparison is hard with limited statistics.

On the other hand, fluorescence lines often provide good evidence for photoionized plasma. The fluorescent lines from neutral elements are resolved from recombination lines with the energy resolution of ASCA. Of course, fluorescent lines can be emitted from “dense” matter illuminated by “high energy electrons” seen in X-ray generators in laboratories or

molecular cloud illuminated cosmic rays. However, in the situation around AGN, some amount of flux in fluorescent lines is accepted for the evidence for photoionized plasma. Indeed the 6.4 keV iron fluorescent lines have been observed in many AGNs.

We search fluorescent lines in the soft components of IC5063 and NGC4507, since these sources do not have extra steep continuum in the soft components. It is useful to measure the strength of line emissions by their equivalent widths (EWs). If scattered X-rays from the central source dominate the observed continuum, a straightforward calculation gives the EW of the fluorescent line from the scattering region in the following formula,

$$EW = \frac{\eta \int_{E_K - \text{edge}}^{\infty} dF/dE(E) \sigma_{\text{ph}}(E) A_b dE}{dF/dE(E_{\text{line}}) \sigma_{\text{Th}}} \quad (3)$$

where we assumed each X-ray photon can be scattered only once in the scattering region for simplicity. The terms,  $\sigma_{\text{Th}}$  and  $\sigma_{\text{ph}}(E)$  are the cross section of Thomson scattering and of photoelectric absorption, respectively.  $A_b$  is the abundance of each element (i.e. the number ratio of the relevant elements to hydrogen). The fluorescence yield of  $K\alpha$  photons per recombination is denoted by  $\eta$ . When the incident power-law spectrum  $F(E)$  has the photon index of 1.8, this formula gives EWs of, respectively, 140, 214, 309 and 1530 eV for Mg, Si, S and Fe, while the expected center energies of the emission lines come, respectively, at 1.25, 1.74, 2.31 and 6.4 keV, assuming the elements are neutral (i.e. not ionized).

In fact, such lines of light elements are detected in Cen A with ASCA (Sugizaki et al 1997[165]), and a strong Fe K line has been observed in NGC 1068. We listed the upper limits of the EWs for the soft component of IC5063 and NGC4507 in table 24.

The upper limits are smaller than expected values, suggesting that these elements are either depleted or highly ionized in the photoionized plasma. Since Fe K lines in AGNs generally show no depletion, the lack of the light elements is unpalusible. Thus the scattering matter in IC5063 and NGC4507 would be highly ionized.

Table 24: Upper limits of fluorescent-line emission in the soft component

	Expected center energy(keV)	Expected EW(eV)	ASCA EW(eV) IC5063	ASCA EW(eV) NGC4507
Mg	1.25	140	<53	<25
Si	1.74	214	<237	<79
S	2.31	309	<183	<160

### 5.3 Distribution of absorption column

#### 5.3.1 All polarized broad line sources show heavy absorption

We show the distribution of the absorption column density in figure 43. Since ASCA can not measure column densities larger than  $10^{24} \text{ cm}^{-2}$ , the targets with  $N_{\text{H}} > 10^{24} \text{ cm}^{-2}$  are included at the  $\log N_{\text{H}} = 24 - 24.5$  band. We separately show the [OIII]-bright sources, Narrow Emission Line Galaxies(NELG), and the others. Our results indicate that Seyfert 2s with polarized broad line have heavily absorbed X-ray nuclei as well as broad-line regions.

It is difficult to derive column density distribution of non-biased sample, especially those for heavily absorbed sources, because large absorption column can only be determined by X-rays, hence are inevitably biased to the X-ray selected samples.

One remarkable result is concentration of the column densities around  $10^{23} \text{ cm}^{-2}$  for the [OIII] sample. There are only a few objects with  $N_{\text{H}} > 10^{24} \text{ cm}^{-2}$ . However, if extremely absorbed sources has small luminosity of [OIII] line, we would underestimate the number of sources with  $N_{\text{H}} > 10^{24} \text{ cm}^{-2}$ . Thus in mind, we compare the [OIII] luminosities between the [OIII] sample and the other completely blocked sources and found no systematic difference.

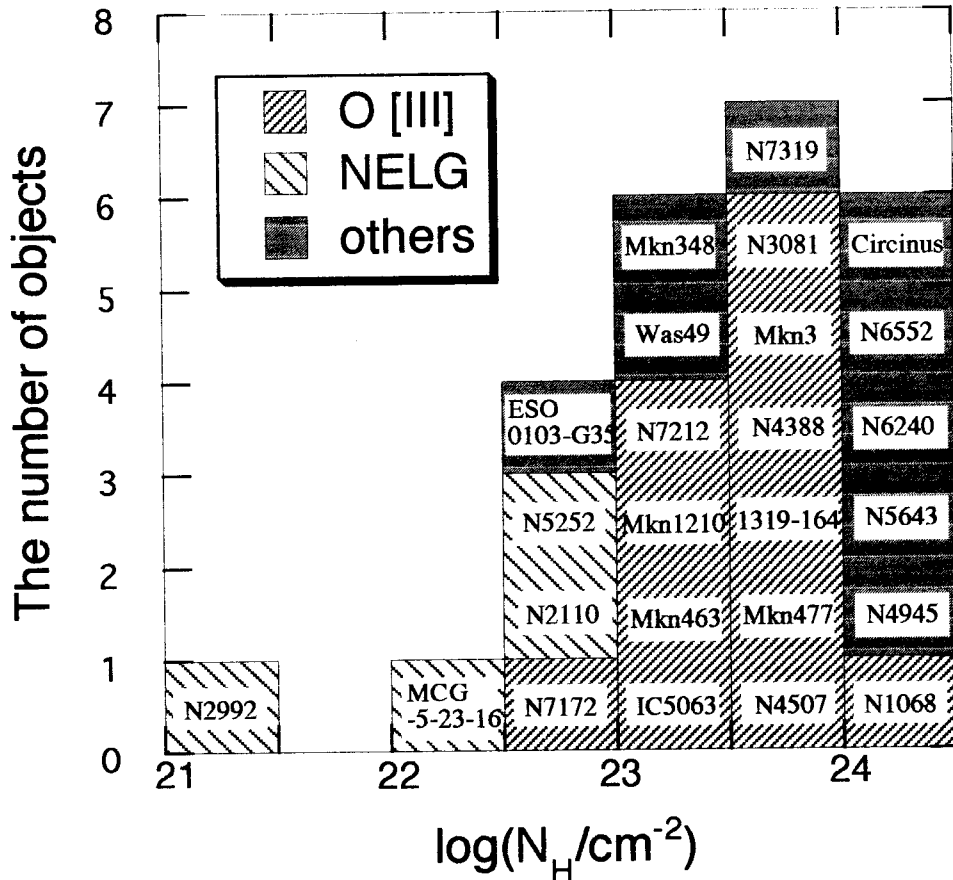


Figure 43: The distribution of absorption column thickness

The targets with  $N_H > 10^{24}$  cm $^{-2}$  are located at  $\log N_H = 24.0 - 24.5$ . In addition to the column densities for our sample, we show those for NGC 4945 (Iwasawa 1994[70]), NGC 5643 (Awaki, Matsuoka 1996[16]), NGC 6240 (Nakagawa et al. 1997[117]), NGC 6552 (Fukazawa et al. 1994[50]), Circinus galaxies (Matt et al. 1996[101]), Mkn 3 (Iwasawa et al. 1994[72]), NGC 3081 (Awaki, Griffiths 1996[12]), Was 49 (Ueno et al. 1997[178]), Mkn 348 (Weaver, Awaki 1996[193]), NGC 7172 (Ryde et al. 1997[150]), NGC 5252 (Cappi et al. 1996[24]), ESO 0103-G35 (from the ASCA archive), MCG-5-23-16 (Weaver et al. 1997[196]), and NGC 2992 (Weaver et al. 1996[195]). We separately exhibit the [OIII]-bright sources, Narrow Emission Line Galaxies (NELG), and the others.

### 5.3.2 Peak in $N_H$ distribution and the cosmic X-ray background

It is now clear that large fraction of the cosmic X-ray background (CXB) comes from the integrated emission of AGNs. One serious problem was that the X-ray spectrum of the CXB is different from that of the typical AGNs. The X-ray spectra of Seyfert 1s are

approximated by a power-law model of mean index of 1.7, which is significantly steeper than that of the CXB of about 1.4. If we subtract the mean X-ray spectrum of AGNs from the CXB spectrum, we found that residual spectrum has a low energy turn-off, which is similar to those of Seyfert 2s (Awaki 1991 [7]). Awaki pointed out that if total number of type 2 AGNs is two or three times larger than that of type 1s, then the integrated spectrum become similar to the spectrum of the CXB (Awaki 1991 [7]).

Comastri et al (1995 [28]) fit the distribution of absorbing column density of Seyfert 2s to explain the wide-band spectral shape of the CXB. They divided the absorbed objects ( $N_{\text{H}} > 10^{21} \text{ cm}^{-2}$ ) into four  $N_{\text{H}}$  classes, one decade in  $N_{\text{H}}$  wide, up to  $N_{\text{H}} = 10^{25} \text{ cm}^{-2}$ . They pointed out that if the number density of objects in the four  $N_{\text{H}}$  classes is 0.35, 1.10, 2.30, 1.65, then the spectral shape of the CXB is explained in the 5-100 keV band within two sigma from all the available data points.

The distribution of absorbing column density of the model well matches with our results especially on the peak at  $10^{23.5} \text{ cm}^{-2}$ .

Awaki (1991 [7]) and Comastri et al (1995 [28]) numerically give that the number density of Seyfert 2s larger than Seyfert 1s by the comparison of spectra between Seyferts and the CXB. Our observational results give no information on the ratio of number densities Seyfert 1s and 2s. The unbiased [OIII] sample of both types of Seyferts would make it possible to give an answer. Inoue(1997 [68]) have used far-infrared luminosities instead of O[III] and suggest the local number density of Seyfert 2s is larger than Seyfert 1s.

### 5.3.3 Spatial distribution of absorbing material

If we assume the all Seyfert galaxies have similar spatial distribution of material around the X-ray nucleus, the observed distribution of absorbing column can not be explained by a simple model based on only a uniform-density torus. For example, we assumed a simple configuration of absorbing torus as showed in figure 44, and calculated the expected distribution of column (figure 45). This model has a sharp peak in the expected column. To explain the observed number distribution, we need more complicated absorber, for example, optically thicker torus inside than outside.

The outside-thin option could be attributed to the envelope of the torus, while the inside-thick absorber can be a torus itself or an accretion disk (e.g., an inner torus in Maiolino and Rieke 1995[94]; the dual absorber in our results of NGC 2110).

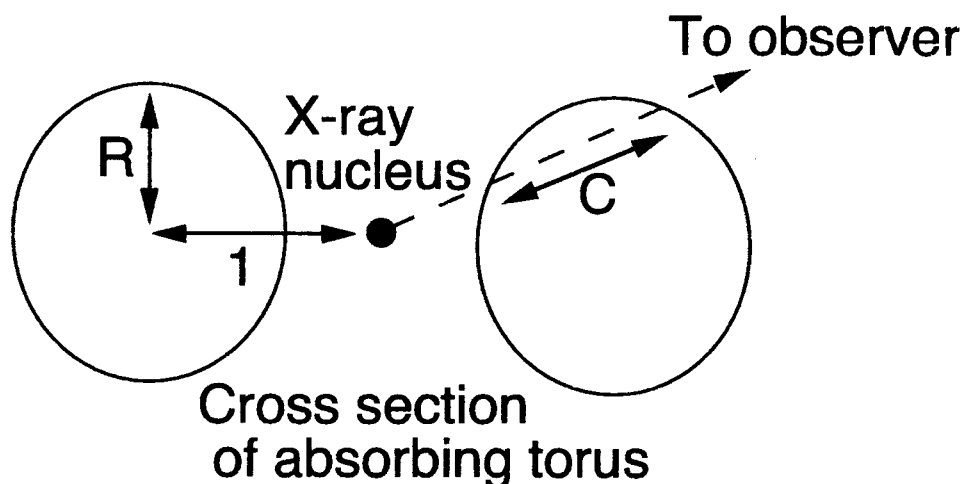


Figure 44: The configuration of a simple torus model

The  $R$ ,  $C$ ,  $1$  have the dimension of length.

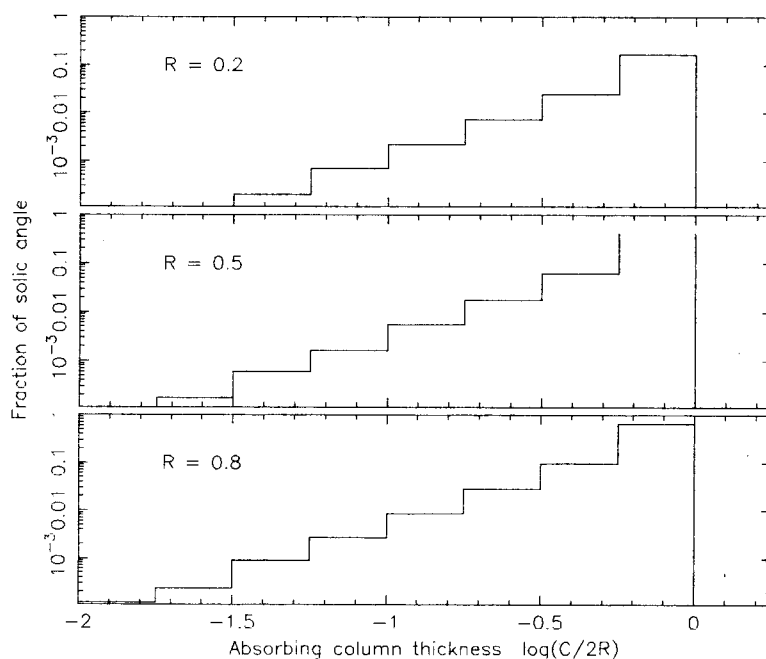


Figure 45: The expected distribution of column density for a simple torus model  
Fractions of solid angle are given as a function of column density.

### 5.3.4 The depth of Fe K edge

We compare the hydrogen equivalent column densities with iron column densities. The hydrogen column densities are determined from the low energy cutoffs of the hard components. We get the iron column densities by fitting the hard component with a power-law

and the iron K-edge at 7.11 keV (table 25). The hydrogen and iron column densities are shown in figure 46 and are roughly consistent with the cosmic abundance: the number ratio  $\text{Fe}/\text{H} = 4.68 \times 10^{-5}$ , except for NGC2110. The discrepancy seen in NGC 2110 is explained by dual absorber ( see the discussion for NGC2110).

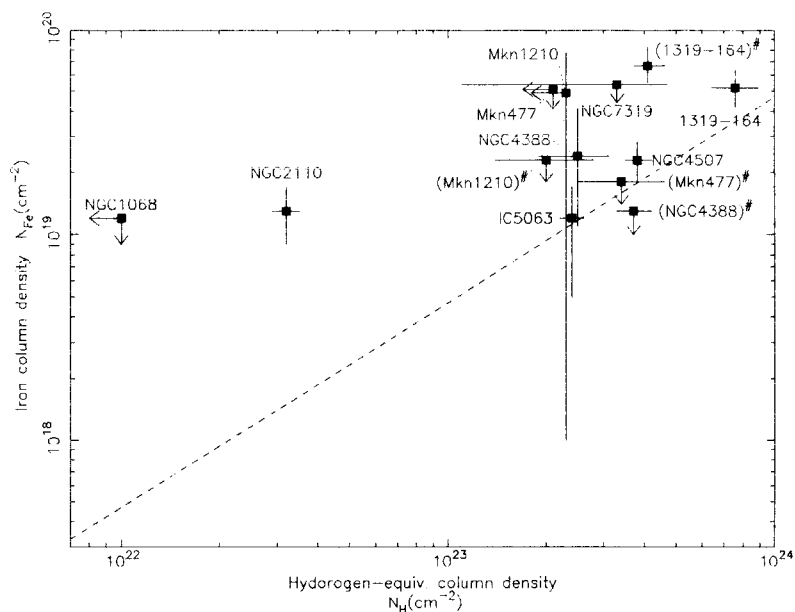
Table 25: Depths of Fe K edge

Source name	Optical depth $\tau_{\text{Fe}}$	Iron column density $N_{\text{Fe}}(10^{19}\text{cm}^{-2})$	Hydrogen-equivalent column density* $N_{\text{H}}(10^{23}\text{cm}^{-2})$
IC 5063	0.34(0.15–0.50)	1.2(0.5–1.7)	2.4(2.2–2.6)
NGC 4507	0.64(0.50–0.79)	2.3(1.8–2.8)	3.8(3.5–4.2)
NGC 1068	< 0.34	< 1.2	< 0.10
Mkn 1210	1.39(0.05–2.17)	4.9(0.1–7.7)	< 2.3
(Mkn 1210)#	< 0.64	< 2.3	2.0(1.4–2.8)
Mkn 477	< 1.44	< 5.1	< 2.1
(Mkn 477)#	< 0.50	< 1.8	3.4(2.5–4.6)
NGC 2110	0.36(0.25–0.47)	1.3(0.9–1.7)	0.32(0.29–0.35)
PKS B1319-164	1.47(1.19–1.82)	5.2(4.2–6.4)	7.6(6.4–8.9)
(PKS B1319-164)#	1.90(1.57-2.34)	6.7(5.5–8.3)	4.1(3.7–4.6)
NGC 7319	<1.54	< 5.4	3.3(1.1–4.7)
NGC 4388	0.68(0.32–1.17)	2.4(1.1–4.1)	2.5(1.9–3.1)
(NGC 4388)#	< 0.37	< 1.3	3.7(3.3–4.2)

Note: The edge energy was fixed at 7.11 keV at the rest frame of each source. We calculate the iron column density from the optical depth by using  $N_{\text{Fe}} = \tau_{\text{Fe}}/\sigma_{\text{FeK edge}}$ , where  $\sigma_{\text{FeK edge}}$  is the cross section of photoelectric absorption at the edge,  $2.84 \times 10^{-20}\text{cm}^{-2}$ .

#: In the case of the photon index of the hard component fixed at 1.7.

\*: From table 19 (a double power-law model) except for NGC 1068. For NGC 1068 we use the upper limit of  $N_{\text{H}} < 0.10 \times 10^{23}\text{cm}^{-2}$  obtained by using the thermal plasma model for the soft component, which is described in the individual source section.

Figure 46:  $N_{\text{Fe}}$  vs.  $N_{\text{H}}$ 

The hydrogen column densities  $N_{\text{H}}$  and the iron column densities  $N_{\text{Fe}}$  are from table 25. The dashed lines show a relation for cosmic metal abundance,  $N_{\text{Fe}}/N_{\text{H}}=4.68 \times 10^{-5}$ .

#: In the case of the photon index of the hard component fixed at 1.7.

## 5.4 Fe K line

### 5.4.1 $\log N_{\text{H}}$ and equivalent width of iron line

Except Mkn463, NGC 1808, and NGC 1667, our targets show Fe K lines, whose center energies are consistent with that of neutral iron. Figure 47 shows the correlation of the equivalent widths (EWs) and the hydrogen equivalent column density ( $N_{\text{H}}$ ) inferred from the low energy cutoffs. NGC 1068 also have a broad feature around the narrow Fe K line, which is attributable to the emission lines from highly ionized iron. Here we consider only the narrow lines for comparisons to the other Seyfert 2s. NGC 1068 has the EW and  $N_{\text{H}}$  consistent with the scattering model. The other sources are explained by the Fe K emission from absorbing matter surrounding the central source except NGC 2110. NGC2110 needs to be partially covered by absorber with  $N_{\text{H}} \sim 10^{23} \text{H atom cm}^{-2}$ , much thicker than that inferred from the low energy cut-off (Hayashi et al 1996[60]). The relatively small EWs of IC 5063 and NGC 4507 implies that the absorbers are subtending in small angles.

In many Seyfert 1s, complex Fe K features have been reported, and are attributed to the relativistic motion of possible accretion disks. On the other hand, Seyfert 2s in our sample do not need the accretion disk as the Fe K emitter, since Fe K features of our targets are well fitted with a narrow line. The absence of the relativistic features can be explained by the heavy absorption due to the accretion disk and the largely extended torus.

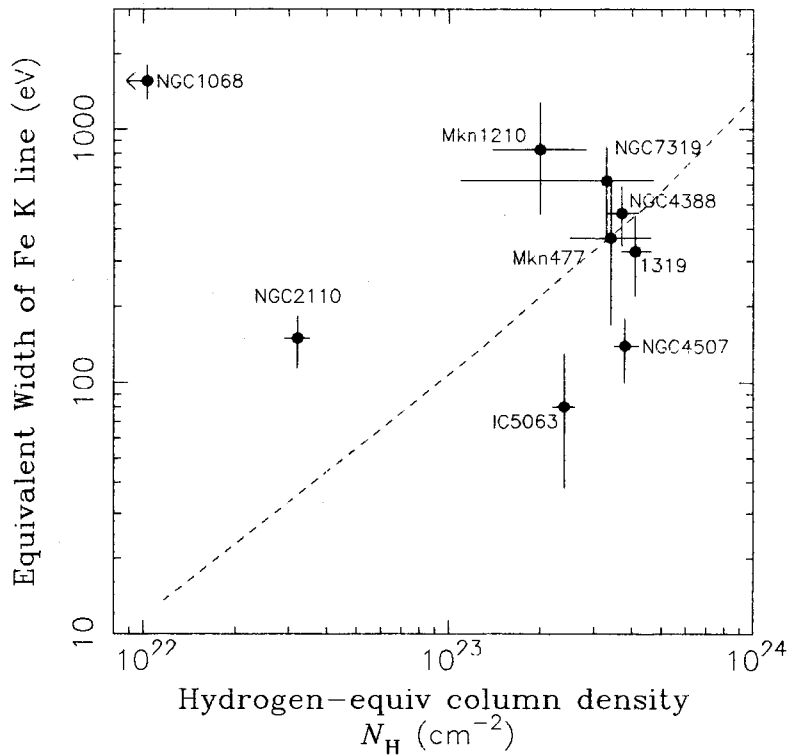


Figure 47: *EW* of Fe K line vs. Absorption column

The dashed lines show the relation between the matter thickness  $N_{\text{H}}$  and the Fe line Equivalent width in the simple model of isotropic radiation and uniform distributed matter (Inoue 1985[66]).

#### 5.4.2 Emission line from warm iron

Two galaxies, NGC 1068 and NGC 6240 (Nakagawa et al. 1997 [117]), show He-like and H-like Fe  $K\alpha$  in their X-ray spectra, as well as cold Fe  $K\alpha$ . Figure 48 shows a close view of the X-ray spectrum for NGC 1068. The emission lines from He-like and H-like iron were clearly detected. To produce H-like iron, ionization parameters ( $\xi = L/nr^2$ ) must have values as large as 1000, and the temperature of the photoionized plasma is about  $10^6$  K (Kallman

and McCray 1982 [75]). Since we also detected cold iron, there may be a two-temperature plasma. Marshall et al. (1993 [96]) estimated the temperature of the plasma, and found to be  $T = 2 \times 10^5$  K for the warm component and  $T = 4 \times 10^6$  K for the hot component.

If this hot and warm plasmas are common for Seyfert 2s, scattered X-ray from the plasma contributes to the soft X-rays detected with ASCA. In fact, we found that the soft component in several galaxies arises from AGN activity.

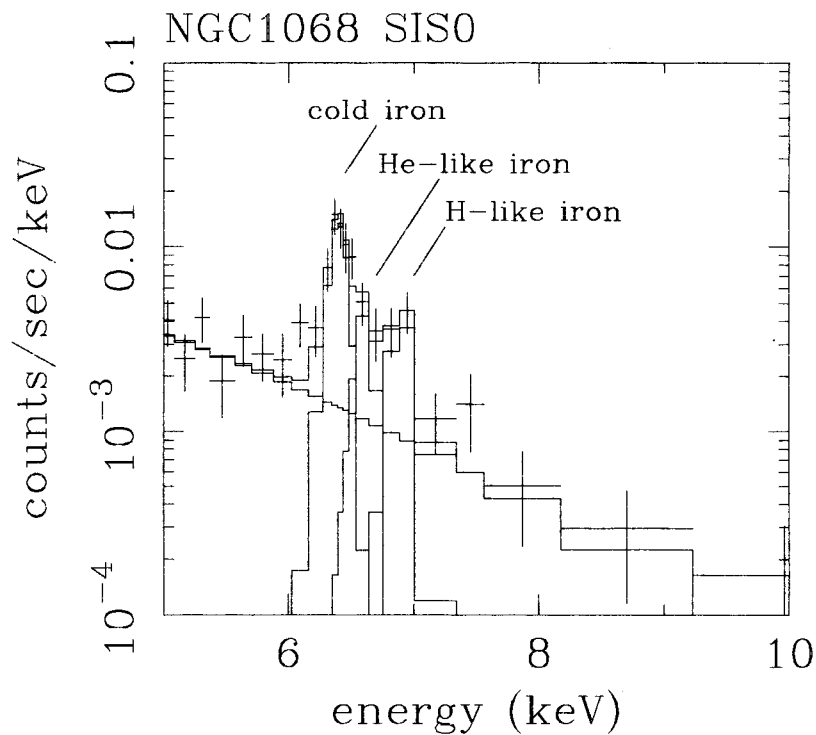


Figure 48: Fe line emission from NGC1068

This spectrum was obtained with SIS0.

## 6 Conclusions

We observed several Seyfert 2 galaxies with the SISs and GISs aboard the ASCA satellite. The wide band spectra ranging from 0.5 to 10 keV were obtained for the first time. We also obtained the ASCA spectra of starburst galaxies for comparison of the soft spectra with those found in Seyfert 2 galaxies.

The majority of the Seyfert 2 galaxies show heavily absorbed spectra with Fe K lines, which supports the unified Seyfert theory developed with previous instruments. ASCA provides new data sets of hard X-rays with reduced fluxes for several Seyfert 2s.

Variabilities of the hard X-rays with time scales of  $\sim 5$  year are found which support that the emitting region is compact. The complex Fe K feature found in NGC1068 indicates the presence of photoionized plasma of high ionization stages. This also confirms the unified model of Seyfert galaxies.

In addition to the hard X-rays, we found soft X-rays and determined that spectra more precisely than any previous observations. Seyfert 2s with strong soft emission tend to have steeper spectral slope. Therefore the previous results of the scattering efficiency by comparisons between the soft and hard X-ray fluxes would be overestimated.

The soft flux in Seyfert 2s generally exceeds (the soft excess) the integrated flux from individual sources in the host galaxies, which is estimated by the empirical  $L_X - L_{\text{FIR}}$  relation found in spiral and starburst galaxies. Thus we suggest two possibilities; either significant fraction of soft X-rays is not attributable to starburst activities in Seyfert 2 galaxies, or the  $L_X - L_{\text{FIR}}$  relation for starburst regions in Seyfert 2s may be different from that found in normal starburst galaxies with no Seyfert activity. For the former case, most plausible origin is the scattering flux from AGN, although host galaxy origin such as hot gas seen in early type galaxies may not be excluded. NGC1068 would be an unique case belonging the latter case. For most Seyfert 2s in our sample, however, the spectral quality is not yet sufficient to give conclusive results.

In the small fraction of Seyfert 2s, on the other hand, we found no significant soft excess, which means the integration of individual sources can well account the most of the soft X-rays.

**A The O[III]  $\lambda$ 5007 flux of Seyfert 2 galaxies**Table 26: O[III]  $\lambda$ 5007 flux of Seyfert 2 galaxies

Source Name	[OIII] flux*	Reference	ASCA observation	Remark
NGC 1068	2.00e-11	2	yes	
Mkn 3	3.47e-12	2	yes	
Mkn 573	1.58e-12	2		
Mkn 477	1.51e-12	2	yes	
1319-164	1.5e-12	3	yes	
NGC 3081	1.26e-12	2	yes	
NGC 4507	1.10e-12	2	yes	
Mkn 1210	1e-12	10	yes	
IC 5063	9.33e-13	2	yes	
NGC 2992	9.12e-13	2	yes	
NGC 1386	7.94e-13	2	yes	
NGC 5643	7.94e-13	2	yes	
Mkn 463	7.24e-13	2	yes	
NGC 7212	7.08e-13	2	yes	
Mkn 34	6.76e-13	2		
Mkn 78	6.61e-13	2		
Mkn 1	6.03e-13	2	yes	NGC 449
NGC 5252	5.9e-13	5	yes	
Mkn 533	4.90e-13	2		NGC 7674
NGC 4388	4.79e-13	2	yes	
TOL 1351-375	4.79e-13	2		
1246-111	4.6e-13	3		
NGC 5506	4.47e-13	2		
Mkn 348	4.17e-13	2	yes	
TOL 0109-383	4.17e-13	2		

Table 26: — Continued

Source Name	[OIII] flux*	Reference	ASCA observation	Remark
NGC 7582	3.47e-13	2	yes	Composition, Sy2(NED)
NGC 4939	3.4e-13	1		
Mkn 1388	2.9e-13	3		
Mkn 270	2.69e-13	2		
NGC 526A	2.69e-13	2	yes	
1105-115	2.4e-13	3		
Mkn 1066	2.40e-13	2		
Mkn 273	2.40e-13	2	yes	
Was 49	2.36e-13	4	yes	
MCG-5-23-16	2.29e-13	2	yes	
Mkn 1157	2.29e-13	2		
NGC 6552	2.2e-13	8	yes	
Mkn 1073	2.19e-13	2		
NGC 5135	2.19e-13	2	yes	
UM 16	2.1e-13	3		
NGC 5728	1.95e-13	2		
NGC 6890	1.91e-13	2		
Mkn 176	1.86e-13	2		
Mkn 612	1.82e-13	2		
TOL 1238-364	1.82e-13	2		
NGC 2110	1.70e-13	2	yes	
1548-037	1.6e-13	3		
NGC 1320	1.41e-13	2		
NGC 4074	1.3e-13	3		
Fairall 188	1.29e-13	2		

Table 26: — Continued

Source Name	[OIII] flux*	Reference	ASCA observation	Remark
NGC 1358	1.29e-13	2		
Mkn 198	1.26e-13	2		
Mkn 917	1.1e-13	3		
NGC 4968	1.00e-13	2		
1304-234	9.8e-14	3		
Mkn 403	9.4e-14	3		
NGC 5929	9.33e-14	2		
Circinus galaxy	8.3e-14	7	yes	1.95e-11(Extention corrected)
1331-231	8.2e-14	3		
NGC 7319	7.8e-14	3	yes	
Mkn 686	7.2e-14	3		
Mkn 609	7.08e-14	2		
Mkn 268	6.76e-14	2		
Mkn 883	6.76e-14	2		
NGC 1667	6.76e-14	2	yes	
NGC 7314	6.7e-14	1		Sy1, Sy1.9(NED)
Mkn 417	6.6e-14	3		
NGC 6221	6.17e-14	2		
NGC 7314	6.17e-14	2		
Mkn 1457	5.9e-14	3		
Mkn 1058	5.62e-14	2		
NGC 5427	5.5e-14	1		
NGC 3281	5.50e-14	2		
UM 246	5.4e-14	3		
1524+007	4.6e-14	3		

Table 26: — Continued

Source Name	[OIII] flux*	Reference	ASCA observation	Remark
NGC 1144	4.3e-14	3		
0450-032	4.0e-14	3		
Mkn 622	3.98e-14	2		
NGC 1410	3.8e-14	3		
NGC 6221	3.6e-14	1		Composite, Sy2(NED)
NGC 1672	3.6e-14	1	yes	
NGC 7743	3.4e-14	1		Weak Sy2, Sy2(NED)
Mkn 955	3.4e-14	3		
Mkn 266	3.24e-14	2		
NGC 4922	3.1e-14	3		
NGC 3185	3.09e-14	2		
Mkn 993	3.0e-14	3		
NGC 4501	2.8e-14	1		
NGC 6240	2.6e-14	6	yes	
NGC 5273	2.19e-14	2		
NGC 1433	2.1e-14	1		
TOL 1028-301	2.00e-14	2		
NGC 613	1.7e-14	1		Composite, Sy1 or 2?
NGC 6810	1.7e-14	1		HII, Sy2(NED)
NGC 1808	1.4e-14	1	yes	
1329+022	1.4e-14	3		
NGC 6300	1.4e-14	1		
NGC 5128	1.2e-14	1		Type N, Sy2(NED)
Mkn 938	1.1e-14	3		
NGC 1241	1.0e-14	3		

Table 26: — Continued

Source Name	[OIII] flux*	Reference	ASCA observation	Remark
1423-116	8.6e-15	3		
0438-084	7.7e-15	3		
NGC 5005	7.5e-15	3	yes	
Mkn 522	7.5e-15	3		
1305-241	6.5e-15	3		
Mkn 957	3.2e-15	3		
NGC 4945		9	yes	No information on O[III]
Mkn 308		3		No information on O[III]
IC 4870		3		No information on O[III]
ESO 103-G35		2	yes	No information on O[III]
ESO 32-G2		2		No information on O[III]
NGC 5674		2		No information on O[III]
NGC 7172		2	yes	No information on O[III]
NGC 7496		2		No information on O[III]

Note.

\*: The unit of [OIII] $\lambda$ 5007 is  $\text{erg s}^{-1}\text{cm}^{-2}$ .

For a part of the sources, the digit numbers for the [OIII] flux are limited by those in referred papers.

#### References

1. Véron-Cetty, M.-P., Véron, P. 1986, A&AS, 66, 335
2. Mulchaey, J.S., Koratkar, A., Ward, M.J., Wilson, A.S., Whittle, M., Antonucci, R.R.J., Kinney, A.L., Hurt, T. 1994, ApJ, 436, 586
3. Dahari, O., De Robertis, M.M. 1988, ApJS, 67, 249
4. Moran, E.C., Halpen, J.P., Bothun, G.D., Becker, R.H. 1992, AJ, 104, 990
5. Tadhunter, C., Tsvetanov, Z. 1989, Nature, 341, 422

6. Fosbury, R.A.E., Wall, J.V. 1979, MNRAS, 189, 79
7. Olivia, E., Salvati, M., Moorwood, A.F.M., Marconi, A. 1994, 288, 457
8. Véron, P. 1996, private communication
9. Maiolino, R., Rieke, G.H. 1995, 454, 95
10. estimated from Tran, H.D., Miller, J.S., Kay, L.E. 1992, ApJ, 397, 452

## B Ionization parameter

The ionization parameter is a ratio of ionizing photon density to particle density. This parameter is derived from an equation on two successive ionization states, denoted in general as  $N$  and  $N^+$ , in a photoionized plasma at ionization equilibrium. For simplicity, suppose that we are dealing with hydrogen,  $N$  would be the density of neutral hydrogen atoms (ground or excited states) and  $N^+$  the density of protons. In a equilibrium, the number of recombinations per unit time is equal to that of ionizations per unit time, hence given as,  $N^+ N_e \times \overline{\sigma_r v} = N \int_{\nu_0}^{\infty} 4\pi J_{\nu} a_{\nu} (h\nu)^{-1} d\nu$ , where  $\sigma_r$  and  $a_{\nu}$  are the recombination cross section and the absorption coefficient for ionization, both in units of  $\text{cm}^2$  per photons.

We express the threshold energy for photons to ionize the atom to be  $\nu_0$ . The term  $4\pi J_{\nu} a_{\nu} / h\nu$  is the number of photons impinging in the unit volume containing  $N$  within a unit time, hence has a unit of photons number  $\text{cm}^{-2} \text{s}^{-1}$ ; this term represent the photon flux, hence. For a simple geometry where the continuum source is localized at a distance  $d$  from the gas, we obtain  $J_{\nu} \propto L_{\nu} d^{-2}$ . Accordingly, we obtain the relation  $N^+ / N \propto L_{\nu} / N_e d^2$ . The right term represents the ratio of photon flux to matter density, and is called the ionization parameter. This parameter directly controls the ratio  $N^+ / N$ . Ionization ratio depends on distance to the source, hence the distance can be determined from the observed ionization equilibrium with a given source luminosity.

### C ASCA spectra of Seyfert 2 and Starburst galaxies

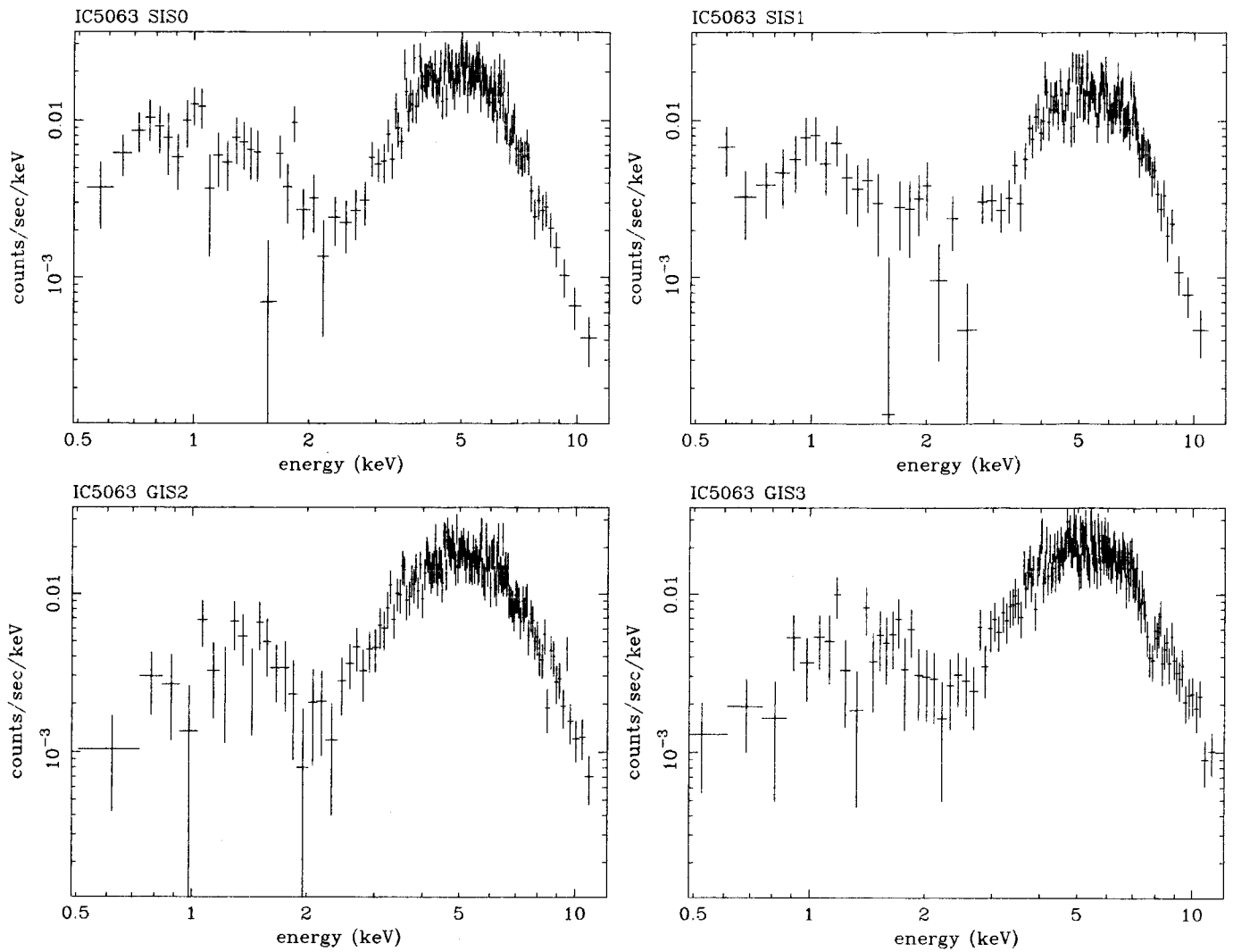


Figure 49: The ASCA spectra of IC5063

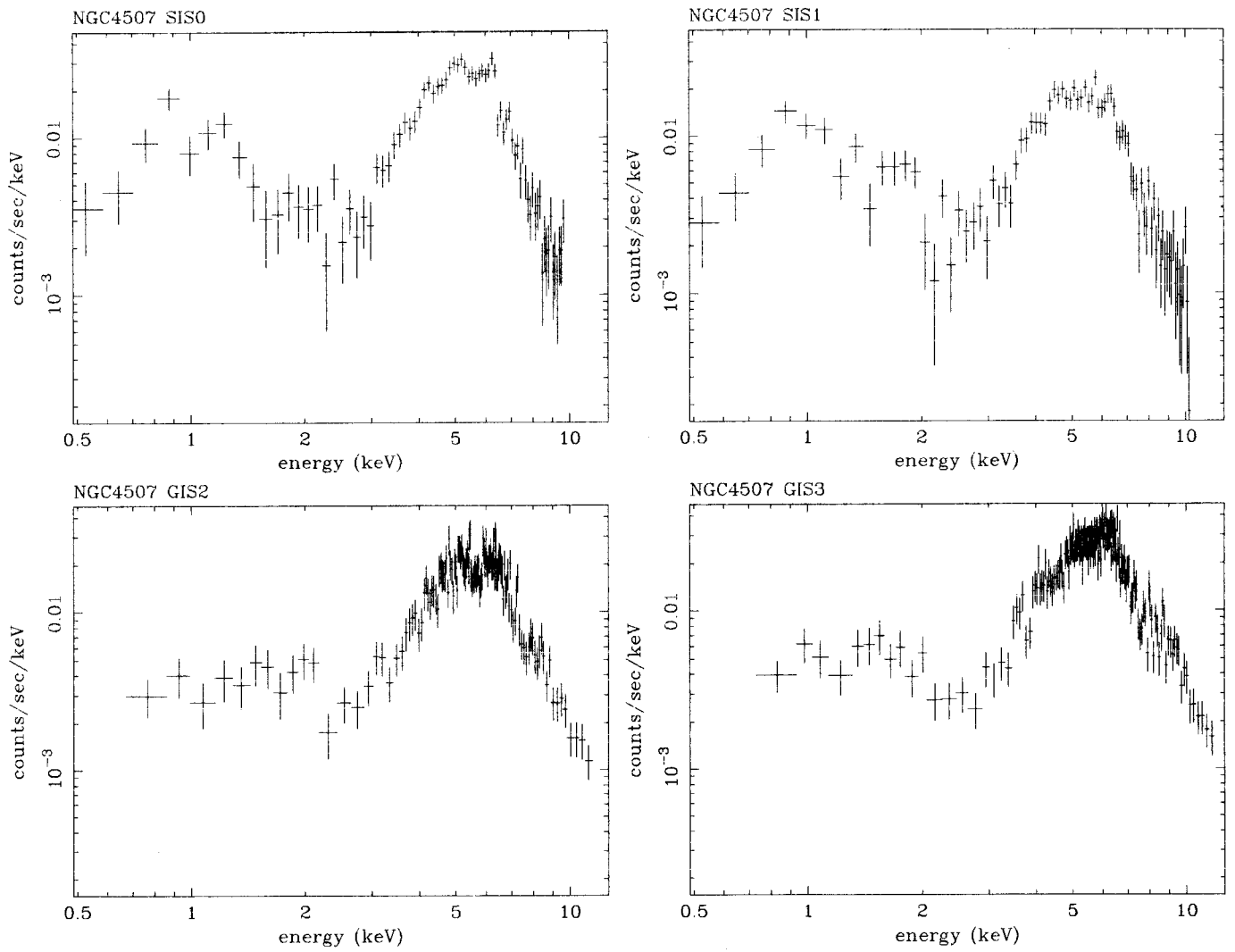


Figure 50: The ASCA spectra of NGC4507

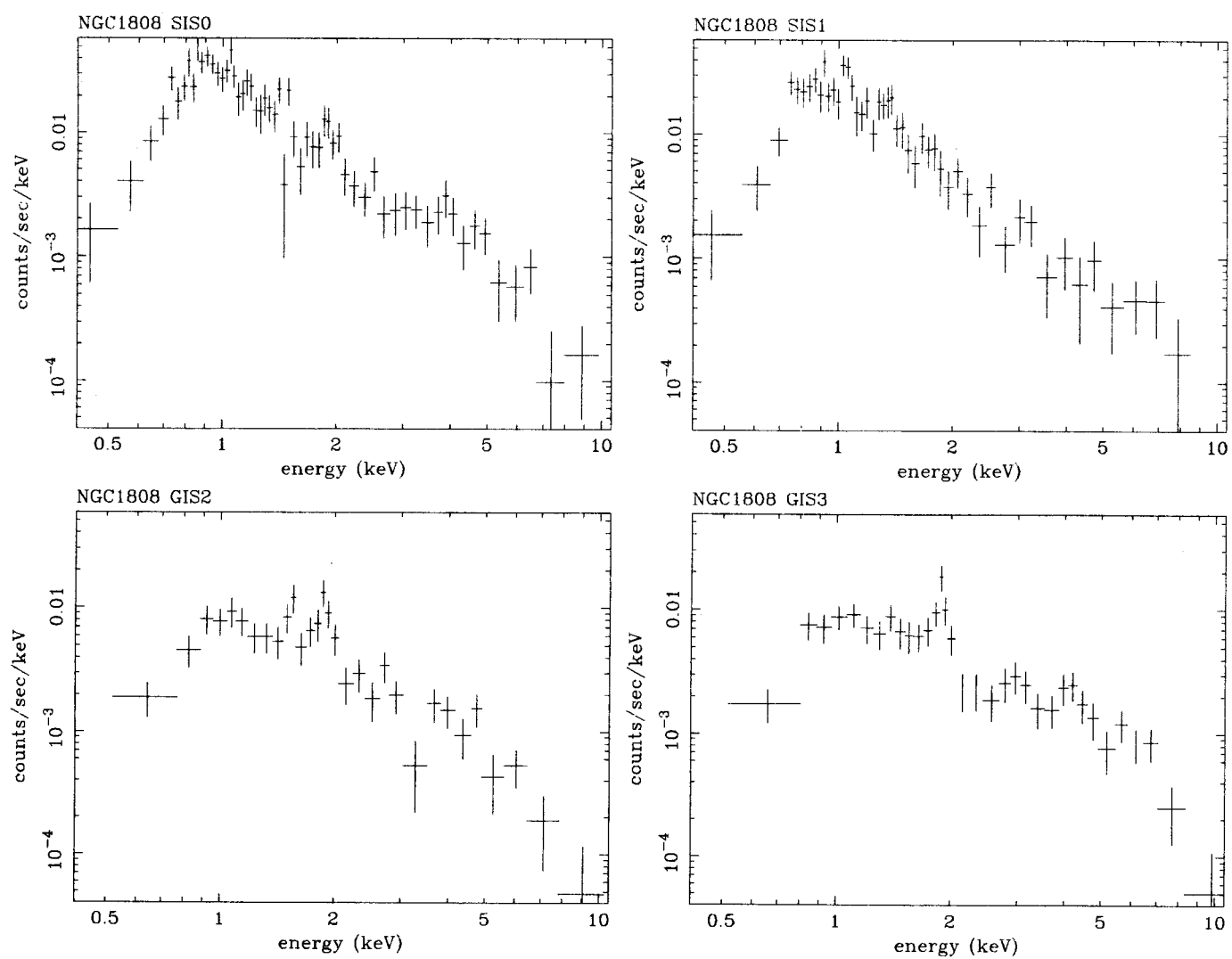


Figure 51: The ASCA spectra of NGC1808

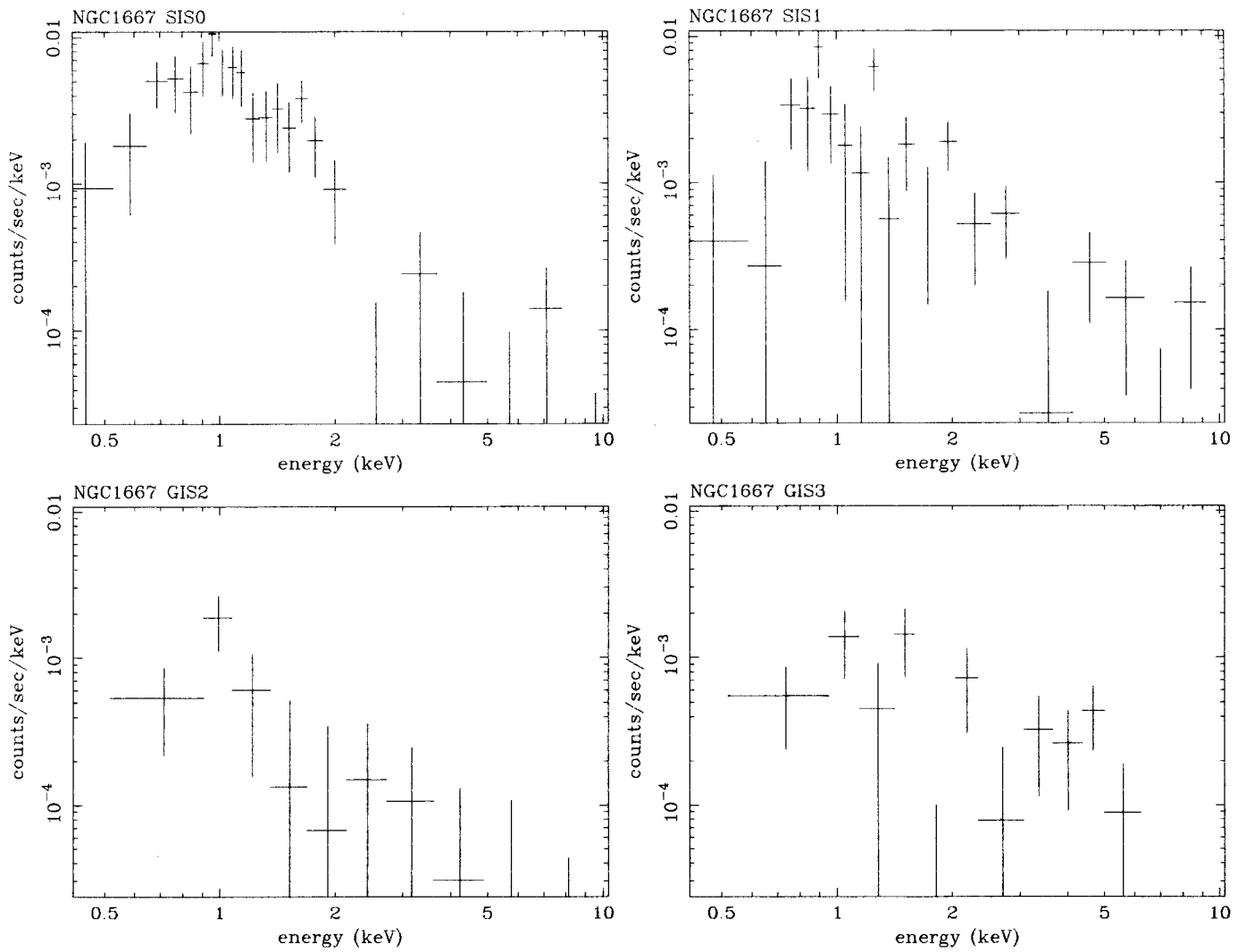


Figure 52: The ASCA spectra of NGC1667

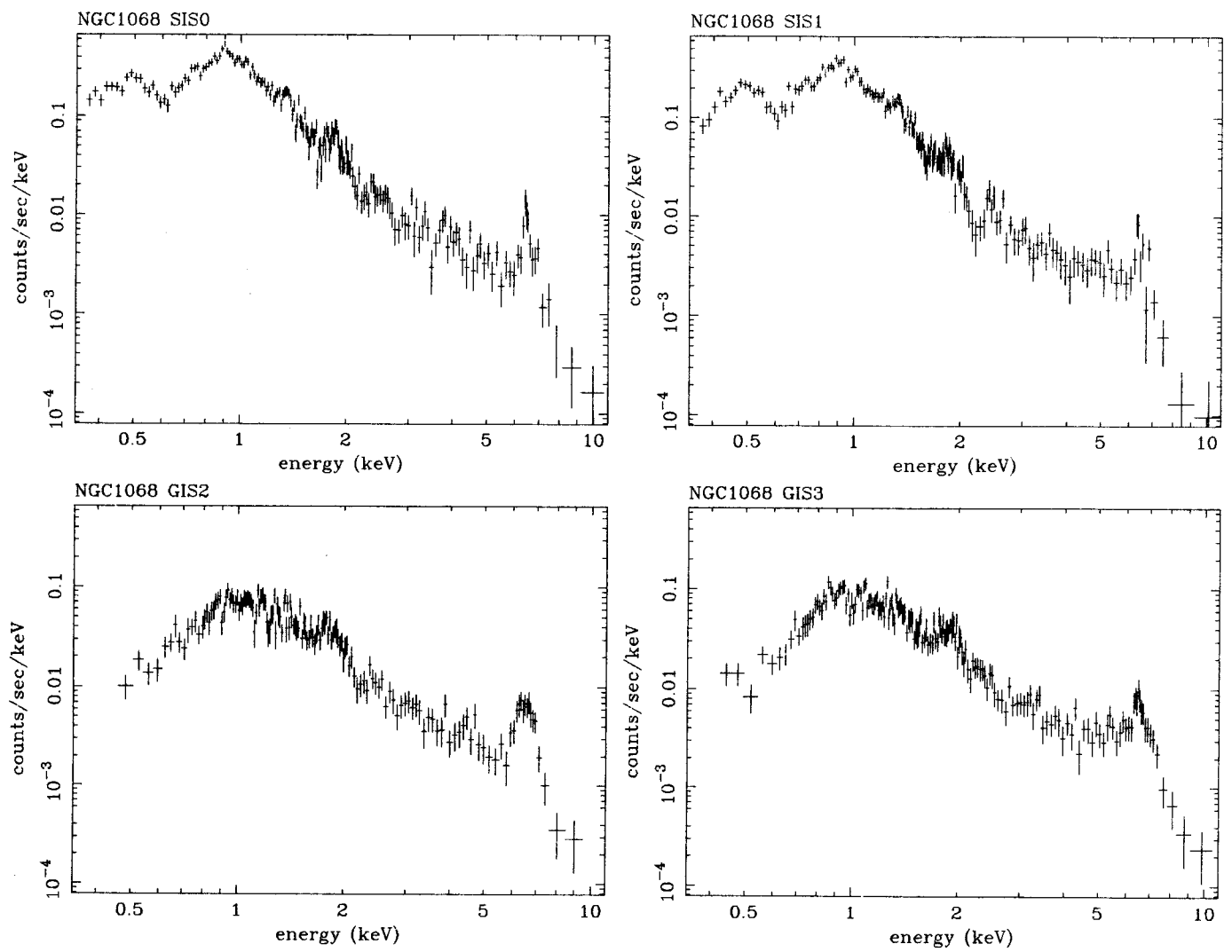


Figure 53: The ASCA spectra of NGC1068

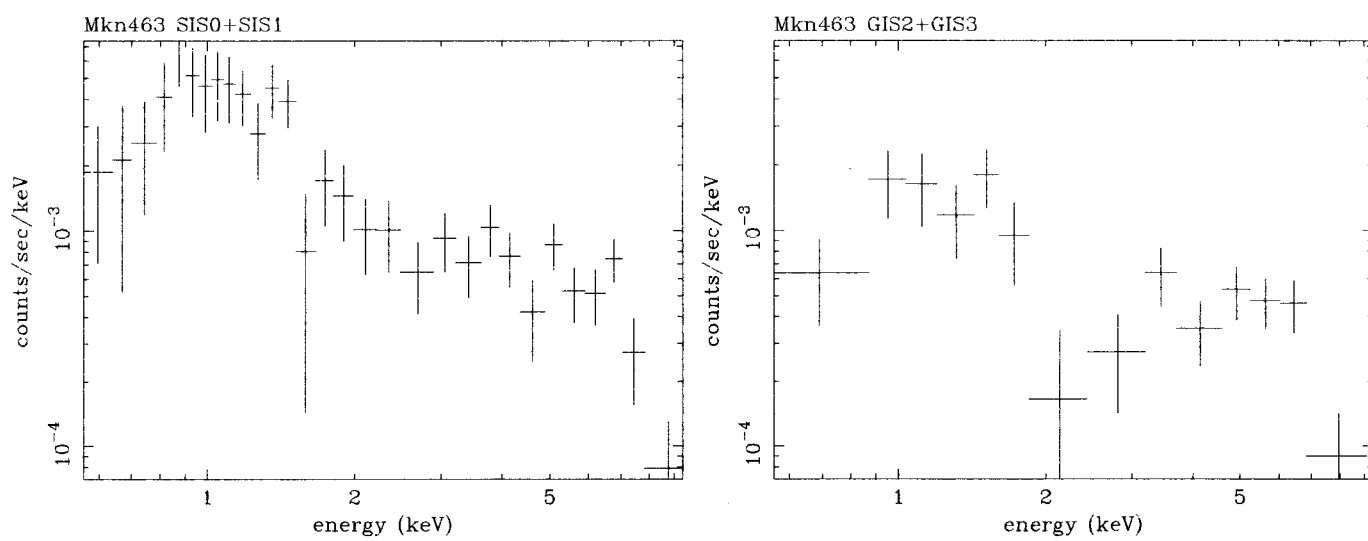


Figure 54: The ASCA spectra of Mkn463

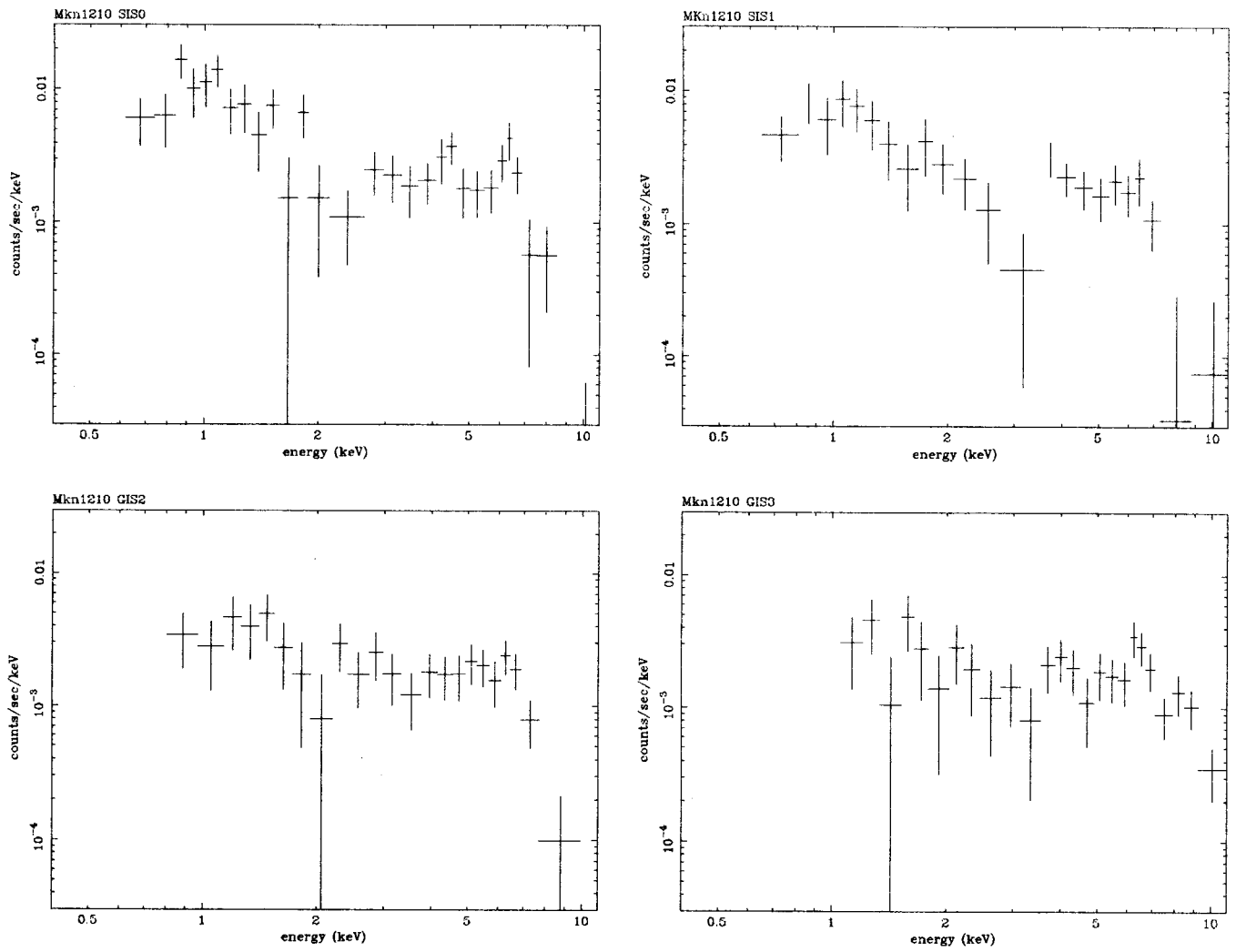


Figure 55: The ASCA spectra of Mkn 1210

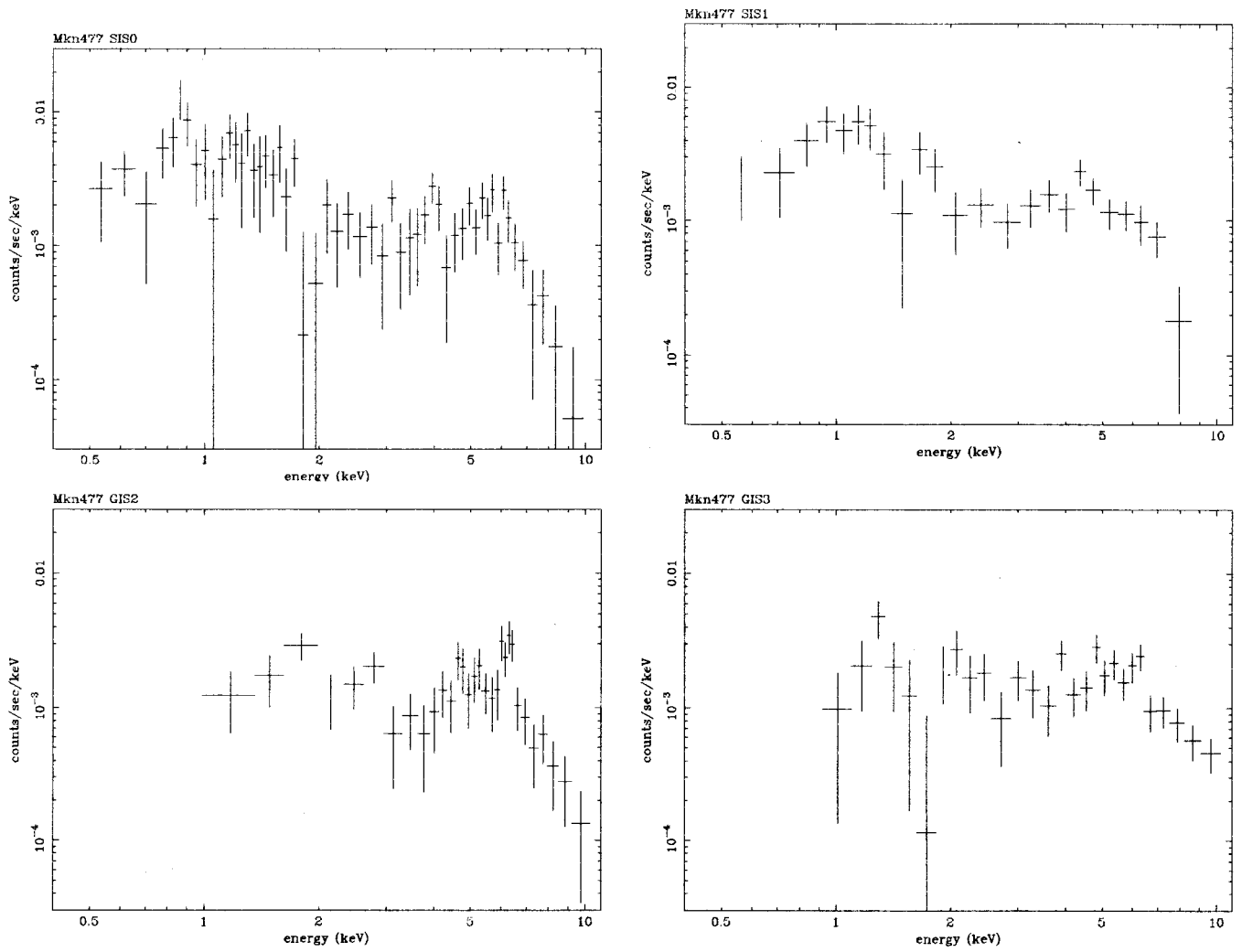


Figure 56: The ASCA spectra of Mkn 477

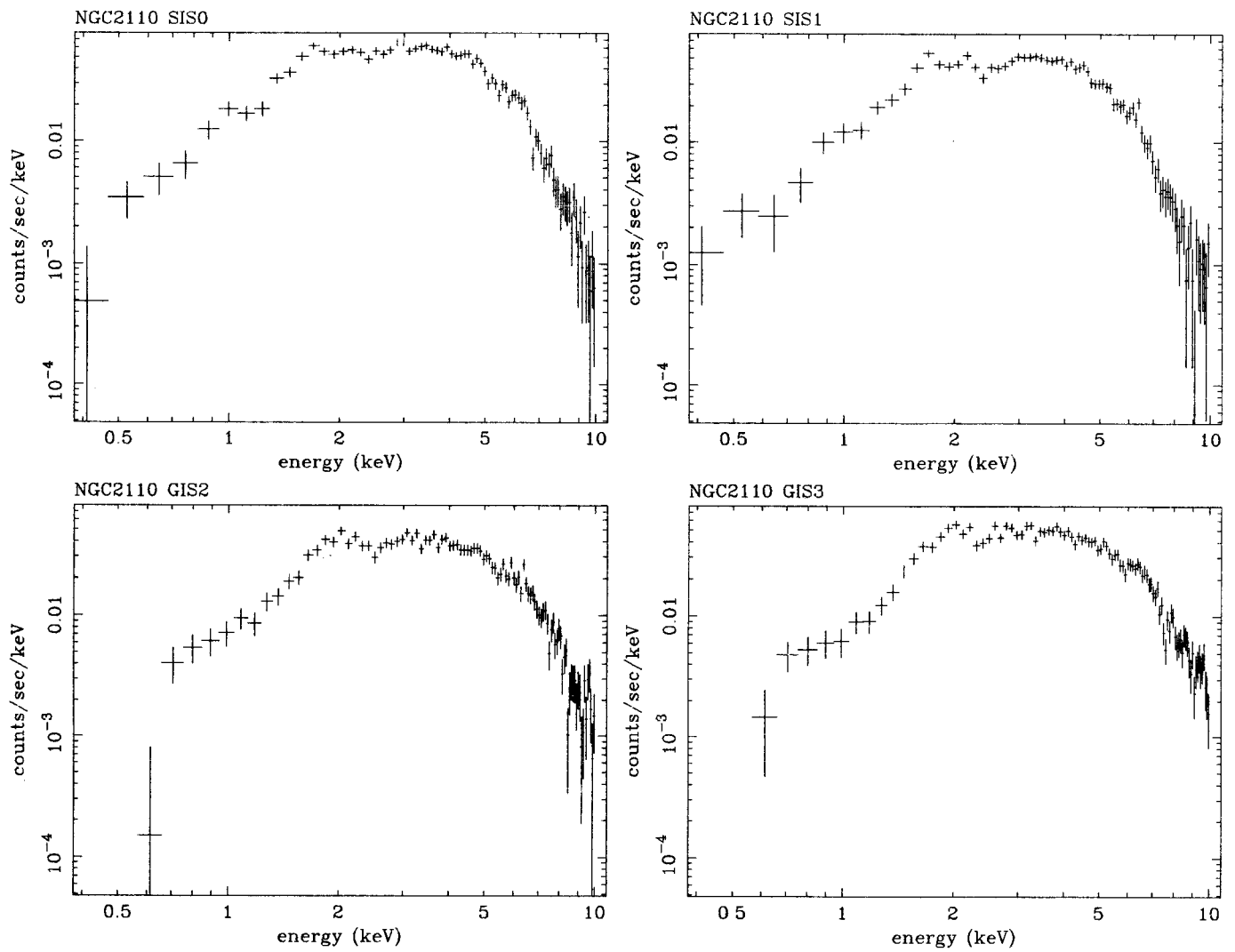


Figure 57: The ASCA spectra of NGC2110

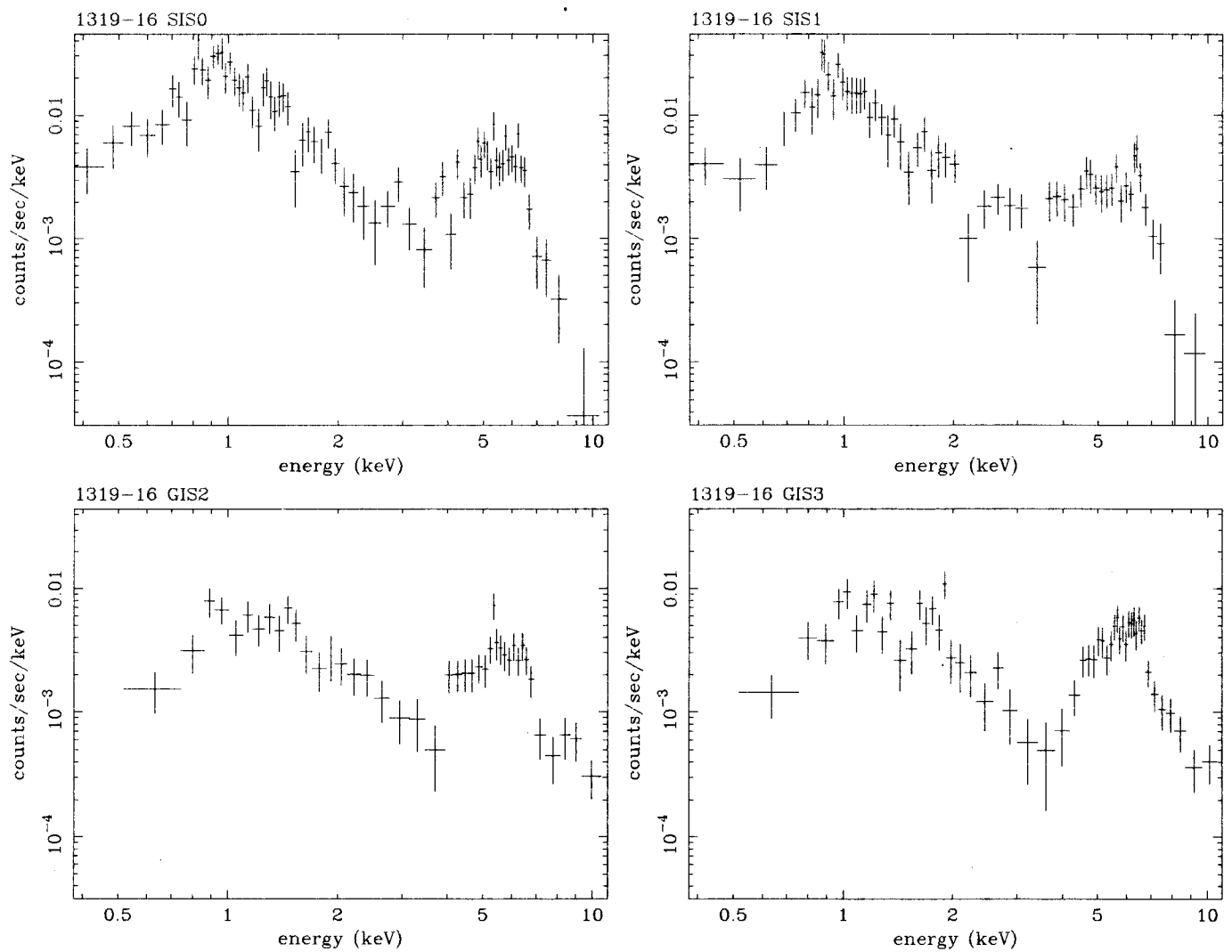


Figure 58: The ASCA spectra of PKS B1319-164

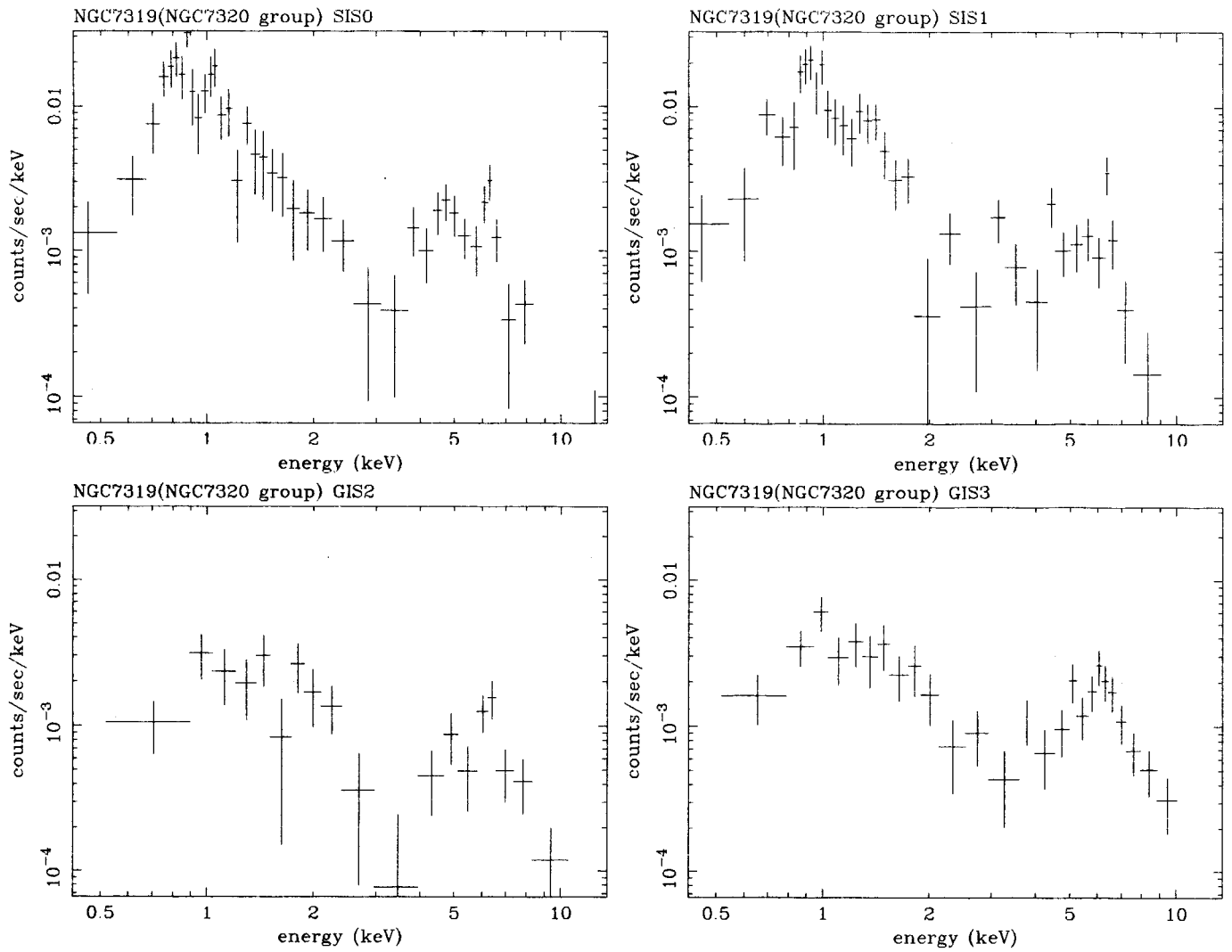


Figure 59: The ASCA spectra of NGC7319

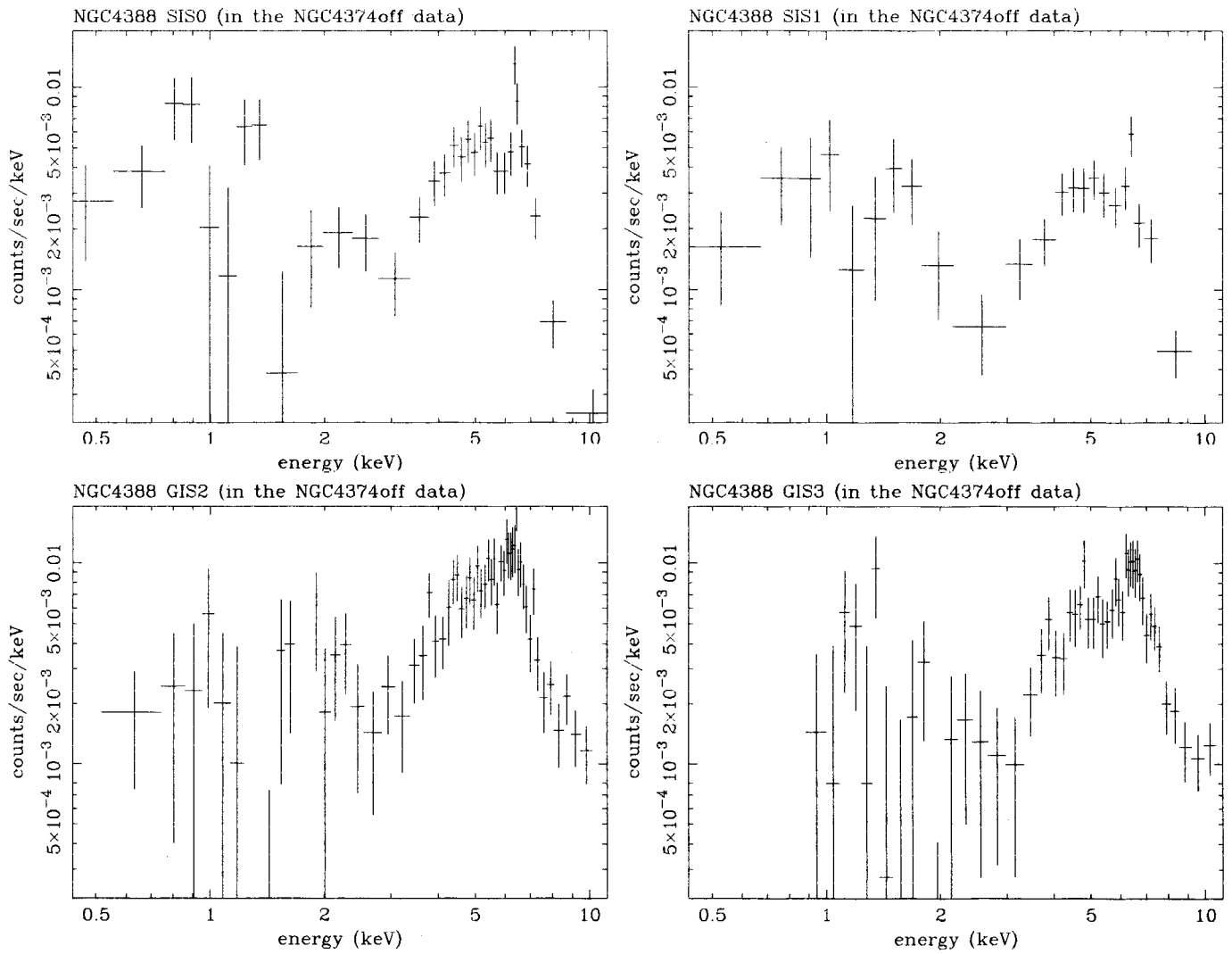


Figure 60: The ASCA spectra of NGC4388

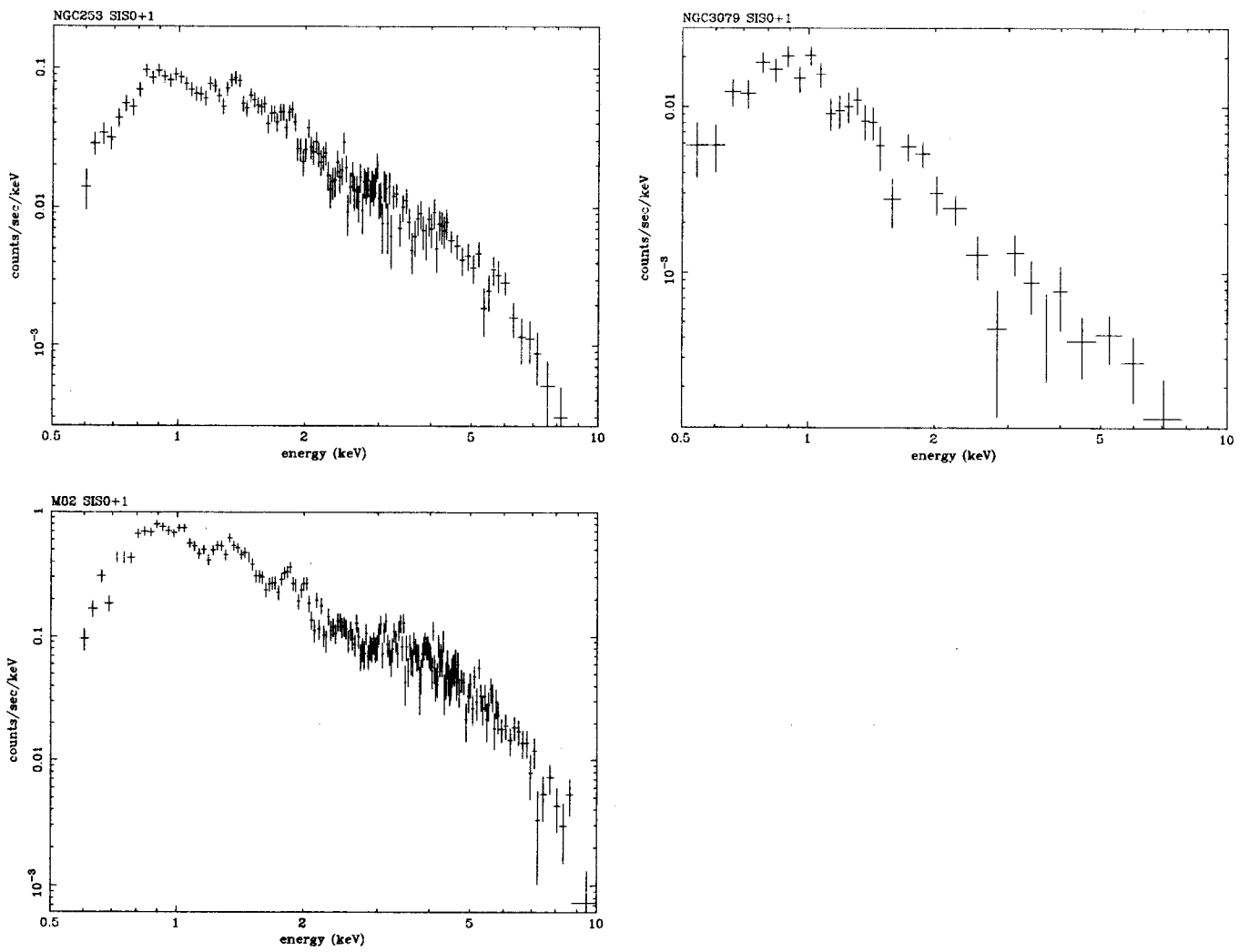


Figure 61: The ASCA SIS spectra of starburst galaxies

## D Glossary

Astro-D	Fourth Japanese X-ray satellite (before launch)
ASCA	Advanced Satellite for Cosmology and Astrophysics (Formerly ASTRO-D)
BBXRT	Broad Band X-ray Telescope
EXOSAT	European X-ray Observatory Satellite
FOV	Field of view
GIS	Gas Imaging Spectrometer
HEAO	High Energy Astrophysics Observatory
HRI	High-Resolution Imager (Einstein and ROSAT)
PSPC	Position-Sensitive Proportional Counter (Einstein and ROSAT)
ROSAT	Röntogensatellit
SAA	South Atlantic Anomaly
SIS	Solid-state Imaging Spectrometer
SSS	Solid State Spectrometer (Einstein)
$N_{\text{H}}$	Hydrogen equivalent column density
$\Gamma$	Photon index
$\xi$	Photoionization parameter (see Appendix B)
$kT$	temperature in unit of energy ( $k$ is Boltzmann constant)

## **Acknowledgments**

I am grateful to Prof. K. Koyama for his continuous support through the five years of my master and doctoral course. I am also grateful to H. Awaki, I. Hayashi, and R. Mushotzky for fruitful collaborations. Y. Maeda and T. Tsuru kindly allow me to analyze parts of their ASCA data. My thanks go to all graduate students of CR laboratory, especially H. Matsumoto and M. Sakano for their help. I want to express my thanks to all members of the ASCA and the launching staff of the Institute of Space and Astronautical Science.

## References

- [1] S.W. Allen and A.C. Fabian. 1992, *MNRAS*, 258,29p.
- [2] R. 1993 Antonucci. 1993, *ARA&A*, 31,473.
- [3] R.R.J Antonucci and Miller J.S. 1985, *ApJ*, 297,621.
- [4] R.R.J. Antonucci and J.S. Ulvestad. 1988, *ApJ*, 330,L97.
- [5] I. Appenzellar and R. Östreicher. 1988, *AJ*, 95,45.
- [6] K. A. Arnaud, R. M. Johnstone, A. C. Fabian, C. S. Crawford, P. E. J. Nulsen, R. A. Shafer, and R. F. Mushotzky. 1987, *MNRAS*, 227,241.
- [7] H. Awaki. 1991, *Ph.D.thesis, Nagoya Univ.*
- [8] H. Awaki. 1992, *In Ginga Memorial Symp., ed. F. Makino, F.Nagase, p.63. Tokyo: Inst.Space Aeronaut. Sci.*
- [9] H. Awaki. 1992, *In Frontiera of X-ray Astronomy, ed Y. Tanaka and K. Koyama (Universal Academic Press, Tokyo) p537.*
- [10] H. Awaki et al. 1991, *PASJ*, 43,L37.
- [11] H. Awaki et al. 1994, *PASJ*, 46,L65.
- [12] H. Awaki and R. E. Griffiths. 1996, *private communication.*
- [13] H. Awaki and K. Koyama. 1993, *Adv. Space. Res., Vol13, No12,221.*
- [14] H. Awaki, K. Koyama, H. Inoue, and J.P. Halpern. 1991, *PASJ*, 43,195.
- [15] H. Awaki, K. Koyama, H. Kunieda, and Y. Tawara. 1990, *Nature*, 346,544.
- [16] H. Awaki and M. Matsuoka. 1996, *private communication.*
- [17] J. A. Baldwin, M. M. Phillips, and R. Terlevich. 1981, *PASP*, 93,5.
- [18] D. L. Band, R. I. Klein, J. I. Castor, and J. K. Nash. 1990, *ApJ*, 362,90.
- [19] L. Bassani, G. Malaguti, E. Jourdain, J. P. Roques, and W. N. Johnson. 1995, *ApJ*, 444,L73.
- [20] P. R. Blanco. 1991, *Ph.D. thesis, University of Edinburgh.*
- [21] I. Bond, M. Matsuoka, and M. Yamauchi. 1992, *ApJ*, 405,179.

- [22] B. Boyle, R. Griffiths, T. Shanks, G. Stewart, and I. Georgantopoulos. 1992, *MNRAS*, 260,49.
- [23] H. V. Bradt, B. F. Burke, C. R. Canizares, P. E. Greenfield, R. L. Kelley, J. E. McClintock, J. van Paradijs, and Koski A. T. 1978, *ApJ*, 226,L111.
- [24] M. Cappi et al. 1996, *ApJ*, 456,141.
- [25] J. Clavel et al. 1991, *ApJ*, 366,34.
- [26] L. Colina. 1992, *ApJ*, 386,59.
- [27] L. Colina, W. B. Sparks, and F. Macchetto. 1991, *ApJ*, 370,102.
- [28] A. Comastri, G. Setti, G. Zamorani, and G. Hasinger. 1995, *A&A*, 296,1.
- [29] O. Dahari and M. De Robertis. 1988, *ApJ Suppl.*, 67,249.
- [30] L. Danese, G. De Zotti, G. Fasano, and A. Franceschini. 1986, *A&A*, 161,1.
- [31] L. P. David, C. Jones, and W. Forman. 1992, *ApJ*, 388,82.
- [32] M.H.K. De Grijp, G.K. Miley, J. Lub, and T. De Jong. 1985, *Nature*, 314,240.
- [33] M. M. De Robertis, J. B. Hutchings, and R. E. Pitts. 1988, *AJ*, 95,1371.
- [34] M.M. De Robertis and D.E. Osterbnnrock. 1984, *ApJ*, 272,478.
- [35] M.M. De Robertis and D.E. Osterbnnrock. 1986, *ApJ*, 301,727.
- [36] N. Duric and E.R. Seaquist. 1988, *ApJ*, 326,574.
- [37] M. Elvis, U.G. Briel, and J.P. Henry. 1983, *ApJ*, 268,105.
- [38] M. Elvis, C. Fassnacht, A.S. Wilson, and U. Briel. 1990, *ApJ*, 361,459.
- [39] M. Elvis and A. Lawrence. 1988, *ApJ*, 331,161.
- [40] M. Elvis, T. Maccacaro, A.S. Wilson, M.J. Ward, M.V. Penston, et al. 1978, *MNRAS*, 183,129.
- [41] G. Fabbiano. 1988, *ApJ*, 330,672.
- [42] G. Fabbiano. 1989, *ARA&A*, 27,87.
- [43] G. Fabbiano and G. Trinchieri. 1984, *ApJ*, 286,491.

- [44] A.C. Fabian. 1979, *Proc. R. Soc. London Ser. A*, 336,449.
- [45] A.C. Fabian. 1992, *In Frontiera of X-ray Astronomy*, ed Y. Tanaka and K. Koyama (Universal Academic Press, Tokyo) p603.
- [46] A.V. Filippenko and W.L.W. Sargent. 1992, *AJ*, 103,28.
- [47] D.A. Forbes, C. Boisson, and M.J. Ward. 1992, *A&A*, 259,293.
- [48] H.C. Ford, O. Dahari, G.H. Jacoby, P.C. Crane, and R. Ciardullo. 1986, *ApJ*, 311,L7.
- [49] W. Forman, C. Jones, and W. Tucker. 1985, *ApJ*, 293,102.
- [50] Y. Fukazawa, K. Makishima, K. Ebisawa, A. C. Fabian, K. C. Gendreau, Y. Ikebe, K. Iwasawa, T. Kii, et al. 1994, *PASJ*, 46,L141.
- [51] I.M. George and A.C. Fabian. 1991, *MNRAS*, 249,352.
- [52] F.C. Gillett, D.E. Kleinmann, E.L. Wright, and R.W. Capps. 1975, *ApJ*, 198,L65.
- [53] R. W. Goodrich, S. Veilleux, and G. J. Hill. 1994, *ApJ*, 422,521.
- [54] P. Grandi, G. Tagliaferri, P. Giommi, P. Barr, and G. Paslumbo. 1992, *ApJS*, 82,93.
- [55] R. E. Griffith and P. Padovani. 1990, *ApJ*, 360,483.
- [56] P.W. Guilbert and M.J. Rees. 1988, *MNRAS*, 233,475.
- [57] J.P. Halpern. 1982, *PhD thesis. Harvard Univ.*
- [58] C. G. Hanson, G. K. Skinner, C. J. Eyles, and A. P. Wilmore. 1990, *MNRAS*, 242,262.
- [59] D. E. Harris, W. Forman, I. M. Gioia, J. A. Hale, F. R. Jr Harnden, C. Jones, T. Karakashian, T. Maccacaro, et al. 1990, *Einstein Observatory Catalog of IPC X-Ray Source 5*, 377, 5,377.
- [60] I. Hayashi, K. Koyama, H. Awaki, and S. Ueno. 1996, *PASJ*, 48,219.
- [61] T. M. Heckman, L. Armus, and G. K. Miley. 1990, *ApJS*, 74,833.
- [62] T.M. Heckman. 1980, *A&A*, 87,152.
- [63] S.S. Holt, R.F. Mushotzky, R.H. Becker, E.A. Boldt, P.J. Serlemitsos, et al. 1980, *ApJ*, 241,L13.
- [64] J. P. Huchra, W. F. Wyatt, and M. Davis. 1982, *AJ*, 87,1628.

- [65] J.B. Hutchings and S.G. Neff. 1989, *AJ*, 97,1306.
- [66] H. Inoue. 1985, *Space Sci. Rev.*, 40,317.
- [67] H. Inoue. 1990, *In Proc. 23rd ESLAB Symp.*, ed. J.Hunt, B.Battrick, p.783. Paris: Eur. Space Agency.
- [68] H. Inoue, T. Kii, Y. Ogasaka, T. Takahashi, and Y. Ueda. 1997, *X-ray Imaging and Spectroscopy of Cosmic Hot Plasma*, p.3 ed. F. Makino, K. Mitsuda.
- [69] J. A. Irwin and E. R. Sequist. 1988, *ApJ*, 335,658.
- [70] K. Iwasawa. 1994, *Ph.D.thesis, Nagoya Univ.*
- [71] K. Iwasawa, K. Koyama, H. Awaki, H. Kunieda, K. Makishima, T. Tsuru, T. Ohashi, and N. Nakai. 1993, *ApJ*, 409,155.
- [72] K. Iwasawa, T. Yaqoob, H. Awaki, and Y. Ogasaka. 1994, *PASJ*, 46,L167.
- [73] B. Jones and J.M. Rodríguez-Espinosa. 1984, *ApJ*, 285,580.
- [74] N. Junkes, H. Zinnecker, G. Hensler, M. Dahlem, and W. Pietsch. 1995, *A&A*, 294,8.
- [75] T.R. Kallman and R. McCray. 1982, *ApJ Suppl.*, 50,263.
- [76] L. E. Kay. 1994, *ApJ*, 430,196.
- [77] A. L. Kinney, R. R. J. Antonucci, M. J. Ward, A. S. Wilson, and M. Whittle. 1991, *ApJ*, 377,100.
- [78] A.L. Kinney, R.C. Bohlin, D. Calzetti, N. Panagia, and Rosemary F.G. Wyse. 1993, *APJS*, 86,5.
- [79] A.P. Koratkar and C.M. Gaskell. 1991, *ApJS*, 75,719.
- [80] B. Koribalski, M. Dahlem, U. Mebold, and E Brinks. 1993, *A&A*, 268,14.
- [81] K.T. Korista and G.J. Ferland. 1989, *ApJ*, 343,678.
- [82] K. Koyama, H. Awaki, K. Iwasawa, and M. J. Ward. 1992, *ApJ*, 399,L129.
- [83] K. Koyama, H. Inoue, S. Takano, Y. Tanaka, T. Ohashi, and M. Matsuoka. 1989, *PASJ*, 41,731.
- [84] G.A. Kriss, C.R. Canizares, and G.R. Ricker. 1980, *ApJ*, 242,492.

- [85] J.G. Krolik and M.C. Begelman. 1986, *ApJ*, 308,L55.
- [86] J.G. Krolik and M.C. Begelman. 1988, *ApJ*, 329,702.
- [87] J.H. Krolik and T.R. Kallman. 1987, *ApJ*, 320,L5.
- [88] J.S. Kruper, C.M. Urry, and C.R. Canizares. 1990, *ApJ Suppl.*, 74,347.
- [89] A. Lawrence. 1991, *MNRAS*, 252,586.
- [90] A. Lawrence and Elvis M. 1982. 1982, *ApJ*, 256,410.
- [91] A. Lawrence, M. Ward, M. Elvis, G. Fabbiano, S.P. Willner, N.P. Carleton, and A. Longmore. 1985, *ApJ*, 291,117.
- [92] A.P. Lightman and T.R. White. 1988, *ApJ*, 335,57.
- [93] D. Lynden-Bell. 1969, *Nature*, 223,690.
- [94] R. Maiolino and G. H. Rieke. 1995, *ApJ*, 454,95.
- [95] K. Makishima. 1986, *In The Physics of Accretion onto Compact Objects*, ed. K.O.Mason, M.G.Watson, N.E.White, p.249. Berlin:Springer-Verlag.
- [96] F. E. Marshall, H. Netzer, K. A. Arnaud, E. A. Boldt, S. S. Holt, K. M. Jahoda, R. Kelley, R. F. Mushotzky, R. Petre, P. J. Serlemitsos, A. P. Smale, J. H. Swank, A. E. Szymkowiak, and K. A. Weaver. 1993, *ApJ*, 405,168.
- [97] F.E. Marshall, H. Netzer, K. Arnaud, E.A. Boldt, S.S. Holt, et al. 1992, *ApJ*, 405,168.
- [98] N. Marshall, R.S. Warwick, and K.A. Pounds. 1981, *MNRAS*, 194,987.
- [99] H. Matsumoto. 1994, *Master thesis, Kyoto University*.
- [100] M. Matsuoka, M. Yamauchi, L. Piro, and T. Murakami. 1990, *ApJ*, 361,440.
- [101] G. Matt, F. Fiore, G. C. Perola, et al. 1996, *MNRAS*, 281,69.
- [102] G. Matt, G.C. Perola, and L. Piro. 1991, *A&A*, 247,27.
- [103] J.M. Mazzarella, R.A. Gaume, B.T. Soifer, J.R. Graham, G. Neugebauer, and K. Matthews. 1993, *AJ*, 102,1241.
- [104] P.J. McCarthy, T.M. Heckman, and W. van Breugel. 1987, *AJ*, 93,264.
- [105] J. E. McClintock, J. van Paradijs, R. A. Remillard, C. R. Canizares, and Veron P. Koski, A. T. 1979, *ApJ*, 233,809.

- [106] I.M. McHardy. 1990, *In Proc. 23rd ESLAB symp., ed. J.Hunt, B.Battrick, p.1111. Paris:Eur.Space Agency.*
- [107] J. S. Miller and R. W. Goodrich. 1990, *ApJ*, 355,456.
- [108] J.S. Miller, R.W. Goodrich, and W.G. Mathew. 1991, *ApJ*, 378,47.
- [109] R. Monier and J.P. Halpern. 1987, *ApJ*, 315,L17.
- [110] A.F.N. Moorwood and E. Oliva. 1988, *A&A*, 203,278.
- [111] J. S. Mulchaey, A. Koratkar, M. J. Ward, A. A. Wilson, M. Whittle, R. R. J. Antonucci, A. L. Kinney, and T. Hurt. 1994, *ApJ*, 436,586.
- [112] J. S. Mulchaey, R. F. Mushotzky, and K. A. Weaver. 1992, *ApJ*, 390,L69.
- [113] R. F. Mushotzky. 1982, *ApJ*, 256,92.
- [114] R. F. Mushotzky, C. Done, and K. A. Pounds. 1993, *Annu. Rev. Astron. Astrophys.*, 31,717.
- [115] R. F. Mushotzky, A. C. Fabian, K. Iwasawa, H. Kunieda, M. Matsuoka, K. Nandra, and Y. Tanaka. 1995, *MNRAS*, 272,L9.
- [116] R.F. Mushotzky. 1984, *Adv. Space Res.*, 3,10.
- [117] T. Nakagawa et al. 1997, *in preparation.*
- [118] K. Nandra. 1991, *PhD thesis. Univ. Leicester, Engrand.*
- [119] K. Nandra and K. A. Pounds. 1994, *MNRAS*, 268,405.
- [120] K. Nandra, K.A. Pounds, G.C. Stewart, I.M. George, K. Hayashida, et al. 1991, *MNRAS*, 248,760.
- [121] H. Netzer et al. 1990, *ApJ*, 353,108.
- [122] J.B. Oke and W.L.W. Sargent. 1968, *ApJ*, 151,807.
- [123] D.E. Osterbrock. 1978, *Proc. Nat. Acad. Sci.*, 72,540.
- [124] D.E. Osterbrock. 1988, *in Active Galactic Nuclei, ed. H.R. Miller & P.J.Wiita (Berlin: Springer-Verlag), p.1.*
- [125] D.E. Osterbrock. 1989, *Astrophysics of Gaseous Nebulae and Active Galactic Nuclei(Mill Valley: Univ. Science Books).*

- [126] D.E. Osterbrock. 1991, *Rep. Prog. Phys.*, 54,579.
- [127] D.E. Osterbrock and M.M. De Robertis. 1985, *PASP*, 97,1129.
- [128] D.E. Osterbrock and R.A. Shaw. 1988, *ApJ*, 327,89.
- [129] B.M. Peterson. 1988, *PASP*, 100,18.
- [130] B.M. Peterson et al. 1991, *ApJ*, 368,119.
- [131] A.C. Philips. 1993, *AJ*, 105,486.
- [132] G. Piccinotti, R.F. Mushotzky, E.A. Boldt, S.S. Holt, F.E. Marshall, et al. 1982, *ApJ*, 253,485.
- [133] L. Piro et al. 1994, *In New Horizen of X-ray Astronomy, first resolts from ASCA, ed. F.Makino, T.Ohashi, p591, Tokyo,:Universal Academy Press.*
- [134] L. Piro, M. Yamauchi, and M. Matsuoka. 1990, *ApJ*, 360,L35.
- [135] R. W. Pogge. 1989, *ApJ*, 345,730.
- [136] K.A. Pounds, K. Nandra, G.C. Stewart, I.M. George, and A.C. Fabian. 1990, *Nature*, 344,132.
- [137] K.A. Pounds, K. Nandra, G.C. Stewart, and K. Leighly. 1989, *MNRAS*, 240,769.
- [138] K.A. Pounds, T.J. Turner, and R.S. Warwick. 1986, *MNRAS*, 221,7p.
- [139] J. C. Raymond and B. W. Smith. 1977, *ApJS*, 35,419.
- [140] M. J. Rees. 1984, *Annu. Rev. Astron. Astrophys.*, 22,471.
- [141] R. A. Remillard, H. V. D. Bradt, R. J. V. Brissenden, D. A. H. Buckley, W. Roberts, D. A. Schwartz, B. A. Stroozas, and I. R. Tuohy. 1993, *AJ*, 105,2079.
- [142] G. H. Rieke. 1988, *ApJL*, 331,L5.
- [143] G.H. Rieke and M.J. Lebofsky. 1979, *Annu. Rev. Astron. Astrophys.*, 17,477.
- [144] G.H. Rieke, M.J. Lebofsky, R.I. Thompson, F.J. Low, and A.T. Tokunaga. 1980, *ApJ*, 238,24.
- [145] G.H. Rieke and F.J. Low. 1975, *ApJ*, 197,17.
- [146] P. F. Roche, D. K. Aitken, C. H. Smith, and M. J. Ward. 1991, *MNRAS*, 248,606.

- [147] P.F. Roche and D.K. Aitken. 1985, *MNRAS*, 213,789.
- [148] V. C. Rubin. 1978, *ApJ*, 224,L55.
- [149] R.W. Russell, B.T. Soifer, and K.M. Merrill. 1977, *ApJ*, 213,66.
- [150] F. Ryde et al. 1997, *in preparation*.
- [151] D.J. Saikia et al. 1990, *MNRAS*, 245,397.
- [152] D.B. Sanders, E.S. Phinney, G. Neugebauer, B.T. Soifer, and K. Mathews. 1989, *ApJ*, 347,29.
- [153] D.B. Sanders, B.T. Soifer, J.H. Elias, G. Neugebauer, and K. Matthews. 1988, *ApJ*, 328,L35.
- [154] M. Schmidt and R.F. Green. 1983, *ApJ*, 269,352.
- [155] N.Z. Scoville, , et al. 1985, *ApJ*, 289,129.
- [156] P. J. Serlemitsos, L. Jalota, Y. Soong, H. Kunieda, Y. Tawara, Y. Tsusaka, H. Suzuki, Y. Sakima, T. Yamazaki, H. Yoshioka, A. Furuzawa, K. Yamashita, H. Awaki, M. Itoh, Y. Ogasaka, H. Honda, and Y. Uchibori. 1995, *PASJ*, 47,105.
- [157] T. Shanks, I. Georgantopoulos, G.C. Stewart, K.A. Pounds, B.J. Boyle, and R.E. Griffiths. 1991, *Nature*, 353,315.
- [158] G.A. Shields. 1977, *ApJL*, 18,119.
- [159] J.M. Shuder. 1980, *ApJ* 240, 32, 240,32.
- [160] J.M. Shuder and D.E. Osterbrock. 1981, *ApJ*, 250,55.
- [161] D. A. Smith, C. Done, and K. A. Pounds. 1993, *MNRAS*, 263,54.
- [162] S. Souffrin. 1969, *A&A*, 1,305.
- [163] T. Storchi-Bergmann. 1991, *MNRAS*, 249,404.
- [164] G.M. Stripe and A.G. De Bruyn. 355, *A&A*, 1991,245.
- [165] M. Sugizaki, H. Inoue, T. Sonobe, T. Takahashi, and Y. Yamamoto. 1997, *PASJ*, 49,59.
- [166] C. M. Telesco, E. E. Becklin, C. G. Wynn-Williams, and D. A. Harper. 1984, *ApJ*, 282,427.
- [167] J. Terrell. 1967, *ApJ*, 147,827.
- [168] J.E. Tohline and D.E. Osterbrock. L49, 1982, *ApJ*,252.

- [169] H. D. Tran. 1995, *ApJ*, 440,578.
- [170] H. D. Tran, J. S. Miller, and L.E. Kay. 1992, *ApJ*, 397,452.
- [171] G. Trinchieri and G. Fabbiano. 1985, *ApJ*, 296,447.
- [172] T. Tsuru et al. 1994, *In New Horizen of X-ray Astronomy, First results from ASCA, p.529 ed. F. Makino, T.Ohashi, Tokyo: University Academy Press.*
- [173] R.G. Tull, S.S. Vogt, and P.W. Kelton. 1979, *Instr. Astr. III, SPIE Proc.*, 172,90.
- [174] T. J. Turner, K. A. Weaver, R. F. Mushotzky, S. S. Holt, and G. M. Madejski. 1991, *ApJ*, 381,85.
- [175] T.J. Turner. 1988, *PhD thesis, Leicester Univ., Engrand.*
- [176] T.J. Turner and K.A. Pounds. 1988, *MNRAS*, 232,463.
- [177] T.J. Turner and K.A. Pounds. 1989, *MNRAS*, 240,833.
- [178] S. Ueno et al. 1997, *in preparation.*
- [179] S. Ueno, K. Koyama, M. Nishida, S. Yamauchi, and M. J. Ward. 1994, *ApJ*, 431,L1.
- [180] S. Ueno, R.F. Mushotzky, K. Koyama, K. Iwasawa, H. Awaki, and I. Hayashi. 1994, *PASJ*, 46,L71.
- [181] J.S. Ulvestad and A.S. Wilson. 1983, *ApJ*, 264,L7.
- [182] J.S. Ulvestad and A.S. Wilson. 1989, *ApJ*, 343,659.
- [183] A. Uomoto, S. Caganoff, H.C. Ford, E.I. Rosenblatt, R.R.J. Antonucci, I.N. Evans, and R.D. Cohen. 1993, *AJ*, 105,1308.
- [184] S. Veilleux, G. Cecil, J. Bland-Hawthorn, R. B. Tully, A. V. Filippenko, and W. L. W. Sargent. 1994, *ApJ*, 433,48.
- [185] S. Veilleux and D.E. Osterbrock. 1987, *ApJS*, 63,295.
- [186] M. Veron. 1980, *A&AS*, 20,191.
- [187] M.-P. Véron-Cetty and P Véron. 1985, *A&A*, 145,425.
- [188] W.H. Waller, S.G. Kleinmann, and G.R. Ricker. 1988, *AJ*, 95,1057.
- [189] R. Walter and H.H. Fink. 1993, *A&A*, 274,105.

- [190] A. Wandel and R.F. Mushotzky. 1986, *ApJ*, 306,L61.
- [191] M. J. Ward, C. Done, A.C. Fabian, A.F. Tennant, and R.A. Shafer. 1988, *ApJ*, 324,767.
- [192] M.G. Watson, V. Stanger, and R.E Griffiths. 1984, *ApJ*, 286,144.
- [193] K. A. Weaver and H. Awaki. 1996, *private communication*.
- [194] K. A. Weaver, R. F. Mushotzky, P. J. Serlemitsos, A. S. Wilson, M. Elvis, and U. Briel. 1995, *ApJ*, 442,597.
- [195] K.A. Weavwer, J. Nousek, et al. 1996, *ApJ*, 458,160.
- [196] K.A. Weavwer, T. Yaqoob, R.F. Mushotzky, J. Nousek, I. Hayashi, and K. Koyama. 1997, *ApJ*, 474,675.
- [197] D. W. Weedman. 1977, *ARA&A*, 15,69.
- [198] M. Whittle. 1985, *MNRAS*, 216,817.
- [199] M. Whittle. 1985, *MNRAS*, 213,33.
- [200] B.J. Wilkes and M Elvis. 1987, *ApJ*, 323,243.
- [201] S. Willner, B.T. Soifer, R.W. Russell, R.R. Joyce, and Gillett F.C. 1977, *ApJ*, 217,L121.
- [202] B.J. Wills et al. 1997, *BAAS*, 9,647.
- [203] A. S. Wilson, J. A. Baldwin, and Ulvestad J. S. 1985, *ApJ*, 291,627.
- [204] A.C. Wilson. 1979, *Proc. R. Soc. London Ser. A*, 366,461.
- [205] A.S. Wilson, M. Elvis, A. Lawrence, and J. Bland-Hawthorn. 1992, *ApJ*, 391,L75.
- [206] A.S. Wilson and J.S. Ulvestad. 1982, *ApJ*, 263,576.
- [207] A.S. Wison and B. Nath. 1990, *ApJS*, 74,731.
- [208] L. Woltjer. 1959, *ApJ*, 130,38.
- [209] L Woltjer. 1968, *AJ*, 73,914.
- [210] G.S. Wright and R.D. Joseph. 1989, *In Infrared Spectroscopy in Astronomy*, ed. B.H.Kaldeich(Nordwijk:ESA),535.